

Tephrochronology of the Last Interglacial in Northwest Europe

by

Denise Avia Becker

Submitted in accordance
with the requirements for
the Degree of Masters by Research

The University of Leeds
Department of Earth and Environment

December 2024

Authorization

I confirm that the work submitted is my own and that appropriate credit has been given where reference has been made to the work of others.

This copy has been supplied on the understanding that it is copyright material and that no quotation from the thesis may be published without proper acknowledgement.

This thesis does not exceed the maximum word limit of 30,000 words, excluding reference lists.

Denise Avia Becker

ACKNOWLEDGEMENTS

My first thanks go to Professor Natasha Barlow and Dr Amy McGuire at University of Leeds for both their moral and academic support throughout this research. I specifically thank Natasha for reading past all of my spelling mistakes and Amy for her technical tephra knowledge in the laboratory. I am very grateful for their understanding and guidance throughout the past year. I also mention Harri Wyn Williams and Charles Woodhouse in the Thin Section Workshop for making resin stubs and assisting me with polishing them. I acknowledge Richard Walshaw for his help operating the EMPA instrument so I could collect geochemical data. I appreciate Professor Stefan Lauterbach and his collaborators at University of Potsdam for providing the cores and pollen data used in the study for which their previous work provided the foundation of this thesis. Lastly, I extend my heartfelt thanks to my mom and my best friend, Biana, for their unwavering support during my move abroad.

ABSTRACT

Understanding the timing of natural climate system feedbacks (i.e. sea-level rise) during the Last Interglacial (c. 130 to 115 ka BP) is crucial for refining model predictions of near future warming. However, Last Interglacial archives in Northern Europe are particularly challenging to date because they lie beyond the upper age limit of radiocarbon dating, and they lack anchored chronologies that extend to present day. A recently published reinvestigation of the annually varved Bispingen Palaeolake record (Lauterbach et al. 2024) suggested that the Last Interglacial actually lasted 4000 years longer than previously thought, as estimated using pollen zones. This study revisits the composite sediment succession in search of tephra, an independent dating and correlating method frequently used in Holocene-age sediments. This study first confirms the presence of cryptotephra shards in the Bispingen record, extracted from 70 5-cm thick low-resolution samples and from 29 1-cm high-resolution samples using a standard density separation technique (Blockley et al. 2005). This is followed by the discovery of five major tephra horizons, which were identified by their distinct shard concentration maxima. To understand the geochemistry of the tephra, the study also presents the results of Electron Microprobe Analysis from two tephra peaks. A rhyolitic population composed five tephra shards shows a distinct total high alkali signature (>10 wt%) that cannot be matched to any known Last Interglacial eruptions documented in North Atlantic marine cores. Total alkali and silica oxide comparison suggests that some trachytic shards may be associated with unknown Jan Mayen and Icelandic volcanism, although they differ in other Major element-oxide ratios. More Last Interglacial tephra studies in Northern Europe are needed to harness the chronostratigraphic potential of the tephra horizons found in this study, as linking sites together on the basis of a geochemically common tephra isochron will help constrain the regional timing of climate responses.

ABBREVIATIONS

Abbreviation	Definition
BC	before Christ
BP	before present
EMPA	Electron Micro-probe Analyser
ka	age - thousands of years
kyr	duration - thousands of years
LIG	Last Interglacial
Ma	age - millions of years
MIS	Marine Isotope Stage
NAO	North Atlantic Oscillation
OSL	Optically Stimulated Luminescence
PAZ	Pollen Association/Assemblage Zone
TAS	Total Alkali vs Silica
wt%	percent weight
IQR	Inter-Quartile Range
SD	Standard Deviation

TABLE OF CONTENTS

Title Page	i	
Authorization	ii	
Acknowledgements	iii	
Abstract	iv	
Abbreviations	v	
Table of Contents	vi	
List of Figures	x	
List of Tables	xv	
Chapter 1	Introduction	1
	1.1 Last Interglacial Climate Change	1
	1.2 Motivation for this Study	2
	1.3 Research Objective	3
	1.3.1 Identifying cryptotephra shards in the Bispingen sequence	3
	1.3.2 Classifying the geochemical signature of key tephra horizons	3
	1.3.3 Evaluating the potential use of tephra horizons to further Last Interglacial chronology in Northern Europe	3
	1.4 Thesis Structure	3
	1.5 Chapter Summary	4
Chapter 2	Literature Review	5
	2.1 The Last Interglacial	5
	2.2 Chronostratigraphy of Northwest Europe	7
	2.2.1 Last Interglacial deposits	7
	2.2.2 Eemian pollen assemblages	8
	2.3 Tephrostratigraphy	14

	2.3.1	Volcanism and climate	14
	2.3.2	Tephrochronology principles	15
	2.3.3	Dating tephra layers	17
	2.4	Central European Holocene Chronostratigraphy	18
	2.5	Comparable Tephra Archives	19
	2.5.1	Nordic tephras	19
	2.5.2	Eifel tephras	22
	2.5.3	Massif Central tephras	23
	2.5.4	Other tephras	24
	2.6	Summary	26
Chapter 3		Study Site	27
	3.1	Geographical Information	27
	3.2	Last Interglacial Climate in Lower Saxony	28
	3.3	Geological history of Lower Saxony	29
	3.3.1	Lower Saxony during the Last Interglacial and Weichselian glacial	29
	3.3.2	Lower Saxony during the Holocene	30
	3.4	Previous Work at Bispingen	31
	3.5	Summary	37
Chapter 4		Methodology	38
	4.1	Sampling Methods	38
	4.2	Cryptotephra extraction	38
	4.3	Microscopy and Shard Concentrations	40
	4.4	Identifying Tephra Peaks	42
	4.4.1	Shard Picking	44
	4.5	Geochemical analysis	45
	4.5.1	Stub Preparation	45
	4.5.2	Electron Microprobe Analysis	46
	4.5.3	Data Comparison	48
	4.6	Summary	50
Chapter 5		Results	51
	5.1	Shard Morphologies	51

5.2	Low-Resolution Shard Concentration Profiles	51
5.3	High-Resolution Shard Concentration Profiles	55
5.4	Geochemical Analysis	57
5.4.1	Raw Data	57
5.4.2	Normalised Data	61
5.5	Bispingen Pollen Record	65
5.6	Summary	68
Chapter 6	Discussion	69
6.1	Identifying cryptotephra shards in the Bispingen sequence	69
6.1.1	Tephra Peak H	70
6.1.2	Tephra Peaks G and F	70
6.1.3	Tephra Peak E	72
6.1.4	Tephra Peak D	72
6.1.5	Tephra Peak C	72
6.1.6	Tephra peak B	73
6.1.7	Tephra Peak A	73
6.2	Classifying the geochemical signature of key tephra horizons	74
6.2.1	LINK 16	75
6.2.2	MD99-2289	79
6.2.3	Volcanic zones and the possible origins of Bispingen tephra	85
6.3	Evaluating the potential use of tephra horizons to further Last Inter- glacial chronology in Northern Europe	93
6.3.1	Tephra horizons with weak chronostratigraphic potential	94
6.3.2	Tephra horizons with possible chronostratigraphic potential	94
6.3.3	Tephra horizons with strong chronostratigraphic potential	97
6.3.4	Limitations and uncertainties	97
6.4	Future Work	103
6.4.1	The Netherlands	104
6.4.2	Germany	106
6.4.3	France	107
6.5	Summary	109
Chapter 7	Conclusions	110
7.1	Key Findings	111

Chapter 8	Appendix	113
References		117

LIST OF FIGURES

- Figure 2.1 The past one million years of globally averaged deep sea benthic $\delta^{18}\text{O}$ data (retrieved from Lisiecki and Raymo 2005). The shaded box highlights the most recent 140 ka BP. The red section represents current Interglacial warming, the yellow section represents the Last Interglacial, regionally referred to as the Eemian Interglacial in Northwest Europe. The blue section represent cooler climate stadials in between the two interglacial maxima. 6
- Figure 2.2 Abundances of major pollen taxa in the Bispingen record from Lauterbach et al. 2024. 10
- Figure 2.3 Map of other Eemian pollen sites: [1] Bispingen, Germany (Müller 1974; Field, Huntley, and Muller 1994; Lauterbach et al. 2024) [2] Hollerup, Germany (Jessen and Milthers 1928) [3] Grobern (Litt, Junge, and Böttger 1996; Köhl et al. 2007) [4] Amersfoort (Zagwijn 1983) [5] Trockenmaar (Sirocko et al. 2005). 12
- Figure 2.4 Schematic showing how hypothetical tephra layers across the European continent may be correlated together if they share the same geochemically distinct tephra layer (each tephra isochron is represented as a different coloured section within the cores). 16
- Figure 2.5 Marine cores studied in Table 2.5. Iceland is located on the left of the map, and small volcanic island Jan Mayen can be found at the very top of the map. Bispingen and Northern Europe lie outside the geographic bounds of this map but are generally located in the far southeast direction. 20
- Figure 3.1 Simple map of Bispingen Palaeolake in Northern Germany. 27
- Figure 3.2 Cross-section of an inland Holocene sediment sequence that runs from the Elbe River to Buxtehude (From Streif 2004; Figure 13). The inset image in the bottom-right corner was taken from Figure 6 in Streif 2004 to show the position of the cross-section relative to the Elbe River in Lower Saxony, Northern Germany. Buxtehude is about 90 km southwest of the North Sea coastline, and relevant to this study, it is also about 50 km northwest of Bispingen Municipality. 31
- Figure 3.3 Topographical map of Bispingen Palaeolake sequence (zone 3 Cartesian Gauss-Kruger coordinates). Grey coordinate points represent the original sediment sequences Red coordinate points represent the new sediment sequence cored in 2000. Inset map depicts the location of Bispingen in Northwest Europe relative to other Last Interglacial proxy records discussed in Lauterbach et al. 2024. Source: Lauterbach et al. 2024; Figure 1; data from Lower Saxony Soil Information System (NIBIS) map server (Lower Saxony State Office for Mining, Energy and Geology, Hanover, Germany). 32

- Figure 3.4 Comparing the original KS186/70 sequence from Müller 1974 to the reinvestigated BIS-2000 sequence from Lauterbach et al. (2024). The updated sequence was extended by an additional siliclastics-organic layer (brown) in Unit 5 and an extended calcitic-diatomic layer through in Unit 3. Source: Lauterbach et al. 2024; Figure 7. 34
- Figure 3.5 Images of the core sections used in this study, including sections 9 and 1 of core BIS-1 and sections 8-11 of core BIS-3. Lower sections of these cores are associated with the Early Weischelian and not within the Last Interglacial scope of this study. The entirety of the BIS-2000 sequence is a combination of cores BIS-1 and BIS-3. Source: Lauterbach, pers comms. 35
- Figure 4.1 Workflow summarising the three main goals of this study (detailed further in Chapter 6) and specific methodologies for achieving these goals. 39
- Figure 4.2 Illustration summarising the laboratory procedures for identifying tephra shards. Cryptotephra preparation can be divided into three main steps: wet sieving the sample (left), density separating the size fraction between $15\mu\text{m}$ and $125\mu\text{m}$ using a heavy-liquid sodium polytungstate solution (middle), mounting the dense fraction between 1.95 g cm^{-3} and 2.51 g cm^{-3} onto microscope slides (top-right). Extracted cryptotephra shards are then ready to be counted at either 20x or 40 magnification under a microscope (bottom-right). 41
- Figure 4.3 Schematic of common tephra concentration profiles (adapted from Davies 2015). The stars indicate where the stratigraphic position of a tephra layer would be assigned in the hypothetical sediment records. 43
- Figure 4.4 IQR-based method for detecting outliers. The lower and upper bounds are determined based on the interquartile range. 44
- Figure 4.5 Standard deviation method for detecting outliers. Values more than 2 standard deviations away from the mean are considered outliers. 44
- Figure 4.6 Image of JEOL JXA-8230 Electron Microprobe Analyser (EMPA) located in the Electron Microscopy and Spectroscopy Centre of University of Leeds. 47
- Figure 4.7 Total alkali vs silica plot illustrating the silica to total alkali ratios of common igneous rocks. The exact boundaries and classifications for volcanic rocks come from Bas et al. 1992. Total alkali is defined as the combined % weight of Na_2O and K_2O . 49
- Figure 5.1 Comparison of clear tephra shards from Tephra Peak A in the low resolution sample between 2055 to 2050 cm. The shard in panel A is about $80\mu\text{m}$ on its longest axis, while the shard in panels B is $20\mu\text{m}$. The shards in panels A shows vesicular edges, while the shard in panel B has a more platy morphology. 52
- Figure 5.2 Low-resolution shard concentration profiles are shown on the top. Eight samples display distinct shard concentration maximums. Each colour corresponds to a specific tephra peak and its high-resolution shard concentration profile are shown in the inset figures below, where applicable. 54

- Figure 5.3 Geochemical bivariate plots of major-element data from Bispingen cryptotephra. All data presented are raw. Reference igneous rock classifications for total alkali vs. silica plot (top left) taken from Bas et al. (1992). Green data points (light and dark) are from Tephra Peak A in core BIS 1-9 and blue data points (light and dark) are from Tephra Peak C in core BIS 3-8. The cluster of dark green points in the top-right of the TAS is associated with Population A of Tephra Peak A. The two blue data points (one dark; one light) are associated with Population A of Tephra Peak C. Clustered shards are those that exhibit very similar geochemistries within the same sample. Population in this study is used a wider term for shards within the same sample whose comparable TAS geochemistries suggest they may come from the same volcanic origin. 59
- Figure 5.4 Images of analysed shards from five-shard cluster of Tephra Peak A. 61
- Figure 5.5 Geochemical bivariate plots of major-element data from Bispingen cryptotephra. All data presented are normalised to 100 wt%. Reference igneous rock classifications for total alkali vs. silica plot (top left) taken from Bas et al. (1992). Green data points (light and dark) are from Tephra Peak A in core BIS 1-9 and blue data points (light and dark) are from Tephra Peak C in core BIS 3-8. The cluster of dark green points in the top-right of the TAS is associated with Population A of Tephra Peak A. The two blue data points (one dark; one light) are associated with Population A of Tephra Peak C. Clustered shards are those that exhibit very similar geochemistries within the same sample. Population in this study is used a wider term for shards within the same sample whose comparable TAS geochemistries suggest they may come from the same volcanic origin. The individual points refer to the geochemical compositions of one individual shard, averaged if multiple measurements were taken. 62
- Figure 5.6 The left most figure shows the major sedimentological properties of the BIS-2000 sequence (data from Lauterbach et al. 2024). The grey calcitic + diatomic sediments are associated with Unit 4 and the tan diatomic sediments are associated with Unit 3 (also see Figure 3.4). The middle figure shows the percent abundances of common pollen taxa from the BIS-2000 sequence (data from Lauterbach et al. 2024). The right figure shows the low-resolution tephra shard concentration profiles collected in this study, separated between clear shards, brown shards, and the total of both shard colours. Pink represents the deepest pollen zone used in this study (PAZ IVb) and light blue represents the topmost pollen zone used in this study (PAZ VIb). The names of each tephra peak (E-A) are highlighted according to which pollen zone they are found in. Tephra Peak A is found at the beginning of PAZ Va, but there are some tephra layers below it that are also found in PAZ IVb. The remaining tephra peaks are not found as close to a transition between pollen zones and are easier to distinguish using the PAZ legend within the figure. 67
- Figure 6.1 Comparing the tephra from BIS-2000 (this study) to tephra populations found in the North Atlantic sequence LINK 16 (Abbott, Austin, and Davies 2014). The data from both studies are presented raw. 76

- Figure 6.2 Comparing the tephra from BIS-2000 (this study) to tephra populations found in the North Atlantic sequence LINK 16 (Abbott, Austin, and Davies 2014). The data from both studies are presented normalised and only shards with 95 wt% raw are included. 77
- Figure 6.3 Comparing the tephra from BIS-2000 (this study) to tephra populations found in the North Atlantic sequence MD99-2289 (Brendryen, Hafliðason, and Sejrup 2010). The data from both studies are presented raw. 80
- Figure 6.4 Comparing the tephra from BIS-2000 (this study) to tephra populations found in the North Atlantic sequence MD99-2289 (Brendryen, Hafliðason, and Sejrup 2010). The data from both studies are presented normalised and only shards with 95 wt% raw are included. 81
- Figure 6.5 Comparison of the tephra from BIS-2000 (this study) to tephra populations found in the North Atlantic sequence MD99-2289 (Brendryen, Hafliðason, and Sejrup 2010). Because one layer between 1856 to 1855 cm contained seven different populations, it is presented on a separate figure. Brendryen, Hafliðason, and Sejrup 2010 originally refers to this layer as 1855.5 a-f, with each letter denoting a distinct population. The same naming is used in the key found in the top right corner of the figure. The data from both studies are presented raw. 83
- Figure 6.6 Comparison of the tephra from BIS-2000 (this study) to tephra populations found in the North Atlantic sequence MD99-2289 (Brendryen, Hafliðason, and Sejrup 2010). Because one layer between 1856 to 1855 cm contained seven different populations, it is presented on a separate figure. Brendryen, Hafliðason, and Sejrup 2010 originally refers to this layer as 1855.5 a-f, with each letter denoting a distinct population. The same naming is used in the key found in the top right corner of the figure. The data from both studies are presented normalised and only shards with 95 wt% raw are included. 84
- Figure 6.7 Comparing the tephra from BIS-2000 (this study) to tephra proximal to the 2010 Eyjafjallajökull eruption in Iceland and to ultra-distal ash from the same eruption collected in Prague (Navratil et al. 2013). The data from both studies are presented raw. 86
- Figure 6.8 Comparing the tephra from BIS-2000 (this study) to tephra proximal to the 2010 Eyjafjallajökull eruption in Iceland and to ultra-distal ash from the same eruption collected in Prague (Navratil et al. 2013). The data from both studies are presented normalised and only shards with 95 wt% raw are included. 87
- Figure 6.9 From Titos et al. 2021 Figure 12: Concentration hazard map (Medium): relative epistemic uncertainties related with airborne ash cloud concentrations above 0.2 mg/m³, 2 mg/m³ and 4 mg/m³ and extent at 5000 feet (or 1.5 km). Each map corresponds to a different level of confidence, produced by cutting the hazard curves at different percentiles. 88
- Figure 6.10 Model-simulated trajectories of air masses created to reflect the transport of volcanic ash and dust from Eyjafjallajökull, Iceland to Prague after the 2010 eruption (Source: Navratil et al. 2013; Figure 1). 90

- Figure 6.11 Comparing the tephra from BIS-2000 (this study) to tephra layers found in Lake Monticchio, Italy, that are all linked to Italian eruptions during MIS 5e between 130 ka and 118 ka (Wulf et al. 2012). The data from both studies are presented raw. 91
- Figure 6.12 Comparing the tephra from BIS-2000 (this study) to tephra layers found in Lake Monticchio, Italy, that are all linked to Italian eruptions during MIS 5e between 130 ka and 118 ka (Wulf et al. 2012). The data from both studies are presented normalised and only shards with 95 wt% raw are included. 92
- Figure 6.13 Illustration depicting the ways external factors can affect the stratigraphic position of a tephra layer. The top half shows how climate and vegetation conditions affect tephra transport into a lacustrine environment, and the bottom half shows how conditions within a lake can affect tephra shards even after they settle in the sediment. 102
- Figure 6.14 Map of Northwest European sites with continuous Eemian Pollen records discussed in this section. 105

LIST OF TABLES

Table 2.1	General nomenclature for MIS 5 stadials, as commonly referred to in literature. The bottom row is the Last Interglacial.	8
Table 2.2	This table compares pollen assemblage zones (PAZ) across several Eemian sites in Northwest Europe. The first column of the most commonly used Eemian pollen zones from Zagwijn (1961) are used to correlate between sites. The last column in the table of the original Bispingen palaeolake record (Müller (1974)) is based on an earlier classification of pollen stages from Selle (1962).	13
Table 2.3	Common methods of directly radiometrically dating tephra crystals or indirectly dating the layer in which the tephra lies. Some rows are coloured simply to differentiate between multiple methodologies in the table. Adapted from Encyclopedia of geoarchaeology (Lane and Woodward 2022).	17
Table 2.4	Common methods of directly radiometrically dating tephra crystals or indirectly dating the layer in which the tephra lies. Some rows are coloured simply to differentiate between multiple methodologies in the table. Adapted from Encyclopedia of geoarchaeology (Lane and Woodward 2022).	17
Table 2.5	Summary of Icelandic tephra deposits. Leftmost column lists previously identified tephra horizons. Second column provides the associated MIS 5 interval of each tephra layer. Third column provides the estimated age of each tephra layer in ka BP. All eruptions are from Iceland, and their rock suite affinities are specified alongside the major composition of the deposit, where applicable. References [1] Abbott, Austin, and Davies 2014 [2] Davies et al. 2014 [3] Wastegård and Rasmussen 2001 [4] Sjøholm, Sejrup, and Furnes 1991 [5] Fronval et al. 1998 [6] Sejrup et al. 1989 [7] Brendryen, Hafliðason, and Sejrup 2010 [8] Abbott et al. 2013 [9] Abbott et al. 2011. The highlighted blue tephra layers are isochronous layers that are geochemically linked to the same eruption.	21
Table 2.6	Tephra traced to Eifel Volcanic Zone, Germany. References [1] Sirocko et al. 2005 [2] Bogaard and Schmincke 1990 [3] Pouclet, Juvigné, and Pirson 2008 [4] Gewalt and Juvigné 1986 [5] Sirocko et al. 2016 [6] Zöller and Blanchard 2009 [7] Leyk and Lippolt 1999 [8] Woda, Mangini, and Wagner 2001 [9] Frechen and Lippolt 1965 [10] Meyer 1994 [11] Preusser, Rufer, and Schreurs 2011).	23
Table 2.7	Tephra deposits associated with Massif Central Volcanism, France.	24

Table 2.8	List of all known volcanic eruptions from Italy during MIS 5. The blue highlighted section consists of different tephra deposits all associated with a singular eruption from c. 106 ka. The green highlighted section consists of different tephra deposits all associated from a singular eruption from c. 107 ka. Both widespread tephra layers have only been found near or in the Mediterranean Sea. The majority of Italian tephra deposits from MIS 5, especially during MIS 5e, are recorded from the varved sediments in Lake Monticchio. For more detailed information on Italian eruptions and tephra deposits in Southern Europe from this lake see [1] Wulf et al. 2012. Other References [2] Giaccio, Nomade, Wulf, et al. 2012 [3] Paterne, Guichard, Duplessy, et al. 2008 [4] Keller et al. 1978 [5] Vogel et al. 2010.	25
Table 3.1	Columns (left to right) detail the depths, primary content, and lacustrine interpretation for each distinct sedimentary unit from BIS-2000 (Lauterbach et al. 2024).	33
Table 3.2	Estimated length of each pollen zone from core KS 186/70 and BIS-2000. The rightmost column notes whether the varves were easy to count or whether they were estimated indirectly using the thickness of layers. References [1] PAZ from Zagwijn 1961 [2] PAZ from Selle 1962 [3] KS 186/70 core from Müller 1974 [4] BIS-2000 first from Lauterbach et al. 2024 and used in this study.	36
Table 4.1	Batches refers to the samples that were processed in the same group (i.e. washed, centrifuges, density separated, counted, etc. at the same time).	38
Table 5.1	Table showing the eight tephra peaks. selected for high-resolution analysis. The letters assigned to each peak are given in the left most column. The depths for each 5 cm sample are given in the middle-left columns. The shard concentration within each sample, in shards/g, are given in the middle-right column. The shard concentration was calculated using the total number of shards divided by the dry weight of the entire sample. The final column gives the statistical method used for identifying each tephra peak.	52
Table 5.2	Table of the major element oxides raw wt%. The samples listed in the first column follow the format of sample#_shard#. Where multiple measurements could be taken from the same shard, these numbers are already averaged in the table. Sample 196 is Tephra Peak A Population A; Sample 195 is Tephra Peak A Population B; Samples 184 are Tephra Peak C Population A; Samples 183 is Tephra Peak Population B. The final two rows are the averaged measurements of the ML3B and Lipari standards used to calibrate periodically between measurements. Sample 195_S6 was deemed not tephra on the basis of its usually high Iron content and was removed from further analysis, but it is still shown in the table. All other shards were used in analysis.	60

Table 5.3 Table of normalised major element data, using the raw data and adjusting the analytical totals to 100 wt%. The samples listed in the first column follow the format of sample#_shard#. Where multiple measurements could be taken from the same shard, these numbers are already averaged in the table. Sample 196 is Tephra Peak A Population A; Sample 195 is Tephra Peak A Population B; Samples 184 are Tephra Peak C Population A; Samples 183 is Tephra Peak Population B. The final two rows are the averaged measurements of the ML3B and Lipari standards used to calibrate periodically between measurements. Sample 195_S6 was deemed not tephra on the basis of its usually high Iron content and was removed from further analysis, but it is still shown in the table. All other shards were used in analysis.

CHAPTER 1

INTRODUCTION

This chapter introduces current limitations in dating Last Interglacial archives and how tephrostratigraphy can improve these records to better understand Earth's natural warming responses. This chapter also discusses motivations for this study and its primary objectives.

1.1 Last Interglacial Climate Change

The Last Interglacial (c. 130 to 115 ka) is the most recent warm period prior to the current interglacial, with arctic summer temperatures nearly 4-5 °C higher than the Arctic today (Kaspar et al. 2005; Members 2006). While greenhouse gases were comparable to pre-industrial values (Lüthi et al. 2008), summer solar insolation and warming increased during the Last Interglacial likely because of a difference in orbital parameters (Laskar et al. 2004; Guarino et al. 2020). The Milankovitch cycles, or changes in the earth-sun position over thousands of years, drives solar insolation, especially at higher latitude regions like Northern Europe (Milankovitch 1941; Otto-Bliesner et al. 2021). Studying the full glacial-interglacial cycle provides insight into earth system responses, such as sea-level rise and vegetation successions, which are essential for distinguishing between natural climate variations and those influenced by human activities. A better understanding of natural climate variability is crucial for refining climate model predictions, particularly in the context of ongoing anthropogenic warming (Vera et al. 2013).

While the Last Interglacial is globally defined by warmer sea surface temperatures and higher sea levels (Shackleton 1987; Kopp et al. 2009; Dutton et al. 2015; DeConto et al. 2021; Fox-Kemper et al. 2021), it regionally differs in its onset and timing in the palaeorecord. The Last Interglacial, and the smaller climate stadials that follow it, can also be referred to by local nomenclature that varies by region (Table 2.1). It is widely accepted that the Eemian Interglacial, the regional name for the Last Interglacial pollen records in Northwest Europe, is broadly associated with MIS 5e (Shackleton et al. 2003). The regional significance of the Eemian period is particularly critical for low-lying areas like the Netherlands, which are at risk from rising sea levels. In parts of the Netherlands and even other parts of Northern Europe, many Eemian records lie in basins carved by preceding glacial retreat during MIS 6 (Jessen and Milthers 1928; Mangerud

1989). These well-preserved deposits, including the annually resolved Bispingen Palaeolake sequence in Northern Germany (Müller 1974; Lauterbach et al. 2024), provide knowledge of the Last Interglacial and its regional responses. Although Eemian deposits improve our understanding of the climate system, they are challenging to date within the wider geologic record. This work addresses a possible method for constraining the timing of Last Interglacial climate change in Northwest Europe.

1.2 Motivation for this Study

This study is the first use of volcanic ash (tephra) as a stratigraphic tool in the Last Interglacial records of Northern Europe. Tephra is commonly used as a geochronologic tool in Late Quaternary studies but is less explored in time periods older than the Last Glacial cycle (e.g. Lane et al. 2015). Tephra, well-preserved in varved sediments, can produce a high resolution framework for the timing and rates of climate responses with no upper age limit (Lowe 2011). Recent developments in tephrochronological research, including the discovery of microscopic glass shards known as cryptotephra, provide a unique opportunity to trace volcanic eruptions several thousand kilometres away from their source (Davies 2015; Bilt, Lane, and Bakke 2017). Previous Last Interglacial studies in the Arctic and the North Atlantic (e.g. Fronval et al. 1998; Sjøholm, Sejrup, and Furnes 1991; Abbott et al. 2011) have proven how tephra shards are an effective tool for absolutely dating individual sedimentary records and linking them together. Being able to identify a source eruption opens the door for correlating sediment sequences over continental distances to resolve warming responses between regions (Lowe 2011). Because Last Interglacial sediments lie beyond the upper limit of radiocarbon dating, and those in Northern Europe cannot be linked to the larger marine isotope record, precisely dating the Eemian Interglacial is mainly limited to correlating pollen assemblages with each other (Zagwijn 1996), which can solidify the duration of vegetation phases but cannot estimate their absolute ages in time. There is a strong need to revisit the annually laminated Bispingen Palaeolake sequence with a new approach for correlating Eemian pollen assemblages. Because the palaeolake site in Northern Germany is located downwind of many active volcanic zones, there is great potential for the high-resolution sequence to preserve multiple tephra archives across the continent.

1.3 Research Objective

The wider objective of this project is to create the first terrestrial tephra record for the Last Interglacial in Northern Europe. The tephra record will be established by achieving three benchmark goals, listed below and detailed further throughout this thesis.

1.3.1 Identifying cryptotephra shards in the Bispingen sequence

The large majority of laboratory work focuses on identifying non-visible tephra shards (cryptotephra) within palaeolake sediments. The cryptotephra layers provide the opportunity to trace volcanic eruptions even when ash is found thousands of kilometres away from their source.

1.3.2 Classifying the geochemical signature of key tephra horizons

The latter stages of laboratory work involve extracting individual tephra shards and measuring their major element concentrations. By classifying the possible source of tephra through its unique geochemical signature, it can serve as a stratotype by which future cryptotephra layers in Northwest Europe may be compared to.

1.3.3 Evaluating the potential use of tephra horizons to further Last Interglacial chronology in Northern Europe

The research aims to investigate the use of volcanic ash (tephra) as a regional chronostratotype in Northern Europe. Tephra can date climate responses in the geologic record without an upper age limit, especially when it is found in high-resolution archives, like varved sediments. This thesis represents the early stages of a comprehensive Last Interglacial tephra framework and holds immense potential to refine the timing and rates of warming in future climate models.

1.4 Thesis Structure

This thesis is comprised of seven chapters. Chapter one is a brief introduction to the Last Interglacial period in Northwest Europe. Chapter two is a literature review addressing current understand of Eemian chronology and possible sources of tephra in Europe. Chapter three provides specific geographical information of Bispingen Palaeolake and previous studies conducted there. Chapter four justifies the methodological practices for isolating, extracting, and geochem-

ically measuring tephra shards. Chapter five provides shard concentration profiles for the upper Bispingen sequence and major element data from two Bispingen tephra layers. Chapter six discusses the possible sources and transport mechanisms for tephra found in Bispingen and the strength of these records within the wider context of creating a regional framework. Chapter seven reflects on the three primary objectives and concludes the paper.

1.5 Chapter Summary

Last Interglacial warming is notably similar to global temperatures observed today, and even predicted in the near future. Understanding the rates and timing of climate change during the Last Interglacial can provide invaluable knowledge on current warming. However, Last Interglacial sequences, especially in Northwest Europe, are difficult to precisely date. Previous studies from the North Atlantic justify the use of tephrostratigraphy for identifying widespread chronostratigraphic markers during the Last Interglacial, and these time-linked tephra layers have potential to be found in this study.

CHAPTER 2

LITERATURE REVIEW

This chapter is a literature review of the floating pollen assemblages that comprise the Pollen Assemblage Zones of the Eemian Interglacial. This chapter also justifies the use of tephra as a geostatigraphic tool for synchronising floating archives. It also introduces ways volcanic ash has previously been used as both a geochronological and geostatigraphic tool. While this study focuses more on the correlative power of tephra records rather than absolutely dating individual tephra shards, both have potential to refine the Eemian pollen record from Bispingen Palaeolake. This chapter discusses how Central European tephra records have already been used to resolve the timing of abrupt climate change during the Holocene and how similar methods may be effective for constraining the age of the Last Interglacial. The last part of this chapter lists possible volcanic sources of Bispingen tephra and their known eruptions during MIS 5.

2.1 The Last Interglacial

In recent geologic history over the past 800 kyr, well-defined periods of climate fluctuated between increased global ice volume (glacials) and decreased global ice volume (interglacials) (Figure 2.1 Cohen and Gibbard 2019). The 100 kyr glacial-interglacial cycles highlight the natural and predictable shifts in ice sheets and vegetation ranges. Because glacial and interglacial periods are marked by long-term ice, ocean, atmosphere, and vegetation changes across great distances, there is often distinct regional variability.

This study focuses on the Last Interglacial, the last time Earth experienced mild interglacial conditions prior to today. While Last Interglacial temperatures are comparable to near future warming, the drivers of climate change between the two periods are fundamentally different. Current global warming is overwhelmingly the result of rapid anthropogenic greenhouse gas emissions which reradiate and trap heat in the atmosphere (IPCC 2021). Instead, Last Interglacial warming was primarily driven by a larger eccentricity value in which Earth had a more elliptical orbit around the sun resulting in distinct seasonal variations and anomalously warmer summers (Milankovitch 1941; Otto-Bliesner et al. 2021). The cyclical nature of past interglacials is largely driven by these orbital parameters, or predictable shifts in the geometry of the Earth's

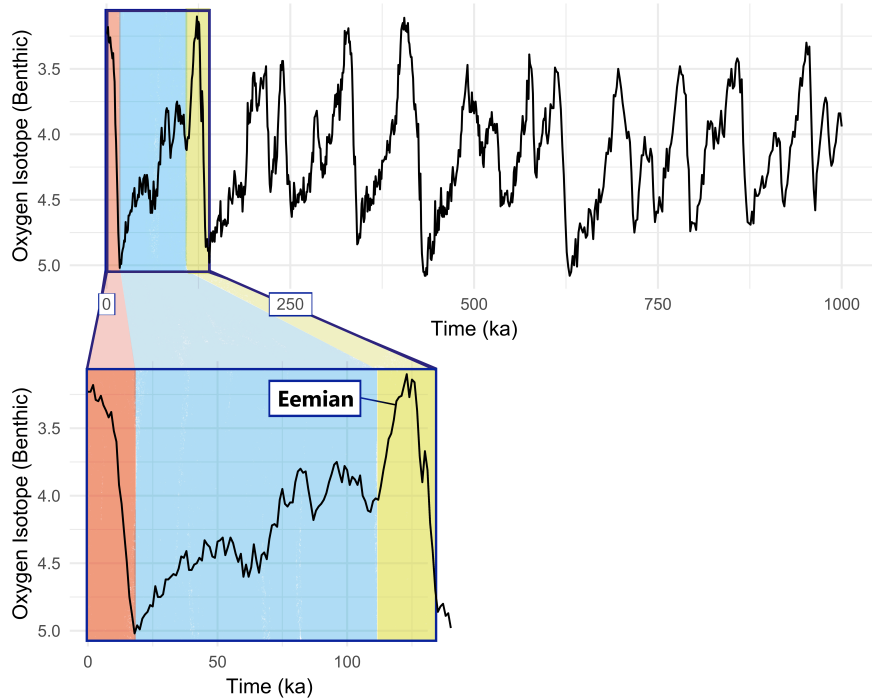


Figure 2.1: The past one million years of globally averaged deep sea benthic $\delta^{18}\text{O}$ data (retrieved from Lisiecki and Raymo 2005). The shaded box highlights the most recent 140 ka BP. The red section represents current Interglacial warming, the yellow section represents the Last Interglacial, regionally referred to as the Eemian Interglacial in Northwest Europe. The blue section represent cooler climate stadials in between the two interglacial maxima.

orbit and axis (Milankovitch 1941; Hays, Imbrie, and Shackleton 1976; Imbrie et al. 1984). The position of Earth and its axis relative to the sun affects the seasonal distribution of net solar radiation (insolation) across latitudes (Berger, Loutre, and Mélice 2006). For this reason, insolation differences, and therefore changes in climate, are felt more dramatically at higher latitude regions, such as Northern Europe. However, only models that consider both melting of ice sheets and external orbital factors show colder surface waters in the North Atlantic around 126 ka (Govin and al. 2015). Otherwise stated, orbital factors alone are not enough to produce the slowed thermohaline circulation observed marine sediment data from at the start of Last Interglacial.

As Northern Europe experiences more intense Earth system responses than lower latitudes, there is a specific need to refine climate feedback models within these high latitude regions. In the context of this study, Earth system responses are the environmental feedbacks to orbital driven climate change during the Last Interglacial. Last Interglacial Global Mean Sea Level (GMSL) rise, caused by thermal expansion of water, melting continental mountain glaciers, and melting polar ice sheets (Dutton et al. 2015), was at least several meters higher than today (IPCC 2021). The significant increase in sea level is especially hazardous to low lying countries

in Northern Europe, like the Netherlands (IPCC 2019). Reconstructing past climate feedbacks, and therefore future sea level rise models for the Netherlands, relies on knowing the timing and rates of these changes (IPCC 2019). The rates of Last Interglacial climate feedback responses in Northern Europe are widely based on pollen sequences that preserve regional vegetation successions. For example, Otto-Bliesner et al. (2021) developed a comparison model of orbital driven warming between 127.8 ka and pre-industrial warming. The model relied on European floating pollen sequences through interpolating ages from marine sequences. Assigning relative ages increases underlying uncertainties, but incorporating cryptotephra analysis within a pollen record will greatly support the effectiveness and accuracy of future climate models by directly anchoring the ages of these regional pollen sequences. This chapter explores the need for cryptotephra analysis to improve Last Interglacial chronologies, facilitating more robust model-data comparisons.

2.2 Chronostratigraphy of Northwest Europe

2.2.1 Last Interglacial deposits

Although the Eemian period was named after pollen sequences from the Eem river in the Netherlands, this term is generally used to refer to the Last Interglacial from the Netherlands to Western Russia (Harting 1874) and is often used in the broader literature (e.g. members 2013; Table 2.1). Northern Europe is abundant in paleolake records that formed in various stages of ice retreat during the Late Pleistocene. The Saalian Ice sheet in the glacial period (MIS 6) preceding the Eemian (MIS 5e) covered the Netherlands and parts of Northern Germany (1983 n.d.; Leeuwen et al. 2000; Beets, Beets, and Cleveringa 2006). Last Interglacial deposits accumulated in lake basins and meltwater channels left behind by Saalian ice sheet retreat, and they are still accessible today because the Weischelian ice sheet in the Last Glacial period (MIS 4), following the Last Interglacial, did not extend far enough south to override sediment (Turner 2000). Well-preserved Last Interglacial sediment archives are essential for resolving the timing and rates of Eemian-warming responses. To resolve larger warming responses, the rates of Eemian climate change need to be linked to other regions, such as Southern Europe or the North Atlantic. However, Eemian pollen archives lie beyond the upper limit of radiocarbon dating, so they can only be relatively correlated between each other with no absolute dates to tie them together.

Table 2.1: General nomenclature for MIS 5 stadials, as commonly referred to in literature. The bottom row is the Last Interglacial.

MIS	Germany	France	Britain	Regional
5a	Odderade	St Germain II	Brimpton	
5b	Rederstall	Melisey 2	Wolstonian	Early Weichselian
5c	Brørup	St Germain I	Chelford	
5d	Herning	Melisey 1	Herning	
5e	Eemian	Lure	Ipswichian	Eemian

2.2.2 Eemian pollen assemblages

Both the magnitude and duration of a warming event influence vegetation development and the migration of plant species. The power of palaeobotanical data, such as pollen assemblages, lies in the climatological thresholds that must be met for tree and plant species to survive and reproduce (Kershaw and Nix 1988). The presence of particular plants or forests in a pollen record typically indicates that temperature and precipitation levels were once within the minimum range required for their widespread abundance. The strong relationship between vegetation growth and favourable regional climate conditions facilitates past climate reconstructions (Väliranta et al. 2009). Pollen archives are especially abundant in Northern Europe and provide the predominant understanding of regional climate responses.

So far, the onset and timing of the Eemian Interglacial is based on several well-studied pollen sequences in Northwest Europe. Many of these palynological studies reveal several distinct vegetation phases throughout the Eemian period (Table 2.2). The vegetation phases, or Pollen Association Zones (PAZ), represent major tree successions across Europe and can sometimes measure Eemian palaeotemperatures in addition to their chronological use. Zagwijn (1996) compared regional pollen records from 31 sites across Northern Europe and found that the general tree successions between the Netherlands (Zagwijn 1961; Zagwijn 1983), Poland (Mamankowa 1989), and Germany (Müller 1974; Menke and Tynni 1984; Litt 1990) show broadly similar taxa abundances and durations despite some regional variations. The PAZ described by Zagwijn, 1961 and 1983 are denoted by the letter E and followed by their corresponding number from E1 through E7 (Table 2.2; Turner and West 1968; Menke and Tynni 1984; Litt, Junge, and Böttger 1996). While the Dutch pollen zonations do not exactly line up with the German PAZ used in this study, their relative equivalences are given in Table 2.2.

In the late glacial phase (E1) the landscape was dominated by birch woodland. In the following Early-Temperate phase pine expanded into pine-birch forests (E2), oak expanded into pine-mixed oak forests (E3), and the pine and birch taxa decreased as oak-hazel forests dominated

by the start of the climatic optimum (E4). By the Late Temperate phase and peak interglacial warmth (E5), the prevailing forest taxa were hornbeam and spruce. The Post-Temperate phase (E6) into the following Early Glacial period (E7) saw boreal forests of pine, spruce, and fir expand. The Eemian pollen succession is generally agreed upon across several sites in Northwest Europe, with pollen zones E4 and E5 occurring at the interglacial maximum (Turner and West 1968; Menke and Tynni 1984; Litt, Junge, and Böttger 1996). As a whole, the general overlap of common pollen successions between sites highlights the geographically consistent changes in climate during the Last Interglacial, but there is some disagreement regarding the Eemian Interglacial and its absolute timing in Europe (Tzedakis 2003; Govin and al. 2015). As the spread of Eemian pollen sequences ranges from the Netherlands to western Russia, there is still some regional variability in between. Litt, Junge, and Böttger (1996) identified a minor climate oscillation during the peak warmth in pollen phase E5 from a partial replacement of spruce by pine and by a lower water level. A similar oscillation was observed in Bispingen Palaeolake sequence (Field, Huntley, and Muller 1994). While the arboreal phases are generally consistent between Northeast German sites (Menke and Tynni 1984; Litt, Junge, and Böttger 1996; Lauterbach et al. 2024) there is still some debate regarding climate stability and timing during the Last Interglacial.

Debate regarding the timing of the Last Interglacial considers whether there was an early or late onset of interglacial warming. In the early onset scenario, pollen zone E1 began around 129 ka in line with Southern European speleothem and offshore marine records (Shackleton et al. 2002; Tzedakis et al. 2018). In this case, there was only small lag between warming in Southern Europe and subsequent warming Northern Europe. In the late onset scenario, however, pollen zones E1 through E6 lasted from 125.5 ka to 112.5 ka., suggesting a diachroneity between Northern and Southern Europe in which warmer forested climate conditions persisted much longer in the south (Tzedakis 2003; Sánchez-Goñi et al. 2002). In this case, the extent of forests decreased in Northern Europe by 115 ka in response to lower summer temperatures, while forests eventually decreased in Southern Europe by 110 ka due to lower moisture availability, triggered by ice rafting and subsequent slowing of thermohaline circulation (Tzedakis 2003). While this may explain climate deterioration into MIS 5d, it still does not answer exactly when deglaciation from MIS 6 ended and when the Last Interglacial began in Europe.

Last Interglacial sequences are difficult to accurately date because they predate the upper limit for radiocarbon dating (c. 55ka BP; Heaton 2022). Eemian pollen assemblages are floating so they can only be aligned either to each other or to other radiometrically dated chronologies (e.g. U-Th dated cave deposits; Tzedakis et al. 2018); however, there are so few

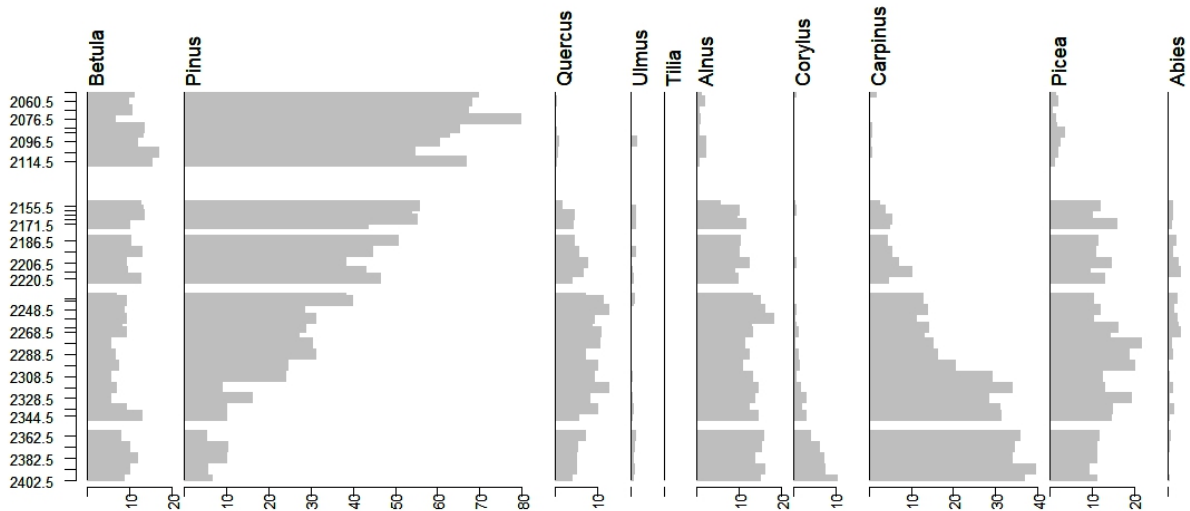


Figure 2.2: Abundances of major pollen taxa in the Bispingen record from Lauterbach et al. 2024.

absolutely dated Eemian archives that using them to link pollen assemblages together is challenging (Govin and al. 2015). While OSL and palaeomagnetism could be used to constrain Eemian archives, these dating methods are associated with large uncertainties (Ster et al. 2015; Seiriene et al. 2021). In contrast, the Last Interglacial in Southern Europe is dated using continuous marine records such (e.g. Iberian Margin; Shackleton et al. 2002) and varved terrestrial records (e.g. Lago Grande de Monticchio; Wulf et al. 2012). In general, palynological data is especially limited by a lack of complete sequences that span the entire Eemian period through the Holocene and present day (Kühl et al. 2002).

The first attempt to estimate the length of the Last Interglacial in Northern Europe comes from Bispingen Palaeolake, an annually varved palaeolake in Northern Germany (Figure 6.14). While the 11 ka estimate from the original Bispingen Palaeolake record is synonymous with the duration of MIS 5e, the varves are poorly preserved towards the top of the core leading to uncertainty (Müller 1974). When Kukla et al. (1997) aligned the French Grand Pile pollen record (Woillard 1978) to North Atlantic marine records (McManus et al. 1994), they estimated a much longer Last Interglacial period from 130 ka to 107 ka. This 23-ka period of warmth would extend far into MIS 5d if it were correlated with the marine record, suggesting that the Last Interglacial in Europe lasted more than double what was originally observed by Müller (1974). Since Kukla et al. (1997) challenged the original duration of the Last Interglacial, several successive studies have revisited this issue. Shackleton et al. (2002) produced a high-resolution pollen record from an offshore site near Portugal. Because the pollen stratigraphy was recorded in marine sediments, it was directly anchored to the well-dated $\delta^{18}\text{O}$ planktonic records. From this, Shackleton et al. (2002) estimated Last Interglacial timing between 126 ka and 110 ka, or 16 kyr in length. This

range is 5 kyr longer than the original Bispingen Palaeolake estimate of 11 kyr (Müller 1974), but shorter than the proposed 23 ka estimate from Le Grande Pile, contributing to more uncertainty in regards to climate stability between Northern and Southern Europe

Many subsequent pollen assemblages are still compared to the original Bispingen Palaeolake pollen record by Müller (1974), but the record was only recently contested in a recent study by Lauterbach et al. (2024) that revisited the Bispingen Palaeolake varve chronology and re-estimated the length of the Eemian Interglacial from 11 to 15 kyr, in closer agreement with Southern Europe. While the findings from the 2024 study will be discussed with greater detail in Chapter 3, it concludes that the Last Interglacial warming in Northern Europe lasted 4000 years longer than previously suggested by Müller 1974. Although the original Bispingen Palaeolake dataset supports a steep vegetation gradient between Northern and Southern Europe, the recent findings suggest a weaker climate gradient. Little-to-no climate lag between the two halves of Europe suggests that the synchronous warming may have been caused by a rapid Scandinavian deglaciation process. Faster ice sheet melt further implies that the preceding MIS 6 ice sheet was comparable in size with MIS 2 ice sheet from the Last Glacial Maximum, impacting how the Last Interglacial can be used as an indicator of relative sea level rise in response to near future deglaciation and warming (Lambeck et al. 2006; Kopp et al. 2009; Long et al. 2015; Cohen et al. 2022). Using the same sediment cores as Lauterbach et al. 2024, this study has the potential to confirm these findings by creating a tephra framework between European pollen assemblages and assessing the synchronicity of pollen responses across the region.



Figure 2.3: Map of other Eemian pollen sites: [1] Bispingen, Germany (Müller 1974; Field, Huntley, and Muller 1994; Lauterbach et al. 2024) [2] Hollerup, Germany (Jessen and Milthers 1928) [3] Grobern (Litt, Junge, and Böttger 1996; Kühl et al. 2007) [4] Amersfoort (Zagwijn 1983) [5] Trockenmaar (Sirocko et al. 2005).

Table 2.2: This table compares pollen assemblage zones (PAZ) across several Eemian sites in Northwest Europe. The first column of the most commonly used Eemian pollen zones from Zagwijn (1961) are used to correlate between sites. The last column in the table of the original Bispingen palaeolake record (Müller (1974)) is based on an earlier classification of pollen stages from Selle (1962).

Author Site	Zagwijn (1963) Netherlands	Zagwijn (1983) Netherlands	Menke and Tynni (1984) Rederfall	Mamakowa (1989) Imbramowice	Litt (1994) Grobern	Selle (1962)	Müller (1974) Bispingen palaeolake
E1	Betula-Pinus	Betula	Betula	Pinus-Betula	Betula	I	Betula-Pinus
E2	a Pinus-Ulmus b Pinus	Pinus	Pinus-Betula	Pinus-Betula-Ulmus	Pinus-Betula	IIa	Pinus-Betula
E3	a Quercus b Quercus-Corylus	Quercus-Ulmus	Pinus-Quercetum mixtum	Quercus-Fraxinus -Ulmus	Pinus-Quercetum mixtum	IIb	Pinus-Quercetum mixtum
E4	a Corylus b Taxus	Corylus Corylus-Taxus	Quercetum mixtum-Corylus Corylus-Taxus-Tilia	Corylus-Quercus-Tilia	Quercetum mixtum-Corylus Corylus-Taxus-Tilia	IIIa+b IIIc	Quercus mixtum-Corylus-Tilia
E5	a Carpinus b Pinus-Carpinus	Carpinus Pinus-Carpinus	Carpinus-picea	Carpinus-Picea-Alnus	Carpinus	IV	Carpinus
E6	a Pinus-Picea b Pinus	Pinus-Picea Pinus	Pinus-Picea-Abies	Pinus-Picea-Abies	Carpinus-Abies Pinus-Picea-Abies	Va Vb VI	Pinus-Picea-Carpinus Pinus-Picea-Abies Pinus
E7			Pinus	Pinus	Pinus		

2.3 Tephrostratigraphy

Far-travelling volcanic debris called tephra may be used to correlate (tephrostratigraphy) or to date (tephrochronology) sedimentary sequences, becoming an increasingly important tool for linking asynchronous palaeoclimate records together in time (Davies 2015; Lowe 2011). Icelandic volcanologist Thórarinnsson (1954) first defined the word tephra, derived from the Greek word for ash (Lowe 2011). Tephra can have a very general meaning, encompassing volcanic debris of any size, shape, or density (Lowe 2011). Heavier debris is transported short distances and tends to fall very close to its volcanic source (Folch 2012). However non-visible cryptotephra, the prefix crypto- derived from the Greek word for hidden, is lighter and can be transported greater distances (Land and Woodward, 2016; Lowe 2011). When a volcanic event is present in multiple records, the common age of the eruption is called an isochron (Lowe 2011). Cryptotephra isochrons offer a means to compare marine, terrestrial, and ice cores on the same geologic timeline when these records would otherwise be dated using methods relative to their source.

Widespread cryptotephra dispersal, which underpins the success of tephrostratigraphy, is typically associated with highly explosive eruptions. In some very large eruptions, an ash column can reach into the stratosphere (20 km in altitude), where strong atmospheric winds carry the silt-sized glass shards several thousand kilometres from their source. In a notable example of this phenomena, work on varved lake sediments in Poland found cryptotephra deposits originating from Iceland, Azores, and even Alaska (Kinder et al. 2020). Ultra-distal glass shards are well-preserved in varved sediments, so even very distant volcanic eruptions may be detected in annual resolutions. There is a clear potential for ash to travel thousands of kilometres under the right atmospheric and eruptive conditions, and tephra from a single eruption can be found across multiple sites in Europe, justifying this work.

2.3.1 Volcanism and climate

Understanding the broader context of ash dispersal requires examining the relationship between volcanism and climate, particularly in how tephra is transported under varying meteorological conditions. Long-term climate phases can affect the frequency and magnitude of tephra-producing eruptions. During interglacial and glacial phases, these factors can vary greatly, leading to distinct patterns of tephra dispersal. The dynamics of tephra dispersal are essential for reconstructing past volcanic events and their impacts on the environment. For example, ice

unloading in deglaciation periods often leads enhanced mantle decompression melting (Aubry et al. 2022) and therefore temporarily increased volcanic events. By climatic optimums and peak interglacial conditions, the period of rapid ice melt and subsequent unloading has already passed, so volcanism tends to slow (Aubry et al. 2022). In lower latitude eruptions especially, increased tropopause height with a warming climate reduces the number of volcanic ash columns that are able to reach the stratosphere and thus be transported to ultra distal sites (Aubry et al. 2016, Aubry, Cerminara, and Jellinek 2019). While eruption columns may only reach lower altitudes in warmer climates, increased precipitation and interaction with water could increase the frequency of highly explosive volatile induced and phreatomagmatic eruptions (Gill and Fitton 2010).

Shorter term climatic factors, like wind patterns and precipitation, directly affect tephra transport at the time of eruption (Watson et al. 2016). Tephra dispersal in Europe is largely dependent on persistent westerly winds in the lower stratosphere (Bilt, Lane, and Bakke 2017, Olafsson and Rousta 2021). Tephra originating from Iceland is also controlled by seasonal shifts in wind direction above 15 km altitude where the westerly winds become stronger in the fall and winter (Lacasse 2001). Climate phases overlapping an eruption will have an affect on the direction in which tephra travels, especially in Iceland (Lacasse 2001). One of the largest modulators of climate in Northwest Europe is the decadal NAO oscillation, a key atmospheric pressure gradient that affects temperature and precipitation levels in Europe (Martin-Garcia 2019). In its positive phase, there is a strong pressure gradient from the Azores to Iceland, causing warm, moist air over the Azores to advect northeast. In its negative phase, there is a weaker pressure gradient between these two air mass systems, causing air from Iceland to advect south towards Northern Europe (Martin-Garcia 2019). Initial tephra transport from a volcano is based on the combined effects of seasonal winds and regional climate cycles that influence both the physical transport of shards themselves in addition to setting thresholds for the maximum heights of eruption columns.

2.3.2 Tephrochronology principles

Tephra as a geochronological tool relies on several assumptions, outlined by Lowe (2011). First, the time between a volcanic eruption and the time at which tephra is deposited in the sedimentary record is negligible relative to geologic time (Lowe 2011). In the case of tephrostratigraphic frameworks derived from marine records, tephra layers deposited by ice-rafting are excluded as age markers due to their very long transport times in the deep ocean (Abbott, Austin, and

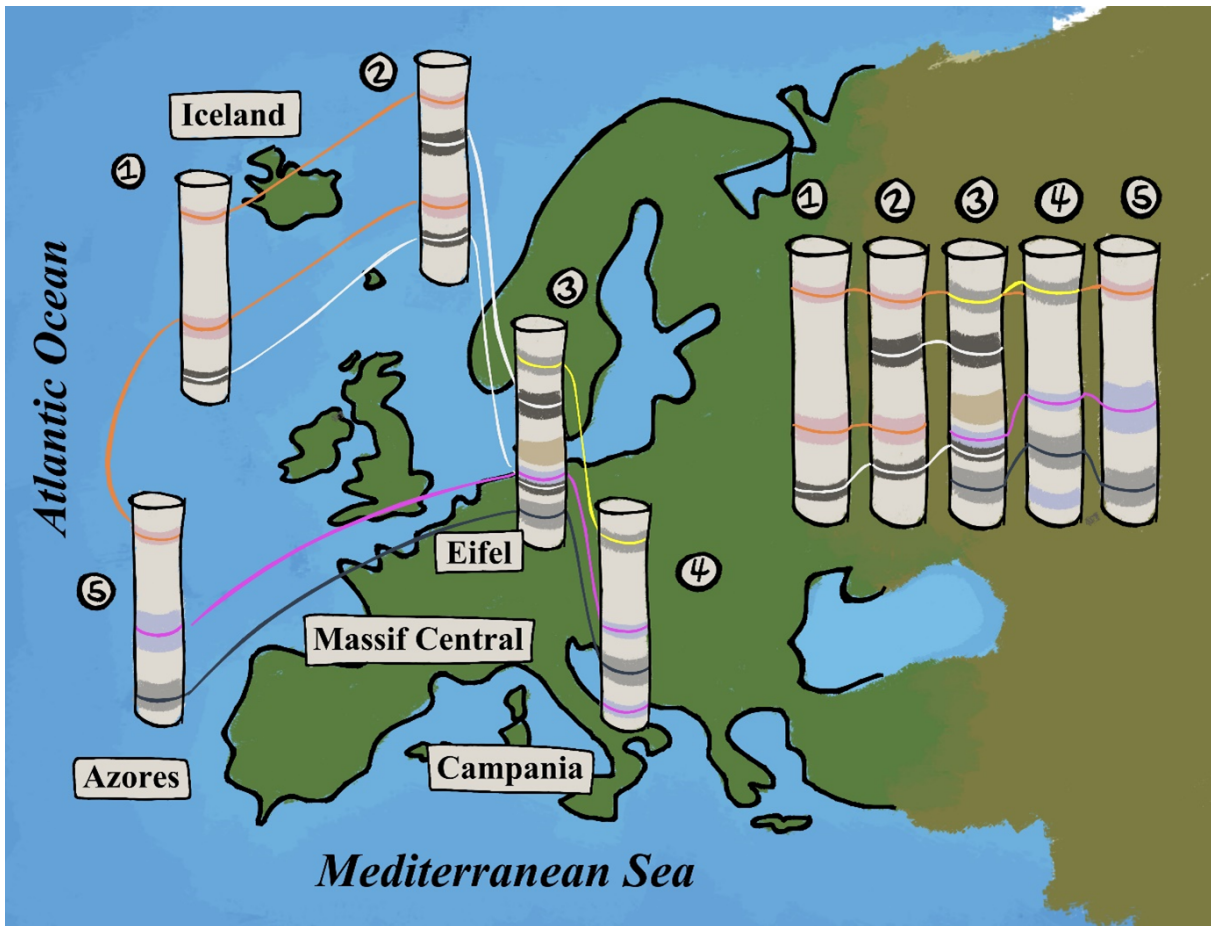


Figure 2.4: Schematic showing how hypothetical tephra layers across the European continent may be correlated together if they share the same geochemically distinct tephra layer (each tephra isochron is represented as a different coloured section within the cores).

Davies 2014). In a similar sense, the basic law of superposition suggests that a layer of tephra in a sedimentary sequence reflects the time at which it was deposited. All sediment below the volcanic layer is older and all sediment above is younger. There are cases of post-depositional reworking, such as bioturbation (Beierle and Bond 2002), that may affect its position in the sedimentary sequence to a variable degree (Abbott, Austin, and Davies 2014; Lowe 2011). In the absence of bioturbation in varved lake sediments, tephra remains concentrated within the depth it was originally deposited in. If a specific tephra layer is found across multiple sites, the associated sections of those sedimentary sequences can be dated to the age of the common tephra layer (Figure 2.4). Lastly, individual tephra layers are identified by their unique geochemical compositions. Every eruption produces tephra with a geochemical “fingerprint” unique to the plutonic and volcanic conditions under which it formed (Lowe 2011).

The geochemistry of tephra closely approximates the original magma composition and eruptive conditions from which it originated (Gill and Fitton 2010). Geochemical analysis of tephra is divided into stages depending on the detail needed to differentiate between distinct tephra

Table 2.3: Common methods of directly radiometrically dating tephra crystals or indirectly dating the layer in which the tephra lies. Some rows are coloured simply to differentiate between multiple methodologies in the table. Adapted from Encyclopedia of geoarchaeology (Lane and Woodward 2022).

Dating Methodology		
Direct	Argon	Radiometric decay of ^{40}K to ^{40}Ar to ^{39}Ar in K-rich crystals.
	Fission track	Measure zircon crystals and U-rich glasses. Age limit depends on U-content usually 50 ka BP.
Indirect	Radiocarbon	Radiometric decay of ^{14}C in organic material stratigraphically near or within a tephra deposit. Age limit less than 60 ka.
	Annual layers	Counting seasonally formed annual layers in ice or lake varves.
	Age modelling	Statistically combined age estimates from multiple dating methods, sites, or samples in a sedimentary sequence.

Table 2.4: Common methods of directly radiometrically dating tephra crystals or indirectly dating the layer in which the tephra lies. Some rows are coloured simply to differentiate between multiple methodologies in the table. Adapted from Encyclopedia of geoarchaeology (Lane and Woodward 2022).

layers. In distal environments, the microscopic glass shards are geochemically analysed, opposed to measuring larger minerals in proximal deposits (Lowe 2011). Major element analysis of common metal oxides can distinguish between silica-rich rhyolitic magmas, iron-rich basaltic magmas, and other magmas, as categorized by Bas et al. 1992. Minor and trace element analysis can help further distinguish between geochemically similar tephra layers, or between different eruptive events that may coexist within a single tephra layer. Tephra layers can either be classified as heterogenous or homogeneous depending on the geochemical similarity between individual glass shards in the layer. Heterogeneous layers, which often occur in the case ice-rafted tephra deposits (e.g. Abbott, Austin, and Davies 2014), contain volcanic shards of varying geochemical compositions, and therefore cannot be linked to a single eruptive event (Lowe 2011; Abbott and Davies 2012). Homogeneous layers contain volcanic shards of one geochemical composition and can therefore be linked to a specific eruptive event or source, if known. When the same homogenous tephra layer is found in multiple sedimentary sequences, it may also be used as a chronological marker or isochron (Figure 4; Lowe 2011). Isochrons form the cornerstone of tephrochronology, serving as the fundamental basis that connects palaeoclimate records together in time (Lowe 2011).

2.3.3 Dating tephra layers

The scope of this study focuses on tying tephra to the Bispingen pollen sequence, but dating layers using various tephrochronological methods is especially useful within other paleoenvironmental and even archaeological contexts (Table 2.4). If the stratigraphic position and the geochemical fingerprint of an isochron are known, then its age can be transferred to any other sedimentary sequence that shares a geochemically identical volcanic layer (Lowe 2011; Pyne-

O'Donnell 2011). Tephrochronology is therefore a robust and independent dating method with no maximum age limit, unlike radiometric dating. Tephrochronology relies on dating the individual shard or crystal itself by measuring the radioactive decay of Argon isotopes, and Uranium isotopes in sediments older than 50 ka BP (Lowe 2011; Lane et al. 2014; Lane and Woodward 2022). It is also possible to date the sediment in which the tephra layer lies by measuring the radioactive decay of Carbon-14 isotopes in organic material or by counting annual layers, e.g. lake varves (Lane and Woodward 2022). Indirect methods are commonly used in archaeological studies to identify major eruptions or constrain climate events that may have influenced human history (Lane et al. 2014).

2.4 Central European Holocene Chronostratigraphy

Cryptotephra, nearly always comprised of microscopic glass shards, is often transported great distances from its volcanic source (Lowe 2011; Jones et al. 2018). In recent decades, scientific focus has shifted towards using these non-visible cryptotephra to link sedimentary sequences from distal eruptions during the Holocene and Late Quaternary (e.g. Brauer et al. 2000; Lane et al. 2011b; Lane et al. 2015; Jones et al. 2018; Albert et al. 2024). Dugmore (1989) pioneered one of the first cryptotephra discoveries by uncovering traces of Icelandic eruptions in Scottish lake and peat sediments. This marked the first time that volcanic deposits from Iceland were discovered in Britain, more than a century after Mohn (1878) first mapped the spatial extent of volcanic ash beyond Iceland's border (Thorarinsson 1981b). The tephra deposit, traced to the Holocene Hekla 4 eruption in Iceland (c. 4 kyr BP; Dugmore 1989), has subsequently been found in many Scandinavian sequences, too (e.g. Zillen, Wastegård, and Snowball 2002). Nearly a decade after the pioneering discovery of an Icelandic ash layer in Britain, Lowe and Turney 1997 made cryptotephra research more accessible by adapting pollen extraction techniques to isolate the density of micro-tephra glass.

As Holocene cryptotephra studies emerge as invaluable tools for reconstructing the rates abrupt climate change, there is particular focus on regions with complex geological histories, such as Germany. Widespread Icelandic tephra layers like the Vedde Ash (c. 12.1 ka BP) and Askja (c. 10.8 ka BP) layers have been found in Meerfelder Maar in Southern Germany, Lake Hamelsee in Northern Germany, and Lake Soppense in Switzerland (Jones et al. 2018; Lane et al. 2011b; Lane et al. 2015). The discovery of Icelandic tephra in European lakes offers an opportunity to link sediment sequences across continents and large bodies of water (e.g. North Sea). Similarly, the widespread Laacher See Tephra layer (c. 13,000 years BP), a phonolite

deposit traced to Eifel, Germany, is notably visible without a microscope in all three lake sediment records and found in more than 400 other central European sites (Wörner and Schmincke, 1984; Riede et al. 2011, Jones et al. 2018, Lane et al. 2011b; Lane et al. 2015). Lake Hamsee and Meerfelder Maar, both in Germany, also preserve the Ulmener Maar Tephra, traced to Eifel Volcanic Field (11 ka BP; Brauer et al. 1999, Jones et al. 2018). The widespread Laacher See Tephra is used for correlating sequences on a continental and even intercontinental scale, while the Ulmener Maar Tephra is used for correlating between Maar lake sequences on a far more regional scale within Germany (Brauer et al. 2000). Interconnected tephra records help spatially resolve the timing and rate of recent climate responses, especially regarding the rapid Younger Dryas-Holocene transition. There is considerable strength in applying cryptotephra analysis on older varved lake records in Northern Europe to resolve similar spatial and temporal uncertainties during the Last Interglacial.

2.5 Comparable Tephra Archives

This section of Chapter 2 highlights known tephra layers that may serve as tie points to potential tephra layers in the Bispingen Palaeolake record. It covers volcanic activity in Europe between 70 to 130 ka, extending through the entirety of MIS 5. Considering volcanic activity over a period much longer than substage MIS 5e (roughly synonymous with the Last Interglacial) accounts for highly active volcanic centres over recent geologic history that have been discovered other substages, but have yet to be detected in sequences from substage 5e. Although tephra layers within this section are organized by their volcanic origin, the potential to correlate these archives with the Bispingen Palaeolake record holds more importance within the context of this chronostratigraphic study than their particular geographic origin.

2.5.1 Nordic tephras

While the number of recorded Icelandic eruptions during periods of deglaciation periods is far greater compared to other climatic phases, seemingly attributed to ice unloading and mantle decompression, there are still several widespread ash layers during the Last Interglacial that hint to at least several large eruptions (Aubry et al. 2022). So far, the most comprehensive collection of European tephra records during the Last Interglacial comes from a series of marine sequences in Iceland, Norwegian, and Greenland Seas (Sejrup et al. 1989; Sjøholm, Sejrup, and Furnes 1991; Fronval et al. 1998; Wastegård and Rasmussen 2001; Brendryen, Haflidason, and Sejrup 2010; Abbott et al. 2011; Abbott et al. 2013; Abbott, Austin, and Davies 2014; Davies

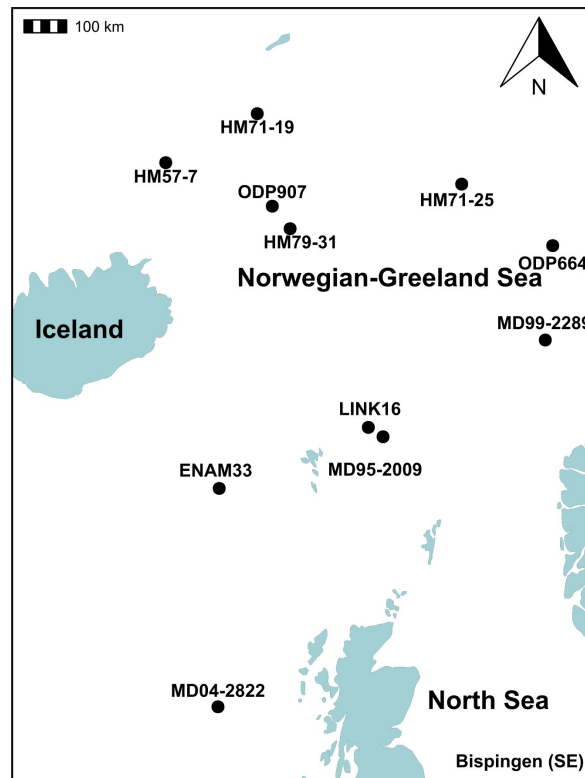


Figure 2.5: Marine cores studied in Table 2.5. Iceland is located on the left of the map, and small volcanic island Jan Mayen can be found at the very top of the map. Bispingen and Northern Europe lie outside the geographic bounds of this map but are generally located in the far southeast direction.

et al. 2014). Table 2.5 highlights most of the Icelandic cryptotephra isochrons that have been identified and linked between multiple Arctic marine cores.

Table 2.5: Summary of Icelandic tephra deposits. Leftmost column lists previously identified tephra horizons. Second column provides the associated MIS 5 interval of each tephra layer. Third column provides the estimated age of each tephra layer in ka BP. All eruptions are from Iceland, and their rock suite affinities are specified alongside the major composition of the deposit, where applicable. References [1] Abbott, Austin, and Davies 2014 [2] Davies et al. 2014 [3] Wastegård and Rasmussen 2001 [4] Sjøholm, Sejrup, and Furnes 1991 [5] Fronval et al. 1998 [6] Sejrup et al. 1989 [7] Brendryen, Hafidason, and Sejrup 2010 [8] Abbott et al. 2013 [9] Abbott et al. 2011. The highlighted blue tephra layers are isochronous layers that are geochemically linked to the same eruption.

Name	Time	Age	Composition	Cores	Location	Volcanic origin	Reference
MD04-2822 2359-66 cm	5a	75.3	Rhyolitic (tholeiitic)	MD04-2822	Rockall Trough	Icelandic Rift Zone	8,9
5a-Top/BAS-I	5a.21	76	Basaltic (tholeiitic)	MD95-2009	SE Norwegian Sea	Grimsvöth	3
5a-DO21/BAS I-III	5a.21	78.5 - 80.1	Basaltic (tholeiitic)	MD99-2289	Norwegian Sea	Grimsvöth	1,3,7
MD04-2822 2385-86 cm	5a	79.6 ± 2.0	Rhyolitic (trans. alkali)	MD04-2822	Rockall Trough	Öraefajökull	8
5a-Low/Bas-I	5a	83	Basaltic (tholeiitic)	MD95-2009	SE Norwegian Sea	?	3
MD04-2822 2424-25 cm	5c.22	91.3 ± 2.4	Rhyolitic (trans. alkali)	MD04-2822	Rockall Trough	Öraefajökull	8
5b-DO23s/BAS-I	5b.23	98.8	Basaltic (tholeiitic)	MD99-2289	Norwegian Sea	Grimsvöth	7
5c-DO23i/BAS-I	5c.23	103.2	Basaltic (tholeiitic)	MD99-2289	Norwegian Sea	Grimsvöth	7
5c-Mid/BAS-I	5c	104	Basaltic (tholeiitic)	MD95-2009	SE Norwegian Sea	Grimsvöth	3
5c-DO24s/BAS-I	5c.24	106.5	Basaltic (tholeiitic)	MD99-2289	Norwegian Sea	Grimsvöth	7
5d-DO25i/RHY-I	5d.25	112.5	Rhyolitic (trans. alkali)	MD99-2289	Norwegian Sea	?	7
5d-Low/RHY-I-III	5d		Rhyolitic (trans. alkali)	ENAM33	NE Atlantic	?	3
MD04-2822 2490-91 cm	5d	116.4 ± 0.7	Rhyolitic (trans. alkali)	MD04-2822	Rockall Trough	Öraefajökull	8
5d-DO26s/TRACHY-I	5d	116.7	Trachybasalt	MD99-2289	Norwegian Sea	Jan Mayen	7
Ash Zone?	5d	111.5	Basaltic (tholeiitic)	HM57-7, HM71-19, HM79-31, HM71-25, ODP664	Norwegian Sea, Iceland Sea	Grimsvoth, Askja, or Kverkfjoll	4,5
5e-Top/RHY	5e		Rhyolitic	ENAM33	NE Atlantic	Eastern Volcanic Zone	1,2,3
5e-Top/BAS	5e		Basaltic	ENAM33	NE Atlantic	Eastern Volcanic Zone	1,2,3
MD99-2253 1798-99 cm	5e	122	Basaltic (tholeiitic)	MD99-2289	Norwegian Sea	?	2
5e-Eem/RHY-I	5e	121.8	Basaltic (tholeiitic)	MD99-2289	Norwegian Sea	?	7
5e-Mid/RHY	5e	122-124	Rhyolitic (tholeiitic)	ENAM33, HM57-7, HM71-19, HM79-31, ODP644, ODP907	NE Atlantic, Norwegian Sea, Nordic Seas, Iceland Sea	?	1,2,3
5e-Eem/TAB-I	5e	124.4	Basaltic (trans. alkali)	MD99-2289	Norwegian Sea	Katla	1,2,4,7
5e-Low/BAS-IV	5e	127	Basaltic (tholeiitic)	ENAM33, MD95-2009	NE Atlantic SE Norwegian Sea	Grimsvöth - EVZ	1,2,3
Ash Zones	5e	129.5	Rhyolitic (tholeiitic)	H57-7, HM71-19, HM31	Norwegian Sea, Iceland Sea	Grimsvoth, Askja, or Kverkfjoll	4,5

Most of the Icelandic tephra layers are individual records, each only identified so far in one marine core (Table 2.5). However, a few notable layers have been correlated between multiple cores. There are two widespread tholeiitic basaltic layers associated with Grimsvöth volcanic zone, one during MIS 5a and an earlier one from MIS 5c. The latter isochronous layer, dated between 106.5 ka (Brendryen, Hafliðason, and Sejrup 2010) and 104 ka (Wastegård and Rasmussen 2001), is also found in a core from the Southeast Norwegian Sea (ENAM33; Wastegård and Rasmussen 2001). The 2 ka time difference between cores may be attributed to a minor difference in transport time for ash to reach core ENAM33, since this site is further from Grimsvöth, in the Southeast Norwegian Sea. There are also two widespread rhyolitic layers. The first rhyolitic layer, of transitional alkali affinity, was found in both the Norwegian Sea (Brendryen, Hafliðason, and Sejrup 2010) and the North Atlantic (Wastegård and Rasmussen 2001). While the origin of the tephra is unknown, the layer has an age of about 112.5 ka during MIS 5a (Brendryen, Hafliðason, and Sejrup 2010). The final, and most widespread, tholeiitic layer is found in seven cores, covering the Northeast Atlantic, Norwegian, Nordic, and Iceland Seas (Sjøholm, Sejrup, and Furnes 1991; Fronval et al. 1998, Wastegård and Rasmussen 2001; Abbott, Austin, and Davies 2014). Rhyolitic deposits can travel further than basaltic deposits because they are released from very explosive eruptions that produce large amounts of ash and pyroclastic material; in some exceptions, however, explosive phreatomagmatic eruptions happen when basaltic magma interacts with seawater (Gill and Fitton 2010). Accounting for all of MIS 5e, there are eight known tephra layers. As Icelandic ash layers have previously been found in other central European lakes (e.g. Poland [Kinder et al. 2020] and Romania [Kearney et al. 2024]), finding an Icelandic tephra layers in the Bispingen Palaeolake sequence may help correlate the floating Eemian pollen record to the anchored North Atlantic marine record.

2.5.2 Eifel tephtras

As Icelandic volcanos are generally the most active, or at least the most recorded, it is likely that cryptotephra in Bispingen Palaeolake may originate from this area. However, finding continental tephra layers in the Bispingen Palaeolake sequence would be especially useful in creating a tephra framework between Northern and Southern Europe. If they are underpinned by a shared tephra layer from the same eruption, there is a possibility to directly link the floating terrestrial sequences that comprise current understanding of Last Interglacial timing.

The West Eifel Volcanic Field is the closest major volcanic source to Bispingen Palaeolake, so the explosive phreatomagmatic eruptions from this region have potential to be found in the

Table 2.6: Tephtras traced to Eifel Volcanic Zone, Germany. References [1] Sirocko et al. 2005 [2] Bogaard and Schmincke 1990 [3] Pouclet, Juvigné, and Pirson 2008 [4] Gewalt and Juvigné 1986 [5] Sirocko et al. 2016 [6] Zöller and Blanchard 2009 [7] Leyk and Lippolt 1999 [8] Woda, Mangini, and Wagner 2001 [9] Frechen and Lippolt 1965 [10] Meyer 1994 [11] Preusser, Rufer, and Schreurs 2011).

Name	Age (ka)	Ref.
Rocourt Tephra	74-90.3	3
Pulvermaar Tephra	75	3,5
Mosenberg Tephra	~80	6,7,8,11
Lummerfeld	90 ± 40	9
Mauerley	100 ± 40	9
Veitskopf	110 ± 40	10
Remochamps Tephra	106 ± 6.0	4
Dumpelmaar Tephra	116 ± 16	1,2

lake sediment record. The Eifel volcanic record identifies six known tephra layers in MIS 5, including the Last Interglacial (Table 2.6). The oldest layer lies slightly outside of MIS 5 in the preceding glacial period at 136 ka and originates from Jungferwiher, Germany (Förster et al. 2010). Following this, the Dumpelmaar tephra is attributed to the eastern region of Eifel, France, and $^{40}\text{Ar}/^{39}\text{Ar}$ dating of its crystals placed this layer at 116 ± 16 ka until the age was tuned in a subsequent study to 105 ka (Sirocko et al. 2005). Found in Belgian cave deposits, Remochamps tephra has a rhyolitic composition with tholeiitic affinity and $^{230}\text{Th}/^{234}\text{U}$ dated to 106 ± 6.0 ka (Gewelt and Juvigné 1986). The most widespread tephra layer, Rocourt Tephra, occurs in the Early Weischelian between 90.3 and 74 ka (Pouclet, Juvigné, and Pirson 2008). While the Rocourt tephra age range is considerably larger, it was constrained from a previous estimate between 106 and 51 ka (Juvigné 1985; Gewalt and Juvigné 1986) by thermoluminescence dating of limestone clasts at the base of its intermixed soil-tephra layer (Pirson et al. 2006).

2.5.3 Massif Central tephtras

There are few cryptotephra deposits associated with Massif Central, so the majority of information about volcanic activity in this region comes from proximal volcanic debris outlines in Table 2.7. The Mosenberg Tephra is a regionally widespread tephra layer found in many sites around Germany. The crystals in the tephra formation itself were $^{40}\text{Ar}/^{39}\text{Ar}$ dated in several studies (e.g. Zöller and Blanchard 2009) to c. 80 ka BP. Lummerfeld and Maurley Tephtras from the Laacher See region are directly dated by K/Ar methods but the very large uncertainties (40 ka) may be associated with the time in which this study was conducted many decades ago (Frechen and Lippolt., 1965). Dumpelmaar Tephra is the only tephra layer with an age within MIS 5e

Table 2.7: Tephra deposits associated with Massif Central Volcanism, France.

MIS 5	Age	Location	Reference
5a	72 ± 7.5	Aubiere (Cler111)	Pilleyre et al. (1992)
5a	72 ± 12	Moula-Guercy - distal tephra	Sanzelle et al. 2000
5a	74 ± 6	Eguals, from Puy de Jumes? (CP 62)#	Gue´rin (1983); Raynal et al. 1984
5a	75 ± 10	Abuiere (cler 111)	Goe´r de Herve et al. 1993
5a	77 ± 9	Fond de Jaude (Cler 46)	Pilleyre et al. (1992)
5a	77.05 ± 9.90	Ray-Pic maar-near sausses on D 215 (VV 8003)	Gue´rin (1983); Pastre, Debard, and Chennaoui (1994)
5a	82.35 ± 4.90	Plateau St Jaques (CP 102)	Gue´rin (1983); Goe´r de Herve et al. 1993
5a	82.40 ± 4.4	Puy de Grave Noire (p. 201)	Brousse et al. 1990
5a	83.05 ± 9.2	La Sapede maar-NNE of freyssenat (VV 8006)	Gue´rin (1983); Pastre, Debard, and Chennaoui (1994)
5b	88 ± 10	Fond de Jaude (Cler 46)	Pilleyre et al. (1992)
5c	90.35 ± 6.2	lava from Bois de Chanat (CP 115)	Gue´rin (1983)
5c	94 ± 14	Pyroclastics du Bechet	Raynal et al. 1984
5d	113 ± 13	Puy de la Godivelle (MD 69) lac D'en Haut (1 Tb)	Gue´rin (1983)
5e	126 ± 15	Fond de Jaude (Cler 51)	Pilleyre et al. (1992)
5e	129.0 ± 6.5	Loubanere-west of Espinchal (MD 04)	Gue´rin (1983)

(Sirocko et al. 2005; Bogaard and Schmincke 1990).

2.5.4 Other tephtras

Lake Monticchio records numerous Italian eruptions throughout the Last Interglacial and is an excellent example of the types of Southern European tephra archives that can be found in annually laminated sediments (Table 2.8). Regardless of the volcanic province they may originate from, all tephra layers from Italy carry a similar, but unique, trachytic signature (Santacroce et al. 2008; Wulf et al. 2012). Beyond Italy, some of these trachytic layers have been found in the wider Mediterranean, including the Tyrrhenian and Ionian Seas (Giaccio, Nomade, Wulf, et al. 2012; Wulf et al. 2012). Because westerly winds are much weaker around the Alps, widespread Italian tephra layers are rarely found in Northern Europe (Sturman and Wanner, 2001). However, it is not impossible to find Mediterranean tephra in other parts of the continent. For example, both Italian and Greek tephra glass have been found in lake Ohrid, Macedonia (Vogel et al. 2010), while both Icelandic and Italian tephra glass have been found in Slovenia (Lane et al. 2011a). Even tephra layers from the Azores can be found across Europe. In Diss Mere, bordering the North Sea in Southeast Britain, eight tephra layers were found from Iceland in addition to a notable cryptotephra layer originating from the Azores (Walsh, Blockley, and Milner 2021). Several active volcanic zones in Italy and the Azores offer an opportunity to correlate the Bispin-gen Palaeolake sequence to Southern European tephra archives, and subsequently with the larger marine record.

Table 2.8: List of all known volcanic eruptions from Italy during MIS 5. The blue highlighted section consists of different tephra deposits all associated with a singular eruption from c. 106 ka. The green highlighted section consists of different tephra deposits all associated from a singular eruption from c. 107 ka. Both widespread tephra layers have only been found near or in the Mediterranean Sea. The majority of Italian tephra deposits from MIS 5, especially during MIS 5e, are recorded from the varved sediments in Lake Monticchio. For more detailed information on Italian eruptions and tephra deposits in Southern Europe from this lake see [1] Wulf et al. 2012. Other References [2] Giaccio, Nomade, Wulf, et al. 2012 [3] Paterne, Guichard, Duplessy, et al. 2008 [4] Keller et al. 1978 [5] Vogel et al. 2010.

Name	Age	Composition	Location	Volcanic Origin	Ref.
TM-25	105.480 ± 5270	trachytic	Monticchio lake	Campanian Province	1
C-27		trachytic	Tyrrehenian Sea	Roman/Campanian	3
POP3	106.2 ± 1.6 ka	trachytic	Sulmona basin	Campanian Province	2
CIL1		trachytic	Cilento coast	Campanian Province	2
X-5		trachytic	Ionian Sea	Campanian Province	4
TM-26	106.3 ± 5320	trachydacitic	Monticchio	Etna	1
TM-27	108.33 ± 5420	trachytic	Monticchio	Campanian Province	1
X-6	107 ± 2	trachytic	Ionian Sea	Campanian Province	4
C-31		trachytic	Thyrenniah Sea	Roman/Campania	3
CIL2		trachytic	Cilento coat	Campanian Province	2
OT0702-9		trachytic	Lake Ohrid	Campanian Province	5
TM-28	c. 110.5	trachytic	Monticchio	Campanian Province	1
TM-29	c. 112	basaltic - trachytic	Monticchio	Phlegrean Fields ?	1
TM-30	c. 114	trachytic	Monticchio	Phlegrean Fields ?	1
TM-31	c. 114.77 ± 5740	trachytic	Monticchio	Phlegrean Fields ?	1
TM-32	c. 115.25 ± 5760	trachytic	Monticchio	Stromboli Island ?	1
TM-33-1	c. 116	trachytic	Monticchio	Ischia Island	1
TM-33-2	c. 118.2	trachytic	Monticchio	Ischia Island	1
TM-34	118.810 ± 5940	trachytic	Monticchio	Salina Island ?	1
TM-35	c. 121	trachytic	Monticchio	Campanian Province	1
TM-36	c. 123.030 ± 6150	trachytic	Monticchio	Sabatina Volcanic District	1
TM-37	c. 124.3	trachytic	Monticchio	Ischia Island	1
TM-38	125.55 ± 6280	trachytic	Monticchio	Campanian Province	1
TM-39	130.53 ± 6530	trachytic	Monticchio	Campanian Province	1
TM-40	130.86 ± 6540	trachytic	Monticchio	Ischia Island	1
TM-41	131.020 ± 6550	trachytic	Monticchio	Campanian Province	1
TM-42	132.11 ± 6610	trachytic	Monticchio	Ischia Island	1

2.6 Summary

Knowledge of Last Interglacial climate in Northwest Europe is largely based on region-specific pollen zones in the Netherlands and Germany that are correlated together on the basis of their common forest taxa successions. While the pollen zones are useful in estimating the duration of the Last Interglacial, they are floating archives that cannot be radiocarbon dated, and therefore cannot provide absolute ages within the geologic record. In recent decades, there have been many conflicting estimates of Last Interglacial length, with a recent study of the annually resolved Bispingen Palaeolake sequence suggesting it lasted about 4000 years longer than the original Eemian sediments from Bispingen (Müller 1974). Longer-lasting warm Interglacial conditions in Northern Europe has wider implications for the diachroneity of climate responses in Europe, as it suggests that warming was on par with that of Southern Europe. Also in recent decades, far travelling volcanic ash called cryptotephra has been an important tool for dating and correlating sediments sequences. The fundamental principle behind tephrostratigraphy suggests that when geochemically similar cryptotephra shards are found in multiple cores, the depths in which the tephra was found can be linked together between sites. If tephra is found in the Bispingen record, it has the potential to be geochemically linked to one of the known Last Interglacial records in the North Atlantic, thus connected the floating Bispingen pollen zones to the wider anchored marine sediments.

CHAPTER 3

STUDY SITE

This chapter provides further detail on the geological context of Lower Saxony followed by a summary of the previous studies of Bispingen Palaeolake and detailed information of the composite sediment sequence used in this study.

3.1 Geographical Information

The former Bispingen Palaeolake (53°050N 10°000E) lies south of the Bispingen municipality, slightly northeast in the Lower Saxony region of Northern Germany (Figure 3.1). The palaeolake accumulated in the meltwater channel formed during the Saalian glacial phase, specifically during the first ice advance known as the Drenthe stage (Cartelle et al. 2021). Today, the Lühe river flows through the palaeolake site into the Elbe River, whose tidal influence reaches about 150 km inland (Meschede and Warr 2019; Hein et al. 2021). The Elbe River Estuary drains into the German Bight, a shallow (<50 km deep) section of the southeastern North Sea and creates a slight stratification between freshwater that diffuses with sea water within the upper tidal-influenced part of the river (Schrum 1997, Hein et al. 2021).

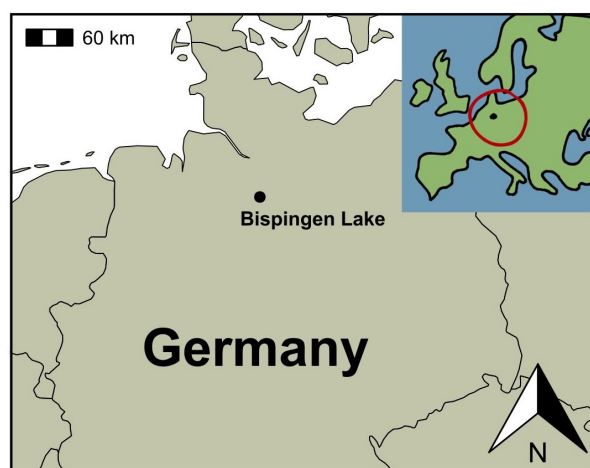


Figure 3.1: Simple map of Bispingen Palaeolake in Northern Germany.

3.2 Last Interglacial Climate in Lower Saxony

Because Bispingen is located in Northern Germany, its climate is reflected in both regional trends of continental Northwestern Europe and marine influence from the North Sea. The climate of Northern Europe is significantly influenced by the North Atlantic, which plays a crucial role in shaping weather patterns and climatic conditions across the continent. Both sea surface temperatures and sea levels peaked during substage MIS 5e, which is palynologically associated with Last Interglacial terrestrial records (Shackleton et al. 2003). By the mid-Interglacial and climate optimum, sea surface temperatures in the North Atlantic increased about 0.6°C above the pre-industrial average (Dutton and Lambeck 2012). While sea levels were not globally uniform, they nonetheless averaged to about 5.5 to 9 meters higher than present levels, indicating that both the Antarctic and Greenland ice sheets were also smaller than present day (Dutton and Lambeck 2012). In comparison, sea levels during the other two mild stadials (MIS 5c and MIS 5a; see Table 2.1) were globally-averaged 20 m lower than present day (Dutton and Lambeck 2012). During the Last Interglacial, the North Sea experienced lower seasonal sea level extremes that were linked to shifts in atmospheric circulation and strengthened mid-latitude westerlies (Scusolini et al. 2023; Salonen et al. 2021).

Because more intense westerly winds brought warmer and wetter air masses to Northern Europe precipitation increased (Salonen et al. 2021; Helmens 2014). The humid environment in Lower Saxony facilitated the spread and growth dense forest, including mixed oak (*Quercum mixum*) and hazel (*Corylus*) (Helmens 2014, Lauterbach et al. 2024). Indicator fauna species records from Oerel Palaeolake north of Bispingen suggest that July summer temperatures in Lower Saxony reached 18°C in the *Carpinus* phase. After the climate optimum, Colpτερα fauna macrofossil species further indicated that the average temperature of the coldest and warmest months were nearly 3°C warmer than today (Helmens 2014). As a note, Although the Oerel record has been well-studied for pollen and macrofossils, it was not utilized in this study due to its incomplete nature, especially as it transitioned into more of a fen environment towards the Late Eemian (Behre and Plicht 1992; Behre, Hölzer, and Lemdahl 2005; Helmens 2014). While the Last Interglacial generally transitioned from peak warmth to cooler glacial conditions, there were some smaller oscillations in between. The Late Eemian Aridity Pulse (c. 118 ka) was a brief 428-year period marked by reduced humidity and the expansion of drier-climate grass species in Central and Northern Europe, as recorded in the pollen assemblages of Eifel Maar Lakes in Western Germany (Sirocko et al. 2005).

3.3 Geological history of Lower Saxony

By the end of the Tertiary period, the North Sea basin was characterized by shallow marine and deltatic sediments as sea level retreated from continental Europe (Zagwijn 1985, Liu and Galloway 1997). Over the following 2.6 million years that comprise the Quaternary period, there were several stages of landscape development in Lower Saxony. An 800 m long borehole sequence from the southern North Sea Basin containing the basal layers of shallow marine to deltatic sediments suggested periods of transgressions around 2.1 million years ago (Cameron et al. 1993; Long et al. 1988). Towards the Middle Pleistocene (2.0-0.2 Ma), there were three transgression events associated with three warm periods Tiglian Complex (2.1–1.7 Ma BP), Waalian Complex (1.3–0.95 Ma BP), and Cromerian Complex (c. 0.7–0.4 Ma BP) (Zagwijn 1979).

By the Upper Pleistocene (126-12 ka) there were three cold climate phases and two warm climate phases. In the oldest cold phase, glacial melting caused hydrostatic pressure beneath the Elesterian ice sheet and carved a system of several hundred kilometre deep valleys into the early Pleistocene sediments (Long et al. 1988; Laban 2000). In the following warm period called the Hostenian Interglacial, transgression reached nearly 160 km inland of the Elbe river, filling in some of the incised valleys from the preceding glacial period (Cameron et al. 1993). In fact, open-water foraminifera suggested that the Hamburg area had a water depth of 20-30 m at the start of the Holstenian Interglacial (Knudsen 1993). The Saalian ice sheet in the following glacial stage extended to parts of Northern Germany, including the area of Bispingen (Cameron et al. 1993; Laban 2000) .

3.3.1 Lower Saxony during the Last Interglacial and Weichselian glacial

During the Last Interglacial (MIS 5e), local sea levels rose nearly 100 m from the glacial low-stand, and the German coastline was very similar to present-day. The shoreline in Northwest Germany and Southwest Denmark initially ran parallel to the modern Wadden Sea, and marshy tidal flat deposits only reached an elevation of 7.5 m below current mean sea level (Cohen et al. 2022). Sea level rise was about 4 m per century in the 650 year period of Eemian Pollen zones IIIa and IIIb, and slowed in the following zones (Streif 2004). Sea level peaked during the climate optimum E5 (Cohen et al. 2022). After the interglacial maximum, sea levels dropped more than 35 m below present-day levels in the Southern North Sea during the Weichselian (MIS 4-2) cold stage, exceeding more than 100 m below present-day levels. The Fennoscandinavian ice sheet reached just north of Hamburg, therefore excluding the Bispingen area.

3.3.2 Lower Saxony during the Holocene

The majority of sediments that lie near the surface of the Lower Saxony region were deposited across several transgressive events throughout the Postglacial and Holocene periods. The periods of transgression can be divided into older Calais phases between 8000 and 3000 years ago and younger Dunkirk phases between 3000 and 500 years ago (Behre 2004). Although the rate of sea level rise slowed by 8000 BC, these periodic phases of transgression were still significant enough to deposit layers of marine clays and sands onto peat sediments (Cameron et al. 1993).

The interactions between the North Sea and the coast also affected areas further inland where lower parts of fluvial systems were still influenced by sea levels and storms (Hageman 1969; Behre 2004). Holocene coastal deposits are normally found within 10 - 20 km from the German shoreline, but extend nearly 100 km inland along the Elbe river estuary (Streif 2004). The raised areas of clay deposits along riverbanks formed natural levees and were covered with woodland until 800 BC when Iron-age Roman settlers began clearing trees. The earliest settlements were built along the Em river in the Netherlands and eventually abandoned by widespread flooding and subsequent clay deposition caused by a Dunkirk transgression event. Roman riverbank settlements in Germany were established later, and built on either the natural clay levees along rivers or built on the tops of artificial clay levees called *Wurts*, both kinds likewise abandoned by the middle ages due to floods in the 13th century (Haarnagel 1979, Behre 2004). The present-day ruins of these villages have nonetheless preserved numerous wood samples that are invaluable resources for reconstructing the river environment in Lower Saxony. (e.g. Behre and Menke 1969, Behre, Dörjes, and Irion 1985). In contrast to the heavily-wooded riverbanks before human occupation, palaeoecological analysis of pollen and wood macro-remains suggest that raised clay deposits slowly thinned into low-elevation treeless peat backswamps further away from fluvial sources (Behre 2004). The general sedimentary sequence of Lower Saxony during the Holocene alternated between marine clays overlying peats during transgressions and peats overlying marine clays during regressions (Baeteman and Gans 1993, Behre 2004, Streif 2004). Further inland, the Holocene sediment record was less affected by frequent transgression-regression cycles along the coastline, so sites near Bispingen (i.e. Figure 3.2) showed fewer alternating layers of peat and clays.

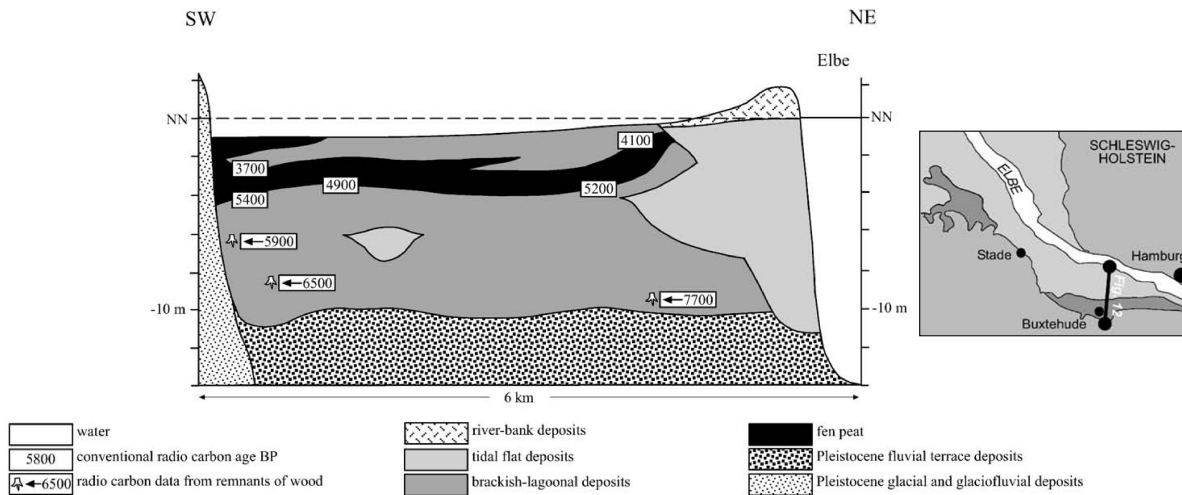


Figure 3.2: Cross-section of an inland Holocene sediment sequence that runs from the Elbe River to Buxtehude (From Streif 2004; Figure 13). The inset image in the bottom-right corner was taken from Figure 6 in Streif 2004 to show the position of the cross-section relative to the Elbe River in Lower Saxony, Northern Germany. Buxtehude is about 90 km southwest of the North Sea coastline, and relevant to this study, it is also about 50 km northwest of Bispingen Municipality.

3.4 Previous Work at Bispingen

The Bispingen Palaeolake was first discovered during a public works project between 1970 and 1971 that aimed to identify and analyse diatomite deposits for economic use in Lower Saxony (Benda and Brandes 1974). In the larger Lower Saxon region of Germany, the public works project found two interglacial deposits (one from the Holsteinian Interglacial [MIS 11] and one from the Eemian Interglacial [MIS 5e]) spread across several isolated basins, including Bispingen. (Benda and Brandes 1974). The Bispingen site (Figure 3.1) was identified about 1 km southwest of the Bispingen municipality, after several unsuccessful coring attempts to find diatomite layers north of the town (Benda and Brandes 1974). The same project took a series of smaller cores within the Bispingen site and found that the wedged diatomite layer had a volume around $150,000 \text{ m}^3$, with a maximum thickness of 10 km that thinned out northward (Benda and Brandes 1974). While the public works project in the early 1970s first discovered Bispingen as diatomite deposit, the full Last Interglacial sequence was not studied in detail until a few years later.

Müller (1974) provided a detailed analysis of the sediment and pollen records in one of the cores (KS 186/70) previously drilled in the public works project. This unprecedented dataset pioneered Last Interglacial research because the sediment sequence was not only continuous and the first of its kind in Northern Europe, but the pollen succession was very similar to other sites

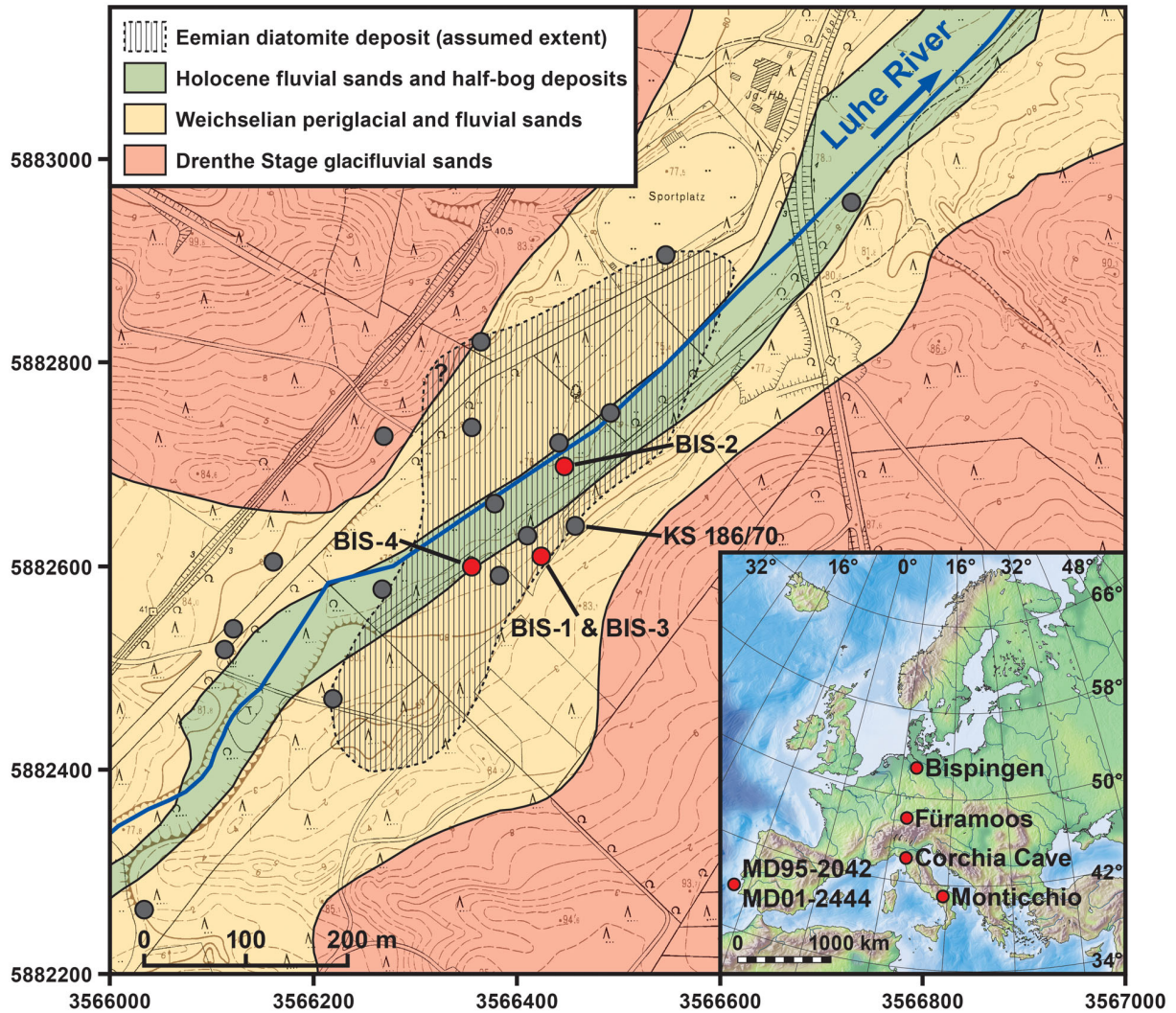


Figure 3.3: Topographical map of Bispingen Palaeolake sequence (zone 3 Cartesian Gauss-Kruger coordinates). Grey coordinate points represent the original sediment sequences. Red coordinate points represent the new sediment sequence cored in 2000. Inset map depicts the location of Bispingen in Northwest Europe relative to other Last Interglacial proxy records discussed in Lauterbach et al. 2024. Source: Lauterbach et al. 2024; Figure 1; data from Lower Saxony Soil Information System (NIBIS) map server (Lower Saxony State Office for Mining, Energy and Geology, Hanover, Germany).

Table 3.1: Columns (left to right) detail the depths, primary content, and lacustrine interpretation for each distinct sedimentary unit from BIS-2000 (Lauterbach et al. 2024).

Unit	Depth (cm)	Material	Interpretation
7	1606-1555	increased siliclastics + increased organics	silting of lakes
6	1697-1606	diatoms	lacustrine sedimentation returns
5b	1849-1697	diatom free + organics + siliclastics	ends of lacustrine sedimentation
5a	1886-1849	low siliclastics	
4	2129-1886	calcite free + diatoms	
3	2922-2129	calcites + diatoms + siliclastics	lacustrine sedimentation disrupted by sand deposition
2	3047-2922	increased diatoms + decreased siliclastics	distinctly varved
1	3068-3047	calcite + diatoms	start of lacustrine sedimentation

in the region (Table 2.2; Zagwijn 1961, Zagwijn 1983; Mamamkowa 1989; Müller 1974; Menke and Tynni 1984; Litt, Junge, and Böttger 1996). Because the Bispingen record is continuous, including portions of distinctively varved layers, it is used as a crucial tie-point between the common pollen successions (Table 2.2; Zagwijn 1961, Zagwijn 1983; Mamamkowa 1989; Müller 1974; Menke and Tynni 1984; Litt, Junge, and Böttger 1996). Although the original Bispingen sequence by Müller 1974 has served as a fundamental connector between other Eemian pollen sequences, the site was not studied again for many decades.

Bispingen was re-cored in December of 2000 and reanalysed for its sediment and palynological components, published in a recent paper by Lauterbach et al. (2024). This study obtained four parallel cores from the German palaeolake, and two of these cores, BIS-1 and BIS-3, were compiled into a continuous sedimentary sequence renamed as BIS-2000 (Figure 3.5). The composite core was divided into 7 distinct sedimentological units, with the majority of this study focused within the calcitic-diatomic sediments of Unit 3 and diatomic sediments of Unit 4 (Table 3.1). The varved facies occur in early stages of Bispingen Palaeolake development, but the record is disrupted by breaks in sedimentation, including a possible rapid sand deposit in Unit 3 (Table 3.1).

Lauterbach et al. (2024) used BIS-2000 to conduct palynological analysis on 128 x 1 cubic centimetre sediment samples at 10 cm resolution. Palynological data was incorporated into an updated floating chronology using varve analysis between 3047 and 2922 cm (the entire BIS-2000 sequence extends from 3068 to 1555 cm; Lauterbach et al. 2024). The varves themselves were made of alternating light-coloured calcite precipitated from CaCO_3 oversaturation in warm spring months (Brunskill 1969; Kelts and Hsü 1978; Lauterbach et al. 2024), and dark-coloured organics precipitated in late autumn. Some varve layers contained a third layer of dark diatomite that reflected increased nutrient availability in early spring (Bluszcz et al. 2008; Maier et al. 2018). Lauterbach et al. 2024 identified three types of varves in order of distinguishability: the first kind of varve was easily counted while the second kind of varve was not clear enough to

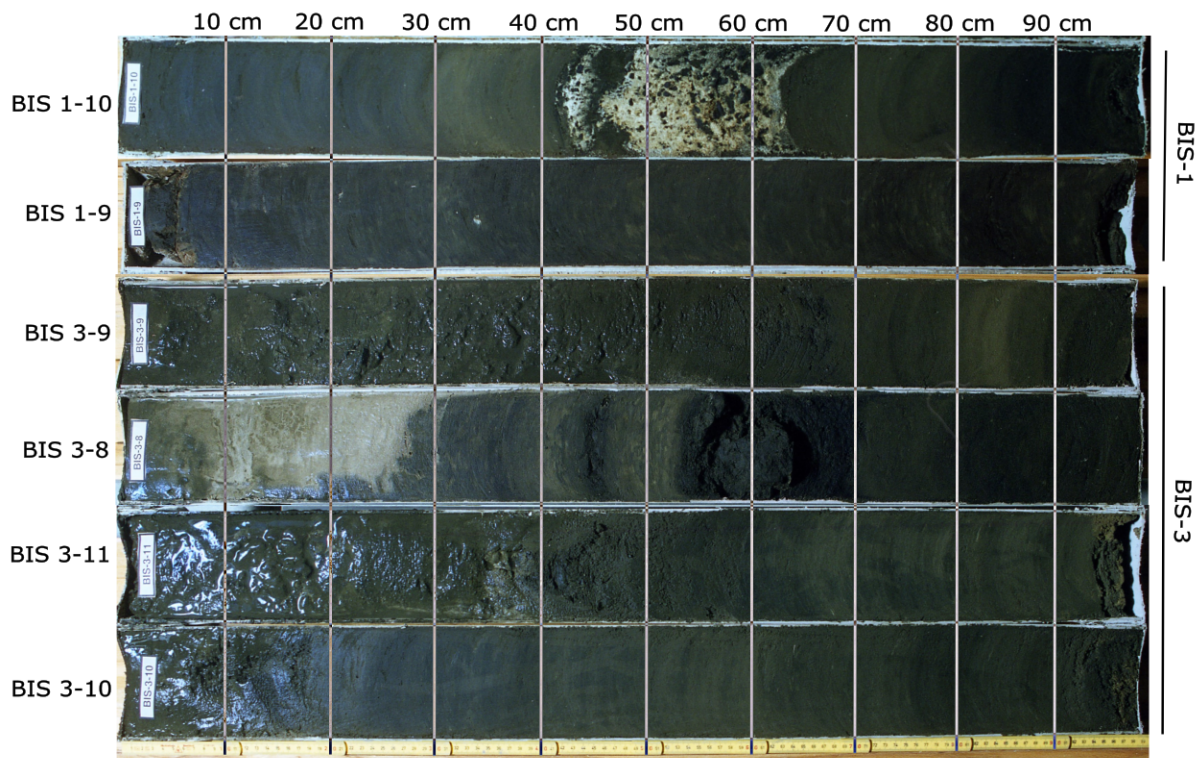


Figure 3.5: Images of the core sections used in this study, including sections 9 and 1 of core BIS-1 and sections 8-11 of core BIS-3. Lower sections of these cores are associated with the Early Weischelian and not within the Last Interglacial scope of this study. The entirety of the BIS-2000 sequence is a combination of cores BIS-1 and BIS-3. Source: Lauterbach, pers comms.

Table 3.2: Estimated length of each pollen zone from core KS 186/70 and BIS-2000. The rightmost column notes whether the varves were easy to count or whether they were estimated indirectly using the thickness of layers. References [1] PAZ from Zagwijn 1961 [2] PAZ from Selle 1962 [3] KS 186/70 core from Müller 1974 [4] BIS-2000 first from Lauterbach et al. 2024 and used in this study.

PAZ ¹	PAZ ²	Taxa	KS 186/70 ³	BIS-2000	
Saalian		NBP			top of core
E7	VI	Pinus	2000	1750	
E6b	Vb	Pinus-Picea-Abies			
E6a	V	Pinus-Picea-Carpinus	2000	2055	estimated from thickness and duration of KS 186/70 (Muller, 1974)
E5	IV	Carpinus	4000	7100	
E4b	IIIc	Tilia	705	1800	
E4a	IIIb	Corylus	1100	975	
E4a	IIIa	Quercetum mixtum-Corylus	450	405	direct counting annual layers
E3	IIb	Pinus-Quercetum mixtum	450	350	
E2	IIa	Pinus-Betula	200	365	
E1	I	Betula-Pinus	100	150	estimated from counting discontinuous annual layers
		Total	11000	<15000	

be directly counted and relied on interpolating from the average sediment thickness of a layer, and the third kind of varve was somewhat distinguishable. The variability of varve preservation was likewise observed in the original study from Müller (1974) who also employed interpolation techniques on the indistinguishable varve layers (Table 3.2; Zolitschka et al. 2015).

Comparing BIS-2000 to the original KS 186/90 finds that the estimated duration for the entire Last Interglacial period is 4000 years longer, extending the previous 11000-year estimate to just under 15,000 years (Figure 3.4; Müller 1974; Lauterbach et al. 2024). The estimated durations of the short pollen assemblage zones at the start of the Last Interglacial are roughly the same between both studies likely because the finely varved layers offer higher precision. The difference between estimates lie in the climate optimum in PAZ IVb and V. PAZ IVb is now estimated at 1800 years in length, over double its original length; and PAZ E5 is now estimated over 7000 years in length, also nearly double its original length Müller 1974; Lauterbach et al. 2024). The updated chronology from BIS-2000 implies that peak interglacial warmth persisted for roughly twice as long than originally thought. The new estimate of 15,000 years for the duration of the Eemian is very similar to Southern European estimates, resolving the diachroneity between a shorter warm period in Northern Europe found in several other studies (Shackleton et al. 2002, Tzedakis et al. 2018; McGuire, Waajen, and Barlow 2024). Despite the BIS-2000 sequence reevaluating the first estimate of Last Interglacial duration from the same study site, it is nonetheless still a floating chronology that cannot definitively suggest when the Interglacial actually began. Henceforth, this study revisits the same BIS-2000 sequence with a tepthrostratigraphic approach.

3.5 Summary

Early Pleistocene sediments infilled large glacial-incised valleys, and Last Interglacial sediments infilled smaller Saalian glacial basins. Over the recent few millennia, inland Lower Saxony indirectly experienced the effects of sea level rise and periodic transgression events from fluvial deposition of clays, forming a regional contrast between woodland forests on elevated clay deposits along riverbanks and treeless peat backswamps that were too far from rivers to receive any of the clay deposits. Bispingen Palaeolake was discovered in regional diatomite deposits, and first studied by Müller 1974, originally suggesting that the Last Interglacial lasted 11,000 years, marking the first estimate of Last Interglacial timing in Northwest Europe. The site was reinvestigated in a recently published paper by Lauterbach et al. 2024. The pollen succession was highly comparable to its original counterpart by Müller 1974, but suggested that the Last Interglacial actually lasted about 4000 years longer, or 15, 000 years in total. The composite sequence from this study, renamed BIS-2000, is hereafter reanalysed from a tephrostratigraphic perspective with the broader contextual goal of anchoring this floating chronology.

CHAPTER 4

METHODOLOGY

This chapter justifies the methods used for extracting and identifying cryptotephra in the BIS-2000 sequence. The methodology can be summarized in Figure 4.1.

4.1 Sampling Methods

Both 70 low-resolution samples (5 cm) and 29 cm high-resolution samples (1 cm) were taken and subsampled from the original BIS-2000 sequence reported in Lauterbach et al. (2024) at University of Potsdam, German Research Centre for Geosciences. All subsequent work, including cryptotephra extraction, as follows, took place at University of Leeds.

Samples were catalogued, dried, and weighed. Samples were generally processed in batches of 15, leaving room for approximately one blank to test for cross contamination. Splitting samples into batches was important for reducing cross contamination, time efficiency, and for recycling the heavy liquid discussed in the following section. The number of samples in each batch were usually determined by the maximum capacity of the centrifuge, aiming for a total of 16 sample tubes in each batch, including blanks (Table 4.1).

4.2 Cryptotephra extraction

The sections of the BIS-2000 used in this study were obtained from the poorly varved parts of the sequence (Figure 3.5). From sedimentological analysis of varved sections from the sequence,

Table 4.1: Batches refers to the samples that were processed in the same group (i.e. washed, centrifuges, density separated, counted, etc. at the same time).

Batch	Date of processing	Number of Samples	Number of Blanks
1	October 2023	16	0
2	January 2024	15	1
3	Feb/March 2024	15	1
4	April 2024	14	2
5	April 2024	10	2
A	May 2024	14	2
B	May 2024	15	1

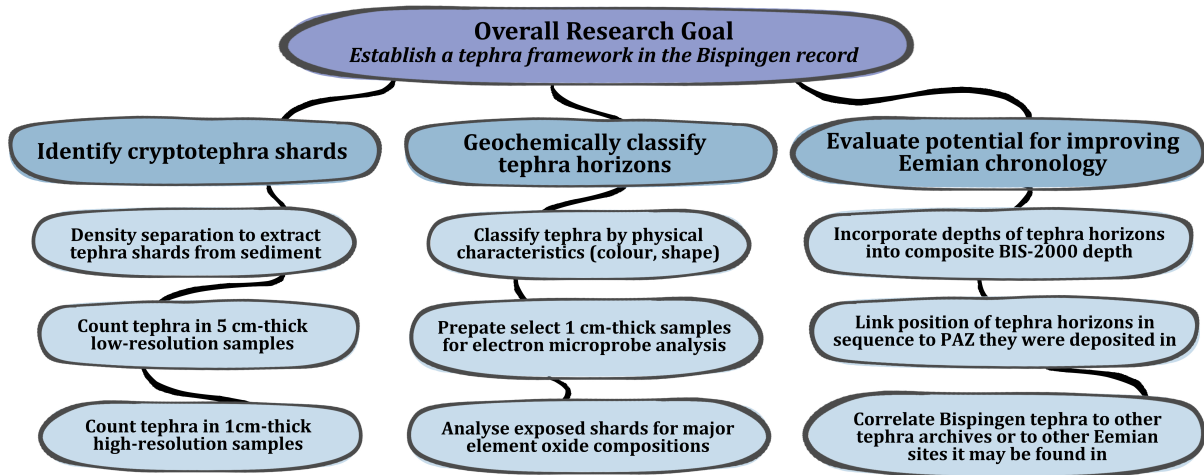


Figure 4.1: Workflow summarising the three main goals of this study (detailed further in Chapter 6) and specific methodologies for achieving these goals.

Lauterbach et al. (2024) identified no tephra horizons, which are usually identifiable at the visible level because of their unique colour and texture characteristics compared to the rest of a sequence (e.g. Wulf et al. 2012). To identify tephra shards that are not visible to the naked eye, they need to be extracted.

The cryptotephra analysis procedure follows a combination of sieving and density separation techniques from Blockley et al. (2005) that protect glass shards from becoming chemically altered or physically destroyed in the laboratory. Traditional chemical digestion techniques for extracting tephra glass shards (e.g. Hall and Pilcher 2002) use corrosive liquids which can chemically alter cryptotephra shards (Blockley et al. 2005; Cooper, Savov, and Swindles 2019). In studies that rely on the element analysis of only a few shards per sample, such as this one, even a slight change in shard geochemistry will have a strong influence over the correlation of tephra layers. Therefore, this study uses density separation (after Blockley et al. 2005) to ensure preservation of the unique geochemical signature of cryptotephra. Limiting geochemical alteration of tephra glass shards is vital as the geochemical fingerprint is ultimately used for correlating between other cryptotephra layers that hold the same geochemistry (Blockley et al. 2005).

Sediment samples were dried, weighed in 12 mL round-bottomed centrifuge tubes, then mixed with a 10 % HCl solution to dissolve carbonates. Each sample was wet sieved twice: first through a 125 μm nylon mesh and then 15 μm , saving the size fraction in-between, because most cryptotephra shard sizes lie well within this range (Hall and Hayward 2014). A lighter sodium polytungstate (SPT) solution of 1.95 g cm^{-3} was added to 15 μm to 125 μm size fraction to remove less dense material, such as the organic fraction. The mixture was centrifuged at 1800 rpm for 20 minutes with the break off, using a VWR Mega Star 1.6 centrifuge machine. After

disregarding the supernatant of this mixture, a higher SPT solution of 2.51 g cm^{-3} was added to the remaining $15 \text{ }\mu\text{m}$ to $125 \text{ }\mu\text{m}$ sediment. The supernatant, between 1.95 g cm^{-3} and 2.51 g cm^{-3} , was saved into 15-mL conical-base tubes, which were then topped with deionized water and centrifuged at 3000 rpm for 5 minutes. The lighter and denser fractions were retained for possible identification.

The next step involves both recycling the SPT solution while preserving the material in the centrifuge tube containing the glass fraction between 1.95 g cm^{-3} and 2.51 g cm^{-3} . Dissolving all SPT from the sample was especially important to prevent it from crystallizing on the microscope slide. Small $15 \text{ }\mu\text{m}$ sieve mesh squares were placed between two small glass cylinders. The contents of the centrifuge tube with the glass fraction were poured through one cylinder opening, passing through the $15 \text{ }\mu\text{m}$ sieve mesh that was secured in place by the second cylinder, so the glass fraction collected on the mesh and the SPT collected in a beaker underneath (Figure 4.2). Once enough deionized water was sieved through the sample to dissolve all remaining SPT, the sample was washed off the mesh back into its original 15-mL conical based centrifuge tube. The centrifuge tubes were once again topped with deionized water and centrifuged at 3000 rpm for 5 minutes. Conical-base centrifuge tubes were helpful at this stage, opposed to 12 mL round-base centrifuge tubes, because the amount of glass-fraction material in each sample was so small that a narrow bottom helped concentrate it into a smaller area that was easier to pick up with a pipette tip. In the mounting stage, the supernatant was discarded, and the glass fraction was placed onto glass slides using a 1-mL pipette. The slides were warmed directly on a hot plate, allowing the water to evaporate from the glass fraction, after which a cover slip with a few drops of warm Canada Basalm was placed over it. The remaining $<1.95 \text{ g cm}^{-3}$ and $>2.51 \text{ g cm}^{-3}$ fractions also were retained and checked for the presence of possible tephra shards that may have fallen outside of the standard density range of glass.

4.3 Microscopy and Shard Concentrations

Prior to geochemical analysis, tephra shards were first identified by their physical characteristics under the microscope. All slides were scanned between 20x and 40x magnification on a Leica DM2000 petrographic microscope, using cross-polarized light under which non-crystalline material, like glass, will not glow. The "glowing" represents light penetrating through minerals, and cryptotephra does not have this quality, unless chemically altered. The colour of a tephra shard is dependent on its composition, with clear or slightly-pink shards relating more to felsic and rhyolitic magmas and brown or slightly-yellow shards relating more to mafic and basaltic

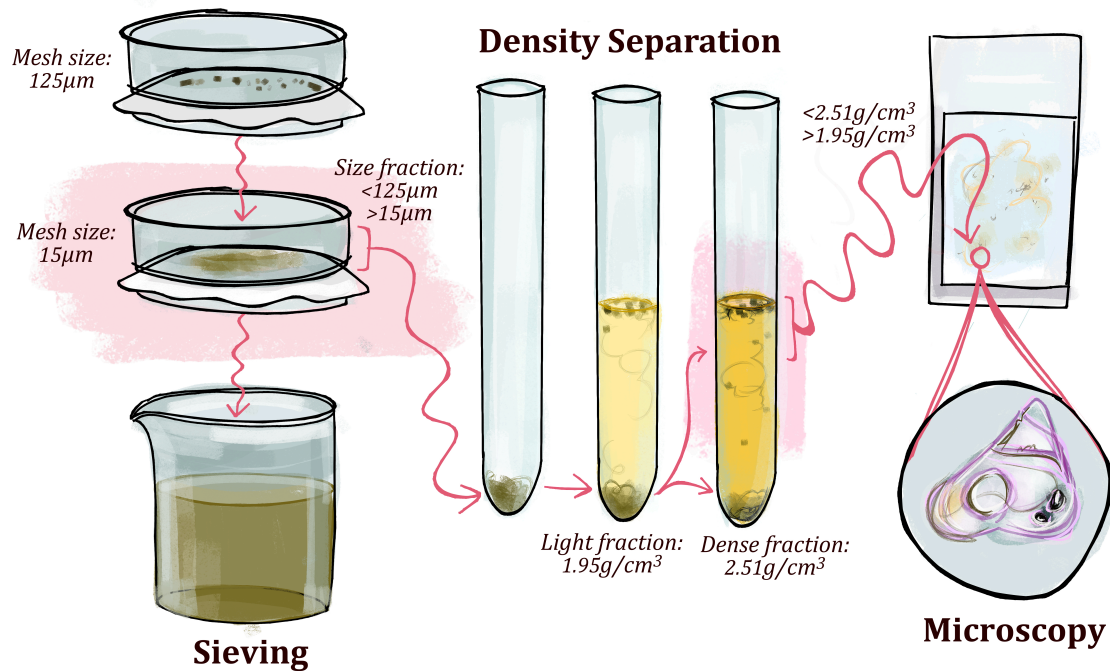


Figure 4.2: Illustration summarising the laboratory procedures for identifying tephra shards. Cryptotephra preparation can be divided into three main steps: wet sieving the sample (left), density separating the size fraction between $15\mu\text{m}$ and $125\mu\text{m}$ using a heavy-liquid sodium polytungstate solution (middle), mounting the dense fraction between 1.95 g cm^{-3} and 2.51 g cm^{-3} onto microscope slides (top-right). Extracted cryptotephra shards are then ready to be counted at either 20x or 40 magnification under a microscope (bottom-right).

magmas (Kvamme et al. 1989, Kristjánssdóttir et al. 2007; Lowe 2011).

All samples were plotted on graphs of shards per gram versus core depth using rioja package, also used for plotting alongside pollen data (Juggins 2024). As high tephra concentrations are the primary indicator of isochronous ash layers, major peaks in the low-resolution shard versus depth profile were further selected for 1 cm high-resolution analysis to pinpoint a specific depth over which the possible isochron was deposited (Davies 2015). The above steps for cryptotephra extraction and identification were repeated for 29 high-resolution 1 cm samples, instead mounted with a non-permanent glycerol medium to allow picking of individual shards for chemical analysis after counting how many were in each sample first.

4.4 Identifying Tephra Peaks

Identifying the precise depth of major tephra peaks is essential for determining the stratigraphic position of an isochronous ash layer (Davies 2015). Various visual characteristics of a shard concentration profile can indicate the locations of these significant tephra peaks within a sequence. The taphonomic processes that guide tephra deposition in lakes affect both shard concentration and the stratigraphic position of an isochron, which are visually represented in the shape of a shard concentration profile and the vertical variability of tephra peaks. Samples with high shard concentrations are generally defined as tephra peaks, but it is also relative to the shard concentration in nearby samples. Tephra peaks are easiest to identify in well-preserved airfall deposits because instantaneous ash fallout combined with minimal reworking produces a discrete peak with little shards in neighbouring samples (Figure 4.3, Panel A). However, even in instantaneous ash deposits bioturbation and other post depositional process will rework tephra and vertical redistribute it over a wider depth range (Davies 2015). An obvious tephra peak may still be present, but it will be accompanied by a gradual decrease in shard concentration. Evidence of reworking is usually seen upcore because it will account for both bioturbated tephra and tephra that is washed in later on, but it is possible for tephra to be vertically displaced down core below the peak (Figure 4.3, Panel B). In some cases, there may be an instantaneous ashfall, but other features of the wider environment, such as seasonal snow cover, precipitation, local winds, or dense vegetation, slow tephra deposition into the lake, after which it is still susceptible to post depositional reworking. When the position of the tephra peak is indistinguishable from surrounding samples, and the maximum shard concentration is similar or comparable to the second highest shard concentration in the tephra layer, it is suitable to ascribe its stratigraphic position as a broader range of depths (Figure 5.2, Panel C; Davies 2015). In general, tephra concentration profiles

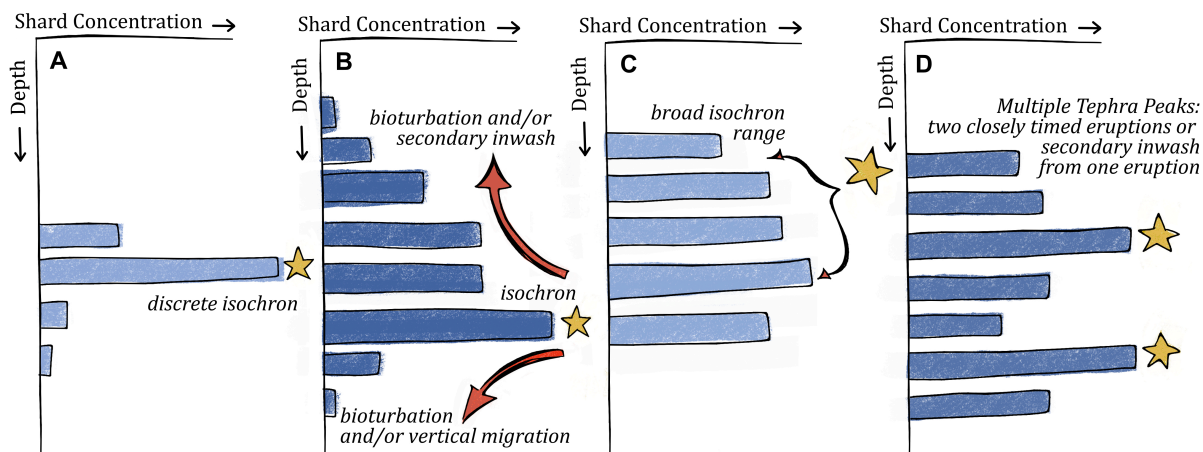


Figure 4.3: Schematic of common tephra concentration profiles (adapted from Davies 2015). The stars indicate where the stratigraphic position of a tephra layer would be assigned in the hypothetical sediment records.

often deviate from displaying discrete maximums and instead reflect the complexities of their depositional environments.

There is a possibility that tephra layers with more than one peak actually reflect separate, but closely-timed, eruptions (Figure 4.3, Panel D). This can be evidenced by the heterogeneity of the major and minor elements of the glass shards within the layer. If the tephra layer is composed of tephra shards with different geochemical signatures, than they likely originate from different volcanic sources. Depending on the volcanic origin relative to Bispingen, the strength of westerly winds, and regional climatic conditions (see Chapter 2), tephra from multiple eruptive sources may fall into the sediment record at a similar time, often appearing as a singular reworked layer without additional geochemical analysis.

Numerical Selection of Tephra Peaks

Identifying a stratigraphically significant tephra peak can also be described as identifying any usually large peaks in tephra shard concentration, or an outlier. There are three primary methods for calculating an outlier: using the the median, using mean and standard deviation (SD; Figure 4.5), and the Interquartile Range (IQR; Figure 4.4). Because a large majority of this dataset is composed of samples that contain zero tephra shards and the median of the total shards/g in the low resolution sequence is 0, the median value is not suitable measure to define tephra peak, as any sample containing more than zero shards would subsequently be considered at outlier. The IQR method measures the spread of the middle 50% of data, but much like the median value, the lower 25% quartile boundary is also 0. From the calculations using the formula in Figure 4.4, the upper threshold for outliers would be 6.86 shards/g, otherwise suggesting that all

samples containing more than 6.86 total shards/g are statistically significant peaks. In contrast, the SD method measures the spread of their entire dataset, calculated as mean plus two times the standard deviation (Figure 4.5). From this, the upper threshold for outliers would be 21.74 shards/g, otherwise suggesting that all samples containing more than 21.74 shards/g are statistically significant peaks. Regardless of how many outliers are identified, the EMPA instrument used for geochemical analysis can only hold up to 6 samples, so the number of samples selected to be reanalysed at a higher 1-cm resolution will be limited to the six most significant tephra peaks. This is more likely to apply to outliers identified using IQR method as it presents a lower minimum threshold value that would allow more samples containing tephra to be considered statistically significant from the rest.

$$\begin{aligned} \text{IQR} &= Q_3 - Q_1 && \text{(Interquartile Range)} \\ \text{Lower Bound} &= Q_1 - 1.5 \times \text{IQR} && \text{(Lower Outlier Limit)} \\ \text{Upper Bound} &= Q_3 + 1.5 \times \text{IQR} && \text{(Upper Outlier Limit)} \end{aligned}$$

Figure 4.4: IQR-based method for detecting outliers. The lower and upper bounds are determined based on the interquartile range.

$$\begin{aligned} \sigma &= \sqrt{\frac{1}{N} \sum_{i=1}^N (x_i - \mu)^2} && \text{(Standard Deviation)} \\ \text{Lower Bound} &= \mu - 2\sigma && \text{(Lower Outlier Limit)} \\ \text{Upper Bound} &= \mu + 2\sigma && \text{(Upper Outlier Limit)} \end{aligned}$$

Figure 4.5: Standard deviation method for detecting outliers. Values more than 2 standard deviations away from the mean are considered outliers.

4.4.1 Shard Picking

Following identification of samples with highest occurrence of tephra shards (detailed further in the results), 29 high-resolution samples were selected to allow the picking of shards for geochemical analysis. Glycerol-mounted high-resolution slides were soaked in 30-mL conical base centrifuge tubes with warm de-ionized water. The wider centrifuge tubes were used to let the entire microscope slide soak in the water for least 30 minutes. Once the glycerol dissolved completely in water, the slides were removed and the tubes were centrifuged to remove the excess dilute glycerol. The sediment was pipetted onto a wellled microscope slide, a few drops at a

time. Where tephra was present, individual shards were picked using a drawn-out glass Pasteur pipette, following the pollen picking technique of Seddon et al. 2017. Glass pipettes were warmed under a Bunsen burner and stretched an aperture small enough ($>100\ \mu\text{m}$) to pick up a single glass shard with as little surrounding material as possible, a precise method for extracting single shards of tephra, especially compared to the large openings on standard pipette tips, or even paintbrush bristles commonly used for dry micropalaeontological picking (e.g. Murray 2006).

4.5 Geochemical analysis

Geochemical analysis is the foundation of tephrochronology because it will identify the unique geochemical fingerprint of a tephra layer, which is then can be used to produce isochronous tephra networks between sites (Lowe 2011; Davies 2015). Geochemical analysis can also resolve nuances in shard concentration profiles by identifying whether a tephra layer is a homogenous entity from a single eruption or rather a heterogeneous conglomerate from multiple eruptions.

4.5.1 Stub Preparation

To prepare the samples for geochemical analysis they were mounted onto 25 mm stubs that were made to fit the EMPA instrument. First, small 4 mm circles were drawn onto a sheet of glass. Then a strip of heat resistant tape was placed onto the glass, fully covering each circle. Geochemical analysis requires that tephra shards are mounted to a flat surface so it is crucial that the strips of tape lie flat. Tephra shards from each sample were picked directly onto the tape, within one of these circles. The samples were covered at all times, other than when shards were being pipetted onto the tape, to prevent dust or any other airborne material in the laboratory from getting stuck onto the tape.

The next step was to create epoxy resin stubs that are secured onto the picked tephra shards. The stub preparation process occurred in the Thin Section Laboratory at University of Leeds. First, the stubs were made from pouring epoxy resin into 25 mm diameter moulds. After the stubs were hardened and removed from the moulds, the next step was to grind and polish them top create a perfectly flat surface on which tephra shards will lie. The resin stubs were first ground using a wet $40\ \mu\text{m}$ plate for about 10 minutes and then levelled using a $10\ \mu\text{m}$ plate for an additional 5-10 minutes. Once the surface of the stubs were completely level, the flat sides were polished over stages of increasingly smaller micron plates. The stubs were placed onto a polisher on a $6\ \mu\text{m}$ plate, then a $3\ \mu\text{m}$ plate, then a $1\ \mu\text{m}$ plate each for 5 minutes with the

associated diamond paste or suspension spray for each level. 4 mm diameter holes were drilled into the polished epoxy stubs. Then the epoxy resin stubs were placed onto the strips of heat resistant tape (described above), with the 4 mm hole in the stub lining up with the picked tephra lying within the 4 mm circle on the tape. The holes in stubs were backfilled with tephra and oven-dried overnight at 50° C. This method allowed the picked shards to already be exposed at the surface of the stub and be ready for polishing. Stubs were polished at 1 μm and 0.25 μm to ensure that the surface was level, but tephra shards are not damaged or removed from the hardened resin.

The alternative method mounting shards onto resin involves picking shards directly onto the stubs instead of onto heat resistant tape. The stubs would then be covered in a second layer epoxy resin and ground down again, with the same 40 μm and 10 μm plates used to level the original stub before tephra. However, an additional round of grinding leaves a greater risk for losing shards if they are not ground to the exact point in which the tephra shards are partially exposed. If the shards are too exposed, they may fall out of the resin; if shards are not exposed enough, then the electron beam may not actually hit the shard to provide accurate element analysis.

4.5.2 Electron Microprobe Analysis

After picking and mounting individual tephra shards, their major-oxide element compositions were measured using a JEOL JXA-8230 Electron Microprobe Analyzer (EMPA) equipped with five wavelength-dispersive spectrometers (WDS). EMPA-WDS was preferable to Scanning Electron Microscopy with Energy Dispersive Spectroscopy (SEM-EDS), because it relies more on well-known mineral standards for calibration that offers more precise element calculations (Hunt and Hill 2001). Analysis was conducted in the Electron Microscopy and Spectroscopy Centre of University of Leeds on October 8th and 9th, 2024.

Before using the instrument, samples were coated thin layers of carbon to ensure conductivity of the beam during analysis. The instrument was operated at an accelerating voltage of 15 kV, a beam current of 10 nA, and a defocused beam of 5 μm for area analyses. These requirements were specific to the EMPA at University of Leeds and may vary between facilities. However, general operating standards dictate that sodium should be measured first to reduce migration and that defocused beams should range between 5–10 μm (Hunt and Hill 1993; Hunt and Hill 2001; Hayward 2012). As silicic shards naturally contain higher levels of sodium than basaltic shards, they are more likely to experience sodium mobility and report under-represented abundances of this element (Hunt 1997). For the same reason, inversely, SiO_2 abundances may be



Figure 4.6: Image of JEOL JXA-8230 Electron Microprobe Analyser (EMPA) located in the Electron Microscopy and Spectroscopy Centre of University of Leeds.

over represented (Hunt and Hill 2001). EMPA analysis was performed at various points on material whose initial measurement indicated a potential tephra shard by yielding an analytical total exceeding 80 wt%. Multiple beam measurements taken from the same potential tephra shards were averaged.

Tephra originating from the same region may show similar geochemistries despite forming from different eruptions (Lowe 2011). Therefore, analysis requires a level of precision that can only be maintained through standard laboratory procedures across all facilities. To better differentiate between subtle signatures of various eruptions, mineral standards were employed to ensure the reliability and reproducibility of this data (Hunt et al. 1998). This study periodically analysed standards ML3B for basaltic affinities and Lipari for rhyolitic affinities to keep element calculations precise (Hunt and Hill 1993). Other primary and secondary standards included KL2-G Basaltic Glass, KL2-G Basaltic Glass, Rutile, Cr_2O_3 , Rhodonite, Diopside, Jadeite, Kspar, Apatite.

The major element compositions of tephra shards were further compared to non-glass matter that was mistakenly analysed because they may have appeared similar to tephra under partially-

exposed conditions. These objects were removed from the tephra data from their obvious non-volcanic glass geochemistry, but nonetheless served as reference values to narrow down which geochemistries did suggest tephra. The main element species analysed were SiO_2 , Al_2O_3 , FeO , CaO , Na_2O , K_2O , and Na_2O , MgO and MnO .

4.5.3 Data Comparison

The chemical composition data collected from this study was compared to the chemical composition data from known eruptions to pinpoint a possible volcanic source. To do this, the measured X-ray intensities were converted to weight percentages. Some samples that had higher silica concentrations and seemed to lean more towards rhyolitic compositions were recalibrated accordingly (see: Table 5.2). In these cases, silica and aluminium were both calibrated with a rhyolitic glass standard and sodium was recalibrated with a halite standard (Hunt and Hill 1993). Only samples with at least an 80% analytical total of combined element oxides compositions were considered for further analysis. This percentage is very low, with most studies establishing analytical total thresholds at at least 95% or above (Hunt and Hill 1993; Lowe 2011). However, the low percentages were still included because there were very few data points collected from the geochemical analysis due to the limited number of samples, and they were used to compare against more robust data points that aligned closer to common tephra compositions. Cr_2O_3 and P_2O_5 were subtracted from the total percentages, following the recommendation in Lowe et al. (2017) to omit trace elements, volatile elements, and minor element oxides less than 1 wt% (Winter 2009). Subtracting non-major elements had very little impact on the analytical totals because Cr_2O_3 and P_2O_5 were practically negligible (Table ??). In some samples, Cr_2O_3 displayed slightly negative values, upwards of -0.02%, suggesting that the actual concentrations of Cr were too low to be detected by the microprobe. Using the new totals, geochemical data was normalised to 100 wt% because it accounted for analytical errors and allowed for easier comparison to tephra records from other sites.

Bivariate-oxide plots are the common way of presenting data from volcanic material (Rollinson 2014). Volcanic material, like tephra, is also classified on total alkali versus silica (TAS) plots (see: Figure 4.7). The classifications originally proposed by Bas et al. (1992) allow potential tephra from this study to be compared to the TAS values of known tephra from other eruptions, ideally establishing isochronous links between geochemically similar shards deposited at the same time. Only the samples with an analytical totals above 80 wt% had total alkali and silica ratios that fell somewhere within the igneous classification, which contributed to setting this

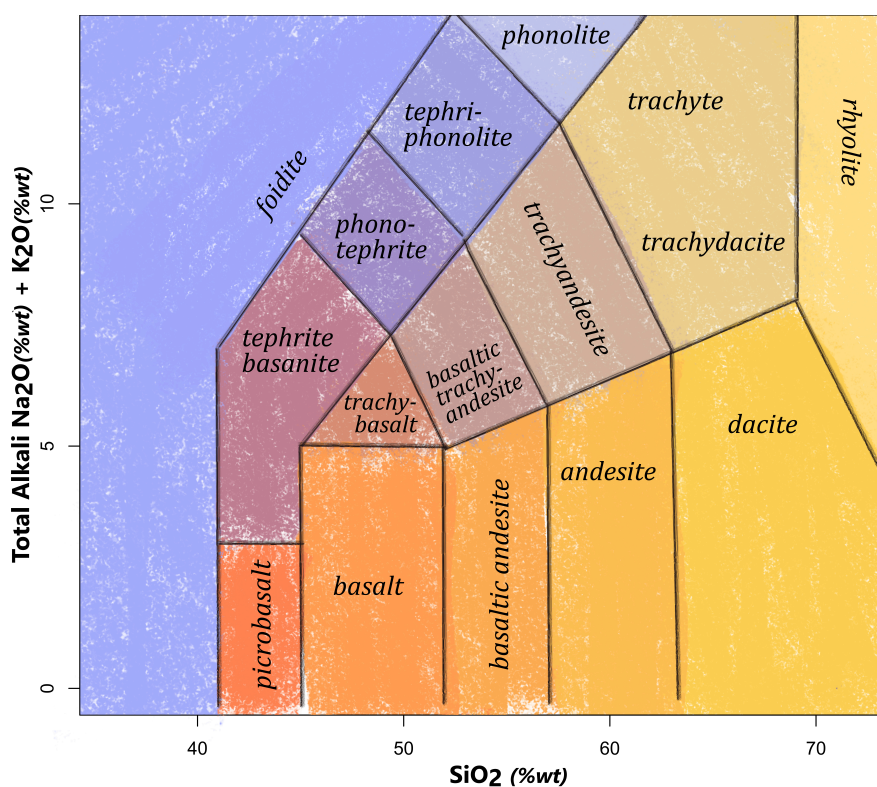


Figure 4.7: Total alkali vs silica plot illustrating the silica to total alkali ratios of common igneous rocks. The exact boundaries and classifications for volcanic rocks come from Bas et al. 1992. Total alkali is defined as the combined % weight of Na₂O and K₂O.

threshold. Following Lowe et al. (2017) and other Last Interglacial tephra studies, like Abbott, Austin, and Davies (2014), only shards with analytical totals above 95 wt% were normalised and further compared to normalised datasets from other sites.

However, because current knowledge of Last Interglacial eruptions is limited, there are not many known geochemical tephra profiles other than those collected in the Nordic Seas near Iceland (e.g. Sejrup et al. 1989; Sjøholm, Sejrup, and Furnes 1991; Fronval et al. 1998; Wastegård and Rasmussen 2001; Brendryen, Hafliðason, and Sejrup 2010; Abbott et al. 2011; Abbott et al. 2013; Abbott, Austin, and Davies 2014; Davies et al. 2014). Because the likelihood of finding a perfect match to one of these Icelandic records is not guaranteed, methodological approaches for establishing a precise tephrochronology are outside the scope of this paper. Instead, geochemical profiles will likely be used to categorize whether tephra peaks are primarily rhyolitic or basaltic. There is, of course, long-term scope for connecting geochemical profiles to future Last Interglacial tephra studies in Northwest Europe as they are collected.

As the depth of tephra layers will be linked to their respective depths in the Bispingen pollen sequence, the primary strength of this study focuses more on placing tephra in a stratigraphic sequence, rather than its distinct geochemical properties. The final step of this study is to pro-

pose other well-known Eemian pollen sequences that are likely to contain at least one of the tephra layers identified in the Bispingen record. Improvements to the current Last Interglacial chronology in Northwest Europe will be detailed further in Chapter 6.

4.6 Summary

The first goal of this study, to identify tephra in the Bispingen core, was achieved using techniques for isolating tephra shards from the sediment samples (e.g. wet sieving and density separation). The second goal of this study was achieved by Electron Microprobe analysis of select high resolution samples to characterize the geochemical fingerprints of tephra shards extracted from the BIS-2000 sequence. Lastly, the third goal of this study, to improve Last Interglacial chronology, was achieved by linking the depth of tephra layers to the depths within the Bispingen pollen sequence.

CHAPTER 5

RESULTS

This chapter presents the tephra count results from the 70 x 5 cm thick low-resolution samples and the 29 x 1 cm thick high-resolution samples. The first results are categorical descriptors of individual tephra shards, including size, shape, and colour. The second part of the results are quantitative descriptors of shard concentrations in both low resolution and then high resolution samples, followed by the geochemical analysis of select high-resolution samples.

5.1 Shard Morphologies

The clear shards all exhibited either platy or vesicular shards (Figure 5.1). The identified brown shards, naturally darker in colour, displayed less-distinct visual characteristics. Nevertheless, all shards were also identified by their ability to be extinguished under the cross-polarized light of a petrographic microscope. The range of tephra shard sizes lied roughly between 20 μm and 80 μm in diameter across their longest axis (Figure 5.1). In the low-resolution counts, the topmost tephra peak was the only one to contain a mix of both brown and clear shards, while the other remaining tephra peaks were entirely composed of clear shards. Both clear and brown shards were present in the high-resolution analysis, but clear shards were noticeably less vesicular.

5.2 Low-Resolution Shard Concentration Profiles

The dataset spanned the lower section of the BIS-2000 sequence from 2050 cm to 2399 cm and consisted of 70 5 cm-thick samples. Shard concentration profiles were made by counting the number of tephra shards found in each sample and dividing the number by the total weight of the dried sample before sieving. Samples that contained a large shard concentration in comparison to the neighbouring samples in the core were defined as a 'peak' (Figure 4.3). Within the 70 samples that comprised the lower section of the BIS-2000, several tephra peaks were identified (Figure 5.2). Applying the two measure of statistical significance to the low resolution dataset, the SD method roughly identifies three tephra peaks using a threshold value of 21.74 shards/g: 2302-2297 (24.84 shards/g); 2217-2213 cm (61.64 shards/g); 2113-2108 (33.53 shards/g). In

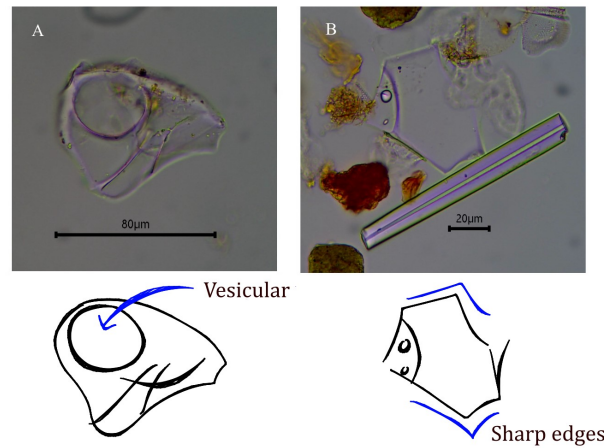


Figure 5.1: Comparison of clear tephra shards from Tephra Peak A in the low resolution sample between 2055 to 2050 cm. The shard in panel A is about 80 μm on its longest axis, while the shard in panels B is 20 μm . The shards in panels A shows vesicular edges, while the shard in panel B has a more platy morphology.

Table 5.1: Table showing the eight tephra peaks. selected for high-resolution analysis. The letters assigned to each peak are given in the left most column. The depths for each 5 cm sample are given in the middle-left columns. The shard concentration within each sample, in shards/g, are given in the middle-right column. The shard concentration was calculated using the total number of shards divided by the dry weight of the entire sample. The final column gives the statistical method used for identifying each tephra peak.

Tephra Peak	Lower Depth (cm)	Upper Depth (cm)	Concentration (shards/g)	Method
H	2337	2332	7.96	IQR
G	2307	2302	11.56	IQR
F	2302	2297	24.85	IQR; SD
E	2217	2213	61.64	IQR; SD
D	2188	2183	7.87	IQR
C	2161	2156	10.93	IQR
B	2113	2108	33.53	IQR; SD
A	2055	2050	21.40	IQR

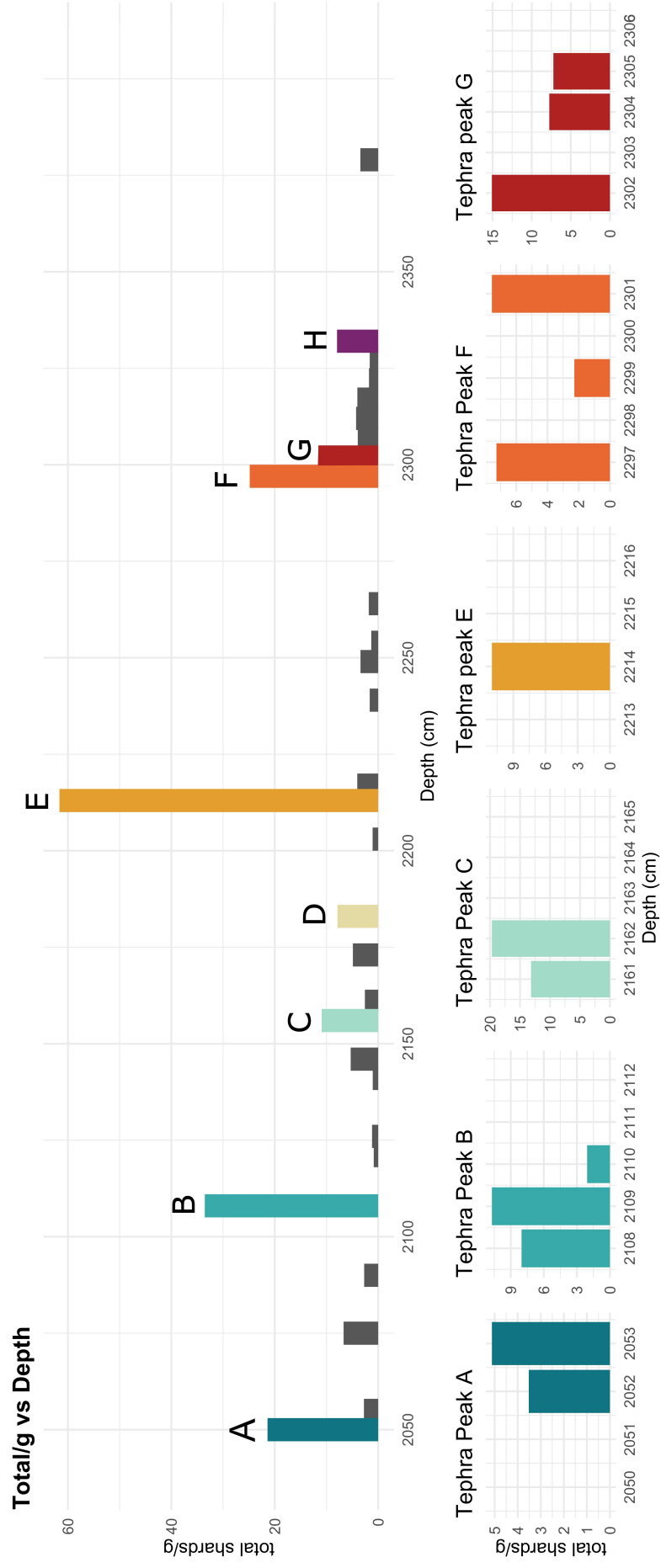
contrast, the IQR method identifies eight tephra peaks using a threshold value of 6.86 shards/g. These tephra peaks include the same three identified with the SD method, in addition to five more between 2337-2332 cm (7.96 shards/g); 2307-2302 cm (11.56 shards/g); 2183-2188 cm (7.87 shards/g); 2156-2151 cm (10.93 shards/g), 2055-2050 cm (21.40 shards/g). The latter IQR methods is favourable because it includes the final tephra peak of 21.40 shards/g, which is technically below the threshold value set using the SD method, although it only differs by a fraction of a tephra shard (0.3 shards/g). From this, tephra peaks will be hereafter defined using the IQR method.

The distribution of tephra shards throughout the studied part of the core was fairly spread out, with shards being found in every pollen zone (Figure 5.6; Selle 1962). However, very little-

to-no tephra was found in the bottom 60 cm of the sequence, between 2399 cm to 2340 cm, with the exception of about 3.5 shards/g found in a single 5 cm sample between 2384-2379 cm depth. Even in samples that contained no tephra shards, there were also no additional shards identified in the 1.95 g cm^{-3} and 2.51 g cm^{-3} density fractions that would suggest tephra peaks may be present within a different glass density.

Samples were selected for high-resolution analysis on the likelihood that they may present a potential tephra layer. As tephra layers are ideally deposited instantaneously after an eruption (Lowe 2011, Davies et al. 2014), a tephra layer would be found in a sample with a relatively large number of shards per gram (for this study >6.86 shards/g), with few or no shards in the neighbouring samples. The presence only a few shards in the samples below, and especially above, signifies that tephra was deposited rapidly with little post-depositional reworking (Figure 4.3). Well-preserved samples that meet these conditions provide more precise chemical profiles that strengthen their potential to be isochrons. However, due to the instrumental limit of the EMPA instrument addressed in the Methods chapter, only the six most significant peaks will be selected for 1 cm high-resolution analysis (Table 5.1). The tephra peaks are listed in chronological order with the first peak from the top of the sequence and the final tephra peak from the bottom of the sequence (Figure 5.2).

Figure 5.2: Low-resolution shard concentration profiles are shown on the top. Eight samples display distinct shard concentration maximums. Each colour corresponds to a specific tephra peak and its high-resolution shard concentration profile are shown in the inset figures below, where applicable.



Tephra Peaks G, H, and F are all found in a wide spread of tephra shards across eight 5-cm thick samples between 2337 cm to 2297 cm. Tephra Peak G is the very first sample to appear in this spread, and in the whole BIS-2000 sequence. It lies between 2337 cm and 2332 cm, and contains 7.96 shards/g. With the exception of a single sample that contains less than 3.5 shards/g, all 14 samples below Tephra Peak G contain zero tephra shards. The next two consecutive samples upcore each contain about one shard/g. The following two consecutive samples upcore each contain about 4 shards/g. Tephra H lies directly above this and contains 11.56 shards/g. Tephra Peak F lies directly above between 2302 and 2297 cm. This final and top-most sample in this tephra group contains 24.85 shards/g. The wider tephra group tended to increase upcore until reaching Tephra Peak F with a concentration of nearly 25 shards/g.

Tephra Peak E is found between 2217 cm and 2213 cm. The tephra peak occurs just above a large input of sediment at 2230 cm depth (Figure 5.6; Lauterbach et al. 2024). Tephra Peak E contains 61.64 shards/g and is the largest peak counted in the entirety of the studied BIS-2000 sequence. The next five samples that lie directly on top of Tephra Peak E contain practically zero tephra shards with the exception of one of these five samples containing just one shard/g. The sample directly below Tephra Peak E only contains about 4 shards/g. Given the low concentration of tephra in the sediment directly above and below Tephra Peak B, it was selected for 1 cm high-resolution analysis.

Tephra Peak D is found between 2188 cm and 2183 cm. This is the smallest significant tephra peak, at only 7.87 shards/g, but the surrounding samples contain no tephra. Tephra peak C is found between 2166 cm to 2561 cm. It has the lowest concentration of tephra out of the other peaks selected for high-resolution analysis, and it only had concentration of 10.93 shards/g. Tephra peak B was found between 2113 cm and 2108 cm. It had a shard concentration of 33.53 shards/g. There were no tephra shards found within 10 cm above and below the sample. Tephra peak A was identified between 2055 cm and 2050 cm. It contains a mix of shards, 13.62 clear shards/g and 7.78 brown shards/g, with a total of 21.40 shards/g. This was the only tephra peak that contained an obvious mix of both shard colour morphologies.

5.3 High-Resolution Shard Concentration Profiles

A total six samples were selected for high-resolution analysis, chosen by having the greatest shard concentrations/g (Table 5.1). Tephra Peaks F and G were both selected to see whether the tephra spread may have been produced from two distinct, but closely timed, eruptions or rather produced from a single eruption and later reworked.

The 70 low-resolution samples were all mounted permanently to microscope slides with Canada Basalm. Mistakenly, the first batch of high-resolution samples were also mounted to microscope slides with Canada Basalm, preventing the material found on these slides to be dissolved and picked from the medium. Nevertheless, very few tephra shards were found in this first batch. 12 out of 15 samples from this first batch contained zero tephra shards, and the three remaining samples that did contain tephra only held about 4 shards/g. The remaining section of high-resolution analysis, therefore, is limited to tephra found in the second batch that was properly mounted with a temporary glycerol medium (Figure 5.2).

The high-resolution shard concentration profile of Tephra Peaks G and F are a combined 10 1-cm thick samples: 5 1-cm samples from Tephra Peak G (2307-2302 cm) and 5 1-cm samples from Tephra Peak F (2302-2297 cm) directly above. Unlike the other high-resolution tephra profiles, Tephra Peaks G and F contain multiple small peaks, with some samples in between containing no shards at all. Within the 10 cm group, the maximum shard concentration of about 15 shards/g occurs in a middle samples between 2303-2302 cm. Out of the remaining nine samples, four of them have shard concentrations near 7 shards/g, one has a shard concentration near 2 shards/g, and four have no tephra. Out of the five remaining samples that contain tephra, all are mixed with both clear and brown shards, but the peak between 2303-2302 cm contains only clear shards.

The high-resolution profile of Tephra Peak E is a group of five 1-cm thick samples between 2217-2213 cm. All tephra shards found within the high-resolution analysis of Tephra Peak B were found within one single 1 cm sample that has a concentration of 11 shards/g, evenly split between 5.5 clear shards/g and 5.5 brown shards/g.

The high-resolution profile of Tephra Peak C is a group of five 1-cm thick samples between 2166-2161 cm. Tephra shards were only found in the top two samples: between 2163-2161 cm. The 1-cm sample between 2162-2161 cm has a concentration of about 13 shards/g and is mixed between about 10 clear shards/g and 3 brown shards/g. However, the 1-cm sample between 2163-2162 cm has a concentration of almost 20 shards/g. This sample contains both shard colour morphologies but largely favours brown shards with about 16 brown shards/g and only 4 clear shards/g.

The high-resolution profile of Tephra Peak B is a group of five 1-cm thick samples between 2113-2108 cm. Tephra shards were found in the top three samples between 2108 cm and 2110 cm. The middle sample between 2109 and 2110 cm has the greatest concentration of 10.71 shards/g mixed between both shard colour morphologies.

The high-resolution profile of Tephra Peak A is a group of five 1-cm samples between 2055-

2050 cm. Tephra shards were found in the lower 2 cm of this section: 2052 to 2053 cm. The 1-cm sample between 2052 cm has a concentration of about 3.5 shards/g and only contains one brown shard and a one clear shard. The 1-cm sample at 2053 cm has a concentration of 5 clear shards/g.

5.4 Geochemical Analysis

Out of the 70 low resolution samples, six were chosen for high resolution analysis. The six 5 cm-thick low resolution samples produced 29 1-cm samples. Then, six of these 1-cm samples were chosen for geochemical analysis in the electron microprobe on the basis of the shard concentration. Two of the samples, upon looking at them under a microscope prior to analysis did not appear to successfully mount any tephra. These were excluded from geochemical analysis. Possible tephra was only found on four of the six samples: BIS 1-9 20-19 cm, BIS 1-9 19-18 cm, BIS 3-8 88-87 cm, BIS 3-8 87-86 cm. The two samples that consecutively cover BIS 1-9 18-20 cm were from Tephra Peak A and correlate to 2056 to 2054 cm in the composite BIS-2000 sequence. The two samples that consecutively cover BIS 3-8 88-86 cm are from Tephra Peak C and correlate to 2163 to 2161 cm in the composite BIS-2000 sequence. Normalized data is given in Table 5.3. The normalized data omits Cr_2O_3 , MnO , and P_2O_5 following Lowe et al. (2017) to exclude more trace and volatile elements. As shown in Table 5.3, the majority of these trace oxide concentrations are very small, if not below detection limits, which are reported as such.

5.4.1 Raw Data

The initial analysis of the tephra samples involved examining the raw, non-normalised elemental compositions. This approach allowed for a comprehensive understanding of the inherent geochemical variability present within the samples. The raw data, encompassing major element oxides, was systematically catalogued into bivariate plots to discern patterns and correlations within the dataset. The use of raw data provided a robust framework for subsequent comparative analyses, ensuring that the intrinsic geochemical characteristics were preserved and accurately represented in an otherwise small dataset.

All of the samples on the TAS plot were assumed to be volcanic material, if not tephra. There was one possible shard (sample 195_S6 in Table 5.2) that was removed before plotting on the basis of its geochemistry. It contained considerably low raw percentage of SiO_2 (35.5 wt%) and an anomalously high raw FeO percentage (39 wt%). While mafic materials tend to contain lower silica and higher iron, such low silica and such high FeO is uncharacteristic of

tephra. Nevertheless, the TAS plot reveals two clusters. The first cluster (dark green; Figure 5.3) is composed of five tephra shards from BIS 1-9 19-18 cm, which correlated to 2055-2054 cm in the compiled BIS-2000 sequence. The SiO₂ percentage of the cluster ranged between 65 wt% and 73 wt%, split between rhyolitic and slightly trachytic compositions. For the most part, and in comparison to the other samples, this cluster may be simplified to being rhyolitic. The five shard cluster contains very high total alkali, between 14-15 wt%. The BIS 1-9 19-18 cm sample contains six total shards, including the five shards clustered with comparable TAS ratios, and one additional one with 63 wt% SiO₂ and 4.7 wt% total alkali. The lower total alkali places the sixth shard towards a trachydacitic composition, but because it still exhibits a relative high SiO₂ composition (>60 wt%) it is considered in population A of Tephra Peak A. However, the second sample from tephra peak A, BIS 1-9 20-19 cm, contains a much more basaltic composition with a singular shard composed of about 50 wt% SiO₂ and >6 wt% total alkali. This shard contains about 20 wt% iron, while more than most tephra shards, was still much less than the other iron-rich data point that was removed from this sample.

The second cluster (Figure 5.3) falls within the range of a trachytic composition, having two shards with intermediate-to-high SiO₂ (61 wt% and 62 wt%) and intermediate-to-high total alkali (9.5 wt% and 11.5 wt%). The shard from sample BIS 3-8 87-86 cm, which correlates to 2164-2163 cm in BIS-2000, contains a much more basaltic composition and is considered part of a population B (dark blue; lower left corner; Figure 5.3). This shard has only 47 wt% SiO₂ and total alkali <6 wt%.

Comparing SiO₂ to individual oxides finds that the two basaltic leaning shards from Tephra Peaks A and C have high FeO levels (15 wt% and >20 wt%) while the two rhyolitic populations have much lower FeO levels (<1 wt%). The difference in total alkali between the basaltic populations and the rhyolitic populations largely lies in opposite amounts of sodium and potassium (Figure 5.3). The rhyolitic populations from both tephra peaks range from 8 wt% to 14 wt% Na₂O. The sixth shard outside of the cluster from Population A of Tephra Peak A contains lower Na₂O (<4 wt%). Population A of Tephra peak C contains very low K₂O (<1 wt%), and Population A of Tephra Peak A had wider range of K₂O that averaged around 3 wt%. In contrast, the two basaltic shards from Tephra Peak A and C contain <1 wt% Na₂O but >5 wt% K₂O. Results for MnO and P₂O₅, while included in the raw total percentage, were not plotted because many of the values were slightly negative and/or near zero (Table 5.2), suggesting that the percentages were below the instrument detection limits (Lowe et al. 2017).

BIS-2000 Geochemical Analysis - Raw Data

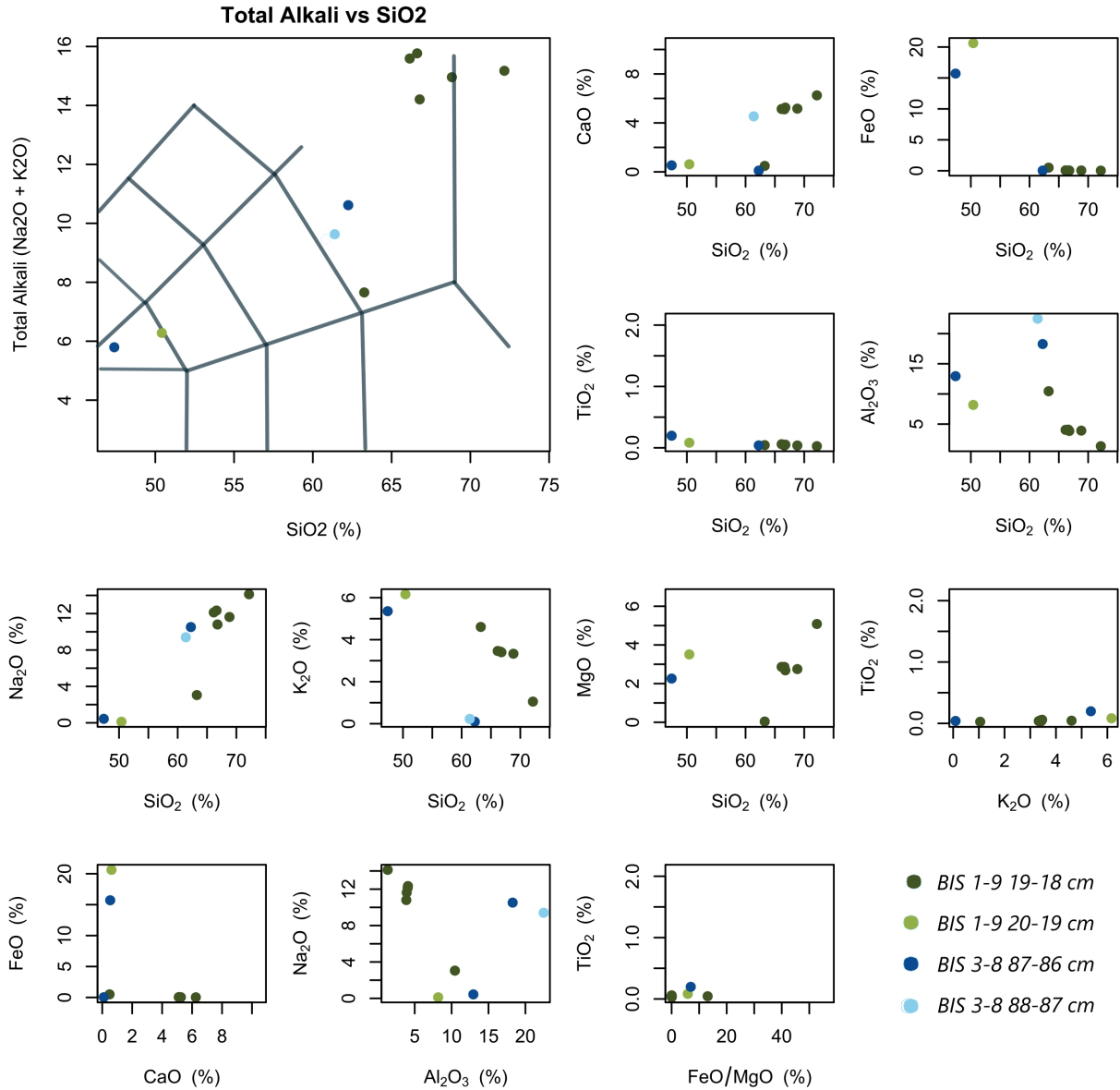


Figure 5.3: Geochemical bivariate plots of major-element data from Bispingen cryptotephra. All data presented are raw. Reference igneous rock classifications for total alkali vs. silica plot (top left) taken from Bas et al. (1992). Green data points (light and dark) are from Tephra Peak A in core BIS 1-9 and blue data points (light and dark) are from Tephra Peak C in core BIS 3-8. The cluster of dark green points in the top-right of the TAS is associated with Population A of Tephra Peak A. The two blue data points (one dark; one light) are associated with Population A of Tephra Peak C. Clustered shards are those that exhibit very similar geochemistries within the same sample. Population in this study is used a wider term for shards within the same sample whose comparable TAS geochemistries suggest they may come from the same volcanic origin.

Table 5.2: Table of the major element oxides raw wt%. The samples listed in the first column follow the format of sample#_shard#. Where multiple measurements could be taken from the same shard, these numbers are already averaged in the table. Sample 196 is Tephra Peak A Population A; Sample 195 is Tephra Peak A Population B; Samples 184 are Tephra Peak C Population A; Samples 183 is Tephra Peak Population B. The final two rows are the averaged measurements of the ML3B and Lipari standards used to calibrate periodically between measurements. Sample 195_S6 was deemed not tephra on the basis of its usually high Iron content and was removed from further analysis, but it is still shown in the table. All other shards were used in analysis.

SAMPLE	SiO₂	TiO₂	Al₂O₃	Cr₂O₃	FeO	MnO	MgO	CaO	Na₂O	K₂O	P₂O₅	TOTAL
196_S1	68.83	0.04	3.92	<0.05	0.05	<0.05	2.75	5.16	11.63	3.33	<0.05	95.75
196_S2	66.78	0.05	3.86	<0.05	0.04	<0.05	2.69	5.25	10.80	3.40	<0.05	92.90
196_S3	72.16	0.03	1.34	<0.05	0.02	<0.05	5.08	6.25	14.12	1.05	<0.05	100.06
196_S4	66.62	0.04	4.08	<0.05	0.05	<0.05	2.86	5.11	12.34	3.43	<0.05	94.58
196_S8	66.15	0.06	4.05	<0.05	0.06	<0.05	2.86	5.14	12.13	3.46	<0.05	93.93
196_S10	63.26	0.04	10.45	<0.05	0.50	0.06	0.04	0.49	3.05	4.61	0.12	82.64
195_S4	50.41	0.08	8.18	0.06	20.63	<0.06	3.51	0.62	0.12	6.16	0.19	89.97
195_S6	35.75	<0.03	0.67	<0.05	39.42	<0.06	0.12	0.60	0.34	0.31	3.89	81.06
183_S1	47.40	0.20	12.95	0.02	15.71	<0.06	2.26	0.53	0.44	5.36	0.73	85.56
183_S3	62.25	0.04	18.27	<0.05	0.03	<0.05	<0.02	0.10	10.52	0.09	<0.04	91.33
184_S3	61.39	<0.03	22.47	<0.05	<0.06	<0.05	<0.02	4.53	9.40	0.23	0.22	98.25
ML3B check	51.76	2.10	13.78	<0.05	11.13	0.17	6.62	10.52	2.36	0.43	0.26	99.12
Lipari check	73.99	0.08	12.96	<0.05	1.59	0.07	0.03	0.76	4.17	5.57	<0.05	99.21

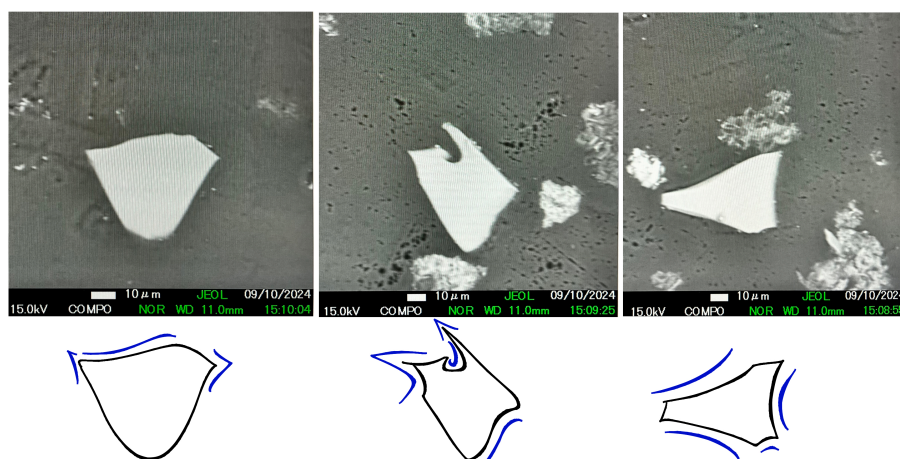


Figure 5.4: Images of analysed shards from five-shard cluster of Tephra Peak A.

5.4.2 Normalised Data

The data was also normalized to 100 wt%, which is often done in tephra studies to compare geochemistries between sites, and it tends to exclude trace elements and volatiles, which in this study, included MnO, P₂O₅, Cr₂O₅ (Lowe et al. 2017). Normalising involves recalculating the total oxide sums to 100 wt%. However, normal data assumes that the deficit in analytical totals below 100 wt% is entirely attributed to loss of water (Lowe et al. 2017).

First, the sample from BIS 1-9 18-19 cm contains five possible tephra shards (Figure 5.4, four of which have total alkali percentages around 15 wt%, and one just under 10 wt%, all within a rhyolitic classification. The sample below this, BIS 1-9 19-20 contains two possible shards, one with very low silica at 45 wt% and likewise very low total alkali just under 1 wt%, and the second one with intermediate silica at 56 wt% and likewise intermediate total alkali at 7 wt%. The low silica and low total alkali material has a distinct basaltic composition, while the intermediate silica and intermediate total alkali material has a trachytic composition, both classified by their position on the TAS plot (Figure 5.5).

The sample from BIS 3-8 86-87 cm contains two possible tephra shards. One shard contains 56 wt% silica and just under 7 wt% total alkali, overlapping slightly with one of the shards from BIS 1-9 19-20 cm, both of which are classified as trachytic. The second possible shard contained 68 wt% silica and about 11.5 wt% total alkali. This aligns much more with rhyolitic compositions (Figure 5.5).

The first set of bivariate oxide plots compares each oxide to silica. The five blue data points from BIS 18-19 cm that are clustered near to each other in the TAS plot (Figure 5.5) are also clustered together throughout the other bivariate oxide plots, showing comparable ratios of CaO vs SiO₂, FeO vs SiO₂, TiO₂ vs SiO₂, Al₂O₃ vs SiO₂, and Na₂O. There was a slight variability in

BIS-2000 Geochemical Analysis - Normal Data

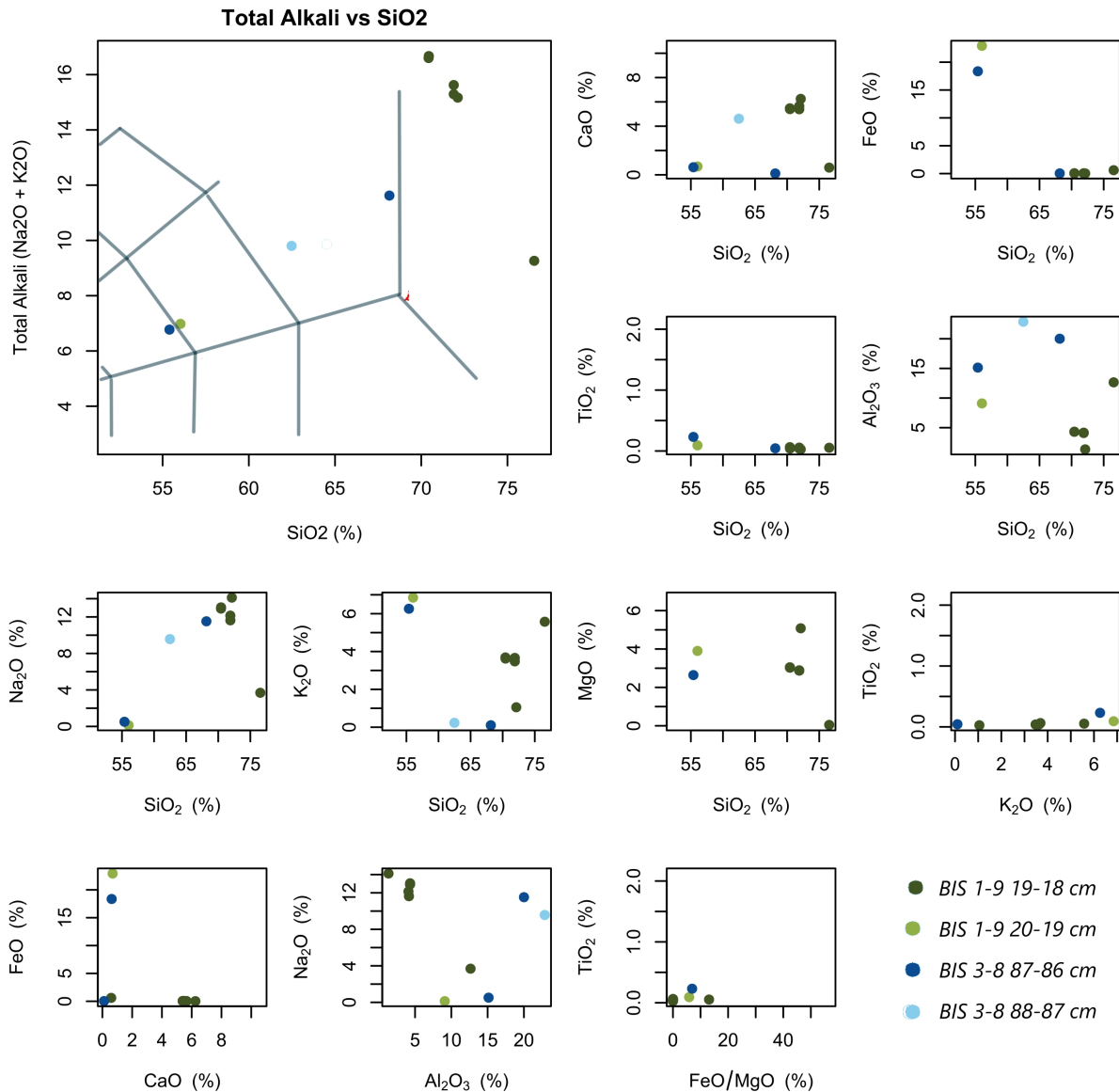


Figure 5.5: Geochemical bivariate plots of major-element data from Bispingen cryptotephra. All data presented are normalised to 100 wt%. Reference igneous rock classifications for total alkali vs. silica plot (top left) taken from Bas et al. (1992). Green data points (light and dark) are from Tephra Peak A in core BIS 1-9 and blue data points (light and dark) are from Tephra Peak C in core BIS 3-8. The cluster of dark green points in the top-right of the TAS is associated with Population A of Tephra Peak A. The two blue data points (one dark; one light) are associated with Population A of Tephra Peak C. Clustered shards are those that exhibit very similar geochemistries within the same sample. Population in this study is used a wider term for shards within the same sample whose comparable TAS geochemistries suggest they may come from the same volcanic origin. The individual points refer to the geochemical compositions of one individual shard, averaged if multiple measurements were taken.

K_2O vs SiO_2 in which one of the four clustered points has a slightly lower ratio. The remaining sixth data point that has a slightly higher silica content and slightly lower total alkali content than the other clustered data points on TAS plot also deviates from the other data points in the bivariate oxide plots (Figure 5.5). The five points from BIS 1-9 18-19 cm still share similar geochemistries in bivariate oxide plots excluding silica (TiO_2 vs K_2O , FeO vs CaO , Na_2O vs Al_2O_3 , TiO_2 vs FeO/MgO).

Table 5.3: Table of normalised major element data, using the raw data and adjusting the analytical totals to 100 wt%. The samples listed in the first column follow the format of sample#_shard#. Where multiple measurements could be taken from the same shard, these numbers are already averaged in the table. Sample 196 is Tephra Peak A Population A; Sample 195 is Tephra Peak A Population B; Samples 184 are Tephra Peak C Population A; Samples 183 is Tephra Peak Population B. The final two rows are the averaged measurements of the ML3B and Lipari standards used to calibrate periodically between measurements. Sample 195_S6 was deemed not tephra on the basis of its usually high Iron content and was removed from further analysis, but it is still shown in the table. All other shards were used in analysis.

SAMPLE	SiO₂	TiO₂	Al₂O₃	Cr₂O₃	FeO	MnO	MgO	CaO	Na₂O	K₂O	P₂O₅	TOTAL
196_S1	71.89	0.04	4.09	<0.05	0.05	<0.05	2.87	5.39	12.14			
196_S2	71.89	0.06	4.16	<0.05	0.04	<0.05	2.89	5.65	11.63			
196_S3	72.12	0.03	1.34	<0.05	0.02	<0.05	5.08	6.25	14.11			
196_S4	70.44	0.04	4.32	<0.05	0.05	<0.05	3.03	5.40	13.05			
196_S8	70.43	0.06	4.31	<0.05	0.06	<0.05	3.05	5.47	12.91			
196_S9	99.08	<0.03	0.11	<0.05	0.27	<0.05	0.07	0.06	0.03			
196_S10	76.55	0.05	12.65	<0.05	0.61	0.07	0.05	0.59	3.69			
195_S4	56.03	0.09	9.09	0.07	22.93	<0.06	3.90	0.69	0.13			
195_S6	44.10	<0.03	0.82	<0.05	48.64	<0.06	0.15	0.74	0.41			
183_S1	55.40	0.23	15.13	0.02	18.36	<0.06	2.64	0.62	0.51			
183_S3	68.15	0.04	20.01	<0.05	0.04	<0.05	<0.02	0.11	11.52			
184_S3	62.48	<0.03	22.87	<0.05	<0.06	<0.05	<0.02	4.62	9.57			
ML3B check	52.21	2.12	13.90	<0.05	11.23	0.17	6.68	10.61	2.38			

For the most part, normalising the data did not have a large impact on the dataset. The broader igneous rock classifications of raw tephra shard data on the TAS plot stayed the same after normalising. Population A of Tephra peak A was still rhyolitic with high SiO₂ (>65 wt%) and high total alkali (15 wt%), and the one trachytic shard with lower SiO₂ and total alkali. Likewise, while the two shards from population A of Tephra Peak C were still trachytic after normalizing, one shifted towards a more basaltic composition (Figure 5.5). The classifications of tephra shards were roughly similar before and after normalising, but the raw data kept these points clustered closer together for more concise identification of populations. For this reason, both the raw and normalised data from Bispingen were compared to their respective raw and normalised tephra datasets from other sites in Chapter 6. Normalising a dataset to draw foreign comparisons is often for larger datasets with higher total percentages, but in this case, redistributing element abundances to achieve a 100 wt% total may add extra assumptions to an already small dataset that exhibits multiple types of tephra between only a few shards in each sample. Therefore, only four shards from Population A of Tephra A are used for comparison in the following chapter because they exhibited raw total wt% above 95%.

5.5 Bispingen Pollen Record

The pollen data presented in this section (Figure 5.6), alongside collect tephra data, was obtained from the re-investigation of the Bispingen sediment succession in Northern Germany by Lauterbach et al. (2024). The previous study provided comprehensive sediment microfacies, geochemistry, and pollen data. A sedimentological and palynological overview of the all the pollen zones from I to IV, can be found in Chapter 3). A more in-depth comparison of the sedimentation rates and pollen data between the BIS-2000 sequence and the original KS 186/70 core by Müller (1974) can be found directly in the re-investigation paper by Lauterbach et al. 2024. Here I compare my tephra results alongside the position of the primary Geramn pollen zones originally from Selle (1962) and used by Lauterbach et al. (2024).

The pollen zones in the BIS-2000 sequence (Lauterbach et al. 2024) were matched by depth to the shard concentration profile collected in this study (Figure 5.6). In the BIS-2000 sequence, there are two tephra peaks found in the unvarved diatomic sediments associated with the upper pollen assemblage zone VIb. The remaining three tephra peaks are found throughout the faintly varved calcitic sediments associated with pollen zones VIa through IVb. Pollen zones VI and V each corresponded to 2000 years in the sediment record, while the lower IV pollen zone is part of a 4000 year section of the sediment record, the rest of which was not included in the sequence

(Lauterbach et al. 2024). Pollen zone VI had the highest sedimentation rate of 0.740 mm, and pollen zone V had the lowest sedimentation rate of 0.535 mm (calculated by Lauterbach et al. 2024 using data from Müller 1974).

Pollen Zone IV spans 2731 -2303 cm. This 428 cm-thick section covered 7133 years, estimated based upon the sedimentation rate of 0.600 mm/year (Lauterbach et al. 2024). Only the upper 100 cm are used in this study, in substage IVb. The pollen zone was dominated by *Carpinus* taxa, and *Picea* and *Pinus* were also present. By this point in the BIS-2000 sequence, Lauterbach et al. (2024) suggested that the interglacial forest began. Tephra Peaks H, G, and F were found towards the end of Pollen Zone IVb (Figure 5.6).

This is then followed by Pollen Zone Va that spans from 2303 cm to 2269 cm. This 34 cm-thick section covered 636 years, estimated using the sedimentation rate of 0.535 mm/year (Lauterbach et al. 2024). The pollen zone was abundant in *Pinus*, *Picea*, and *Carpinus* taxa. *Abies* also increased significantly. Pollen Zone Vb spanned from 2269 cm to 2175 cm. This 94 cm thick section covers 1421 years, estimated using the same sedimentation rate of 0.535 mm/year as the zone below (Lauterbach et al. 2024). The pollen zone was abundant in *Pinus*, *Picea* and *Abies*. *Pinus* and *Picea* were still present while *Abies* continued to decrease. The study suggested that Pollen Zone V covered about 130 years in total and marked the onset of climate cooling and the start of forest decline. Tephra Peak E is found within the middle of Pollen Zone Vb, and Tephra Peak D is found at the end of Pollen Zone Vb (Figure 5.6).

Pollen and Tephra Counts

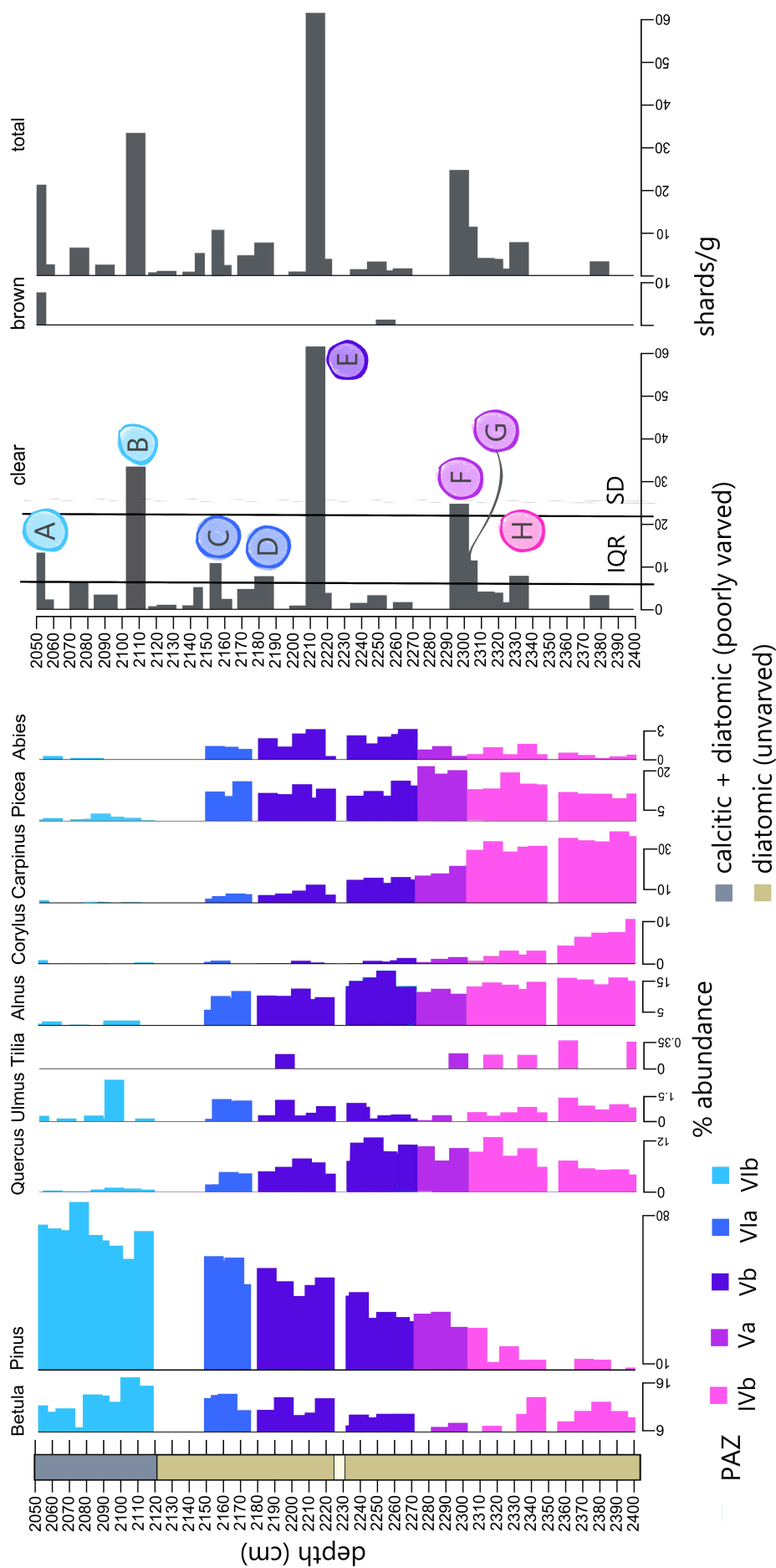


Figure 5.6: The left most figure shows the major sedimentological properties of the BIS-2000 sequence (data from Lauterbach et al. 2024). The grey calcitic + diatomic sediments are associated with Unit 4 and the tan diatomic sediments are associated with Unit 3 (also see Figure 3.4). The middle figure shows the percent abundances of common pollen taxa from the BIS-2000 sequence (data from Lauterbach et al. 2024). The right figure shows the low-resolution tephra shard concentration profiles collected in this study, separated between clear shards, brown shards, and the total of both shard colours. Pink represents the deepest pollen zone used in this study (PAZ IVb) and light blue represents the topmost pollen zone used in this study (PAZ VIb). The names of each tephra peak (E-A) are highlighted according to which pollen zone they are found in. Tephra Peak A is found at the beginning of PAZ Va, but there are some tephra layers below it that are also found in PAZ IVb. The remaining tephra peaks are not found as close to a transition between pollen zones and are easier to distinguish using the PAZ legend within the figure.

Pollen Zone VIa spans from 2175 to 2134 cm. This 41 cm-thick section covered 554 years, estimated using a sedimentation rate of 0.740 mm/year (Lauterbach et al. 2024). The pollen was abundant in *Picea* and *Pinus* taxa. *Betula* is still present and both *Pinus*, and NAP increased from Pollen Zone V. Pollen Zone VIb spans from 2134 cm to 2046 cm. This 88 cm-thick section covers 1189 years, estimated using the same sedimentation rate of 0.740 mm/year (Lauterbach et al. 2024). In Pollen Zone VIb, *Pinus* and *Betula* are still present, and NAP increases significantly to over 25 wt%. The study suggests that Pollen Zone VI ended the interglacial period. Tephra Peak C is found in Pollen Zone VIa, and Tephra Peaks A and B are found in Pollen Zone VIb (Figure 5.6).

5.6 Summary

The tephra shards found in BIS-2000 are categorized into clear and brown shards between 20 μm to 80 μm . The study analysed 70 samples, identifying several tephra peaks. Tephra Peak A is the only major horizon with a mix of clear and brown shards. Tephra Peak E contains has the greatest shard concentration, also accompanied by very low shard concentrations in the neighbouring samples directly above and below. Six samples were selected for detailed analysis. Tephra Peak A contains a cluster of five rhyolite shards, while Tephra Peak C has lower silica and total alkali percentages, leaning more towards a trachytic composition. The Bispingen pollen data is linked with tephra shard concentration profiles, identifying tephra peaks and the corresponding pollen zones they lie in. The results are compared to other regional tephra datasets in the following chapter.

CHAPTER 6

DISCUSSION

The overall structure of this chapter is based upon the three research objectives listed in Chapter 1. This chapter provides local sedimentological and palaeoenvironmental evidence to argue which tephra layers in the Bispingen record have the potential to act as chronostratigraphic markers. To fully harness the potential power of tephra layers during the Last Interglacial, I also propose to revisit other well-studied sequences in Northwest Europe. If the Bispingen record can be tephrostratigraphically linked to these other sites, they would each offer different perspectives on the timing of climate and sea-level responses during the Last Interglacial.

6.1 Identifying cryptotephra shards in the Bispingen sequence

No macrotephra was visible from the sediment, but cryptotephra could be extracted and counted at the microscopic level by employing density separation techniques. The overwhelming majority of these shards were clear, vesicular, and platy, exhibiting morphological characteristics usually attributed to silicic glass (Figure 5.4; Figure 5.6; Kvamme et al. 1989). The density separation process often favours silicic shards over basaltic shards because they are less dense (Blockley et al. 2005), but the over representation of silicic shards may also be attributed to post-eruptive and post depositional processes discussed later in the chapter (Wastegard and Davies 2009).

Not only were shards detected in the Bispingen, many of these shards were detected within the same sample suggesting the presence of several tephra layers. To fundamentally use these tephra layers as chronostratigraphic markers in Northern Europe, their exact position in the sediment sequence must be precisely defined (Davies 2015). The stratigraphic position of a tephra layer is typically easy to quantitatively identify by referring to an obvious maximum shard concentration (Figure 5.2; Davies 2015). There were eight samples that displayed distinct peaks in tephra shard concentrations compared to their surrounding samples, six of which were selected for high resolution analysis (Figure 5.2).

6.1.1 Tephra Peak H

Tephra Peak H is found towards the bottom of the BIS-2000 sequence in Pollen Zone IVb and has a concentration of just under 8 shards/g (Figure 4.3; Figure 5.6).. As there is no high-resolution data to provide information on the stratigraphy at a 1-cm resolution, the stratigraphic position of Tephra Peak H is limited to the wider 5-cm range of 2337 cm to 2332 cm depth. This tephra peak marks the first appearance of a significant tephra layer in the sediment sequence, as all the samples downcore are entirely devoid of tephra with the exception of a single 5 cm-thick sample. There are five samples, encompassing a total 25 cm in-between Tephra Peak H and the slightly upcore Tephra Peaks G and F (Figure 4.3). These intermediary samples all contain less than 5 shards/g and not considered statistically significant by either method used in Chapter 4. The intermediate samples may be a sign of depositional reworking from Tephra Peak H or even a combination of other environmental lags from Tephra Peaks G and F that lie above.

6.1.2 Tephra Peaks G and F

Tephra Peak G is found towards the top of Pollen Zone IVb, directly below Tephra Peak F (Figure 5.6).. The stratigraphic position of Tephra Peak G likely occurs between 2302 cm and 2303 cm because this 1-cm sample contained 15 shards/g, although two 1-cm samples slightly downcore between 2304 cm and 2306 cm each contain about 6 shards/g (Figure 4.3). There are two shard concentration maximums in the high-resolution analysis of Tephra Peak F that make identifying a specific stratigraphic position more difficult. The bottom-most 1-cm between 2301 cm and 2302 cm sample contains just over 7 shards/g, which would align well with the stratigraphic position of Tephra Peak G at 3202 cm, but 6 shards/g were also found in the top-most sample between 2297 cm and 2298 cm (Figure 4.3). The vertical distributions of Tephra Peak F and the samples below are highly variable, with shard concentrations generally decreasing below the peak, which has a maximum concentration of about 25 shards per gram. No shards are present in the next several samples upcore. This distribution is quite unique because post depositional reworking usually produces a tephra profile in which the concentration of shards decreases after the maximum, suggesting some shards were displaced in the sequence only after the primary airfall layer. Tephra Peak F displays a similar signature tail of decreasing shard concentration, but only before the maximum (Figure 5.2). This has been observed in lakes near volcanoes, where macrotephra layers are exposed to seismic liquefaction that can displace tephra downcore (i.e. Beierle and Bond 2002), but cryptotephra layers are generally not thick enough to exert

such pressure on underlying sediments. Previous cryptotephra studies have still recorded similar spatial distributions in which tephra shards are also present below peak shard concentration; however, they are found within the preceding 10 cm (e.g. Turney et al. 2006), while the tephra preceding Tephra Peak F extends over 40 cm downcore. If we considered the continuous presence of tephra altogether, defining the stratigraphic position at first layer in which tephra occurs, the eruptive event would be Tephra Peak H at 2237 cm depth. However, if we assume the stratigraphic position as the maximum shard concentration, the eruptive event would be Tephra Peak F at 2297 cm depth. Because the spatial distribution is very unique, it is reasonable to assume that there are multiple factors influencing the sediment record.

It is possible for tephra shards to be displaced downwards by density sinking, or by other internal lake processes that delay primary deposition (Turney et al. 2006). Finding more dense basaltic shards just below a peak may help strengthen a case for density sinking (Pyne-O'Donnell 2010), but there were not enough brown-coloured shards in the Bispingen sequence to fully test this hypothesis. Because the two cores comprising the composite BIS-2000 sequence were retrieved near the margin of the palaeolake, it is also possible that plant roots caused a downward reworking of tephra (Figure 3.3; Davies et al. 2005; Turney et al. 2006; Pyne-O'Donnell 2010). Tephra Peak F is found in the less varved section of the Bispingen sequence, so the poorly defined annual sediment layers would also reflect increases in post depositional processes, like bioturbation or sediment mixing, that redistribute tephra up or down-core (Wheatcroft et al. 1990).

As Tephra Peak F occurs just before the transition from Pollen Zone IV to V, the water table was readily decreasing to where Saalian incised lakes near the Elbe River valley became swamp-like environments (Hein et al. 2021). NAP increase from 2-4‰ in Pollen Zone IV to about 4‰ in Pollen Zone V (Lauterbach et al. 2024). The increase in local vegetation density at the time of Tephra Peak F may have slowed water flow into the lake catchment area (Boygale 1999, Hein et al. 2021). Delayed in-wash of tephra into Bispingen could produce a concentration profile that spreads across several samples, as seen in the unusual shard distribution between Tephra Peak G and F. Nevertheless, the wider distribution all the way downcore to Tephra Peak H, nearly 40 cm in the BIS-2000 sequence, suggests a much greater influence on the stratigraphy that cannot be explained by minor disruptions, like catchment lags. The spread may indicate a volcanically active period towards the end of Pollen Zone IV, beginning at 2337 cm depth, that produced multiple signatures of closely-timed eruptions. Only further geochemical analysis would be able to solidify whether Tephra Peaks F, G, and H originate from distinctly separate eruptions, but instrumental capacity limits this study to six high-resolution analyses and therefore excludes Tephra Peak H.

6.1.3 Tephra Peak E

Tephra Peak E, identified between 2217 cm and 2213 cm, is situated just above a significant sediment input at 2230 cm depth (Figure 5.6; Lauterbach et al. 2024). This peak, containing 61.64 shards/g, is the largest recorded in the BIS-2000 sequence. The discrete tephra horizon is likely the result of a single primary ashfall combined with no post depositional reworking because shards are confined within only one 1-cm sample (Figure 5.2; Davies 2015). Because of this narrow spread, the stratigraphic position of Tephra Peak E can be precisely placed in the 1-cm interval between 2214 cm and 2215 cm depth.

6.1.4 Tephra Peak D

Tephra Peak D lies towards the end of Pollen Zone Vb, and the surrounding samples directly above and below contain zero tephra shards. Because it contains only 7.87 shards/g, it is the smallest tephra peak in the BIS-2000 sequence, narrowly less than the 7.96 shards/g found in Tephra Peak H and just above the threshold of 6.94 shards/g (Figure 4.3; Figure 5.6). While the spread of the tephra suggests little post depositional reworking or other environmental lags, it was not selected for high-resolution analysis on the basis of instrumental limits and in favour of tephra peaks with greater shard concentrations. Its stratigraphic position is therefore limited to the broader 5-cm range between 2188 cm and 2183 cm depth.

6.1.5 Tephra Peak C

Tephra Peak C lies in the middle of Pollen Zone VIa (Figure 5.6). This peak has a tephra concentration of about 11 shards/g. Tephra Peak C lies above a second 5 cm sample that contains 2.6 shards/g. The surrounding samples within the wider 50 cm range in which Tephra Peak C lies have inconsistent shard concentrations, ranging anywhere from 0 to 10 shards/g with no distinct trend or pattern in their changes (Figure 4.3). Because there were no shards found directly above and below the two samples in the Tephra Peak C horizon, however, it will be assumed that these are unrelated events. In the high-resolution analysis of Tephra Peak C, tephra was only found in the two top-most 1-cm intervals between and 2163 cm to 2162 cm (<20 shards/g) and 2162 cm to 2161 cm (13 shards/g; Figure 4.3). As the lower sample has the greater shard concentration, the stratigraphic position of Tephra Peak C can be narrowed to the single 1-cm interval between 2163 and 2162 cm depth.

6.1.6 Tephra peak B

Tephra Peak B displays little evidence for reworking. The 33.53 shard/g peak lies between samples that contain no tephra. From the low resolution sequence, tephra is present between 2113-2108 cm. From the high resolution sequence, tephra is present within three of the five 1-cm samples: between 2108 and 2109 cm (8.02 shards/g), 2109 cm and 2110 (10.71 shards/g), 2110 and 2111 (2.07 shards/g; (Figure 4.3). Because the difference between the first two samples is only a few shards/g, I consider the stratigraphic position of Tephra Peak B to be between 2108 and 2110 cm. The even split between clear and brown shards indicates a mixed tephra source, which can provide further insights into the volcanic activity and environmental conditions at the time of deposition. This detailed stratigraphic information enhances our understanding of the sedimentary sequence and its broader geological context.

Tephra Peak B lies at the beginning of Pollen Zone VIb (Figure 5.6) and the beginning of Unit 4 (Table 3.1), both palynologically and sedimentologically marking the end of temperate conditions (Müller 1974; Lauterbach et al. 2024). The boundary from Pollen Zone VIa to the VIb is largely defined by a significant increase in NAP taxa from 5% in VIa to over 25% in VIb (Lauterbach et al. 2024). The boundary from sediment Unit 3 to Unit 4 was defined by a distinct stop in calcite precipitation, leaving behind only unvarved organic sediments. Calcite precipitation slows as water temperatures cools (Brunskill 1969; Kelts and Hsü 1978), so perhaps the rapid increase of cooler climate taxa with the onset of Pollen Zone VIb towards the very end of the Last Interglacial was responsible for the sudden disappearance of calcite and increased organics in the record. However, because Tephra Peak B was deposited discretely with no tephra in neighbouring samples, the significant and rapid increase of vegetation did not appear to delay tephra wash-in as theorized for Tephra Peaks G and F.

6.1.7 Tephra Peak A

The 5 cm-thick low resolution sample between 2055 and 2050 cm has a shard concentration of 21.4 shards/g, composed of 13.6 clear shards/g and 7.8 brown shards/g. The 5 cm-thick sample just below this has a shard concentration of only 2.8 shards/g. Further below this, the next three 5-cm samples contain no tephra. From the low-resolution shard concentration profile, there is an obvious shard maximum that would serve as a stratigraphic position. In the high resolution analysis there were two consecutive 1-cm thick samples that contained tephra. It must be noted that in the low resolution profile, the maximum shard concentration was found in the very first sample of the studied sequence, between 2050 and 2055 cm. To truly ensure that the maximum

shard concentration, and thus assumed stratigraphic position, is found within this 5 cm range, it would be important to revisit the next few samples upcore that were outside of the range of this study. However, from high resolution analysis of tephra Peak A, shards are not present between 2050 to 2052 cm, so it is unlikely that the maximum would occur in a sample above 2050 cm.

6.2 Classifying the geochemical signature of key tephra horizons

Comparing the shard compositions of the Bispingen tephra with those from other known eruptions could help link the Bispingen deposit to another site with geochemically similar tephra, potentially identifying its eruptive source. Tracing the volcanic source of Bispingen tephra will help define the geographic range over which cryptotephra can travel and subsequently be used as a regional stratigraphic marker across multiple ultra-distal sites. In ideal cases, tephra can be matched to an exact eruption for which its age is precisely known (Lowe 2011). Iceland has the most robust record of Last Interglacial eruptions with which to compare to Bispingen (see Table 2.5; (Sejrup et al. 1989; Sjøholm, Sejrup, and Furnes 1991; Fronval et al. 1998; Wastegård and Rasmussen 2001; Brendryen, Hafliðason, and Sejrup 2010; Abbott et al. 2011; Abbott et al. 2013; Abbott, Austin, and Davies 2014; Davies et al. 2014). Iceland also has the most diverse volcanic activity so even without an exact match, general rock suite and affinities to certain volcanic zones in Iceland may be discernable (Jakobsson 1979). The tephra records selected for comparison come from cores LINK 16 (Abbott, Austin, and Davies 2014) and MD99-2289 (Brendryen, Hafliðason, and Sejrup 2010). LINK 16 lies southwest of Iceland just west of the Faroe Islands, and MD99-2289 lies directly west of Iceland (Figure 2.5). Should any of the Bispingen tephra originate from Iceland, it would have likely been identified in one of these cores first, since tephra is carried west towards continental Northern Europe. Due to the limited number of shards identified and collected for geochemical analysis, all raw data points above 80 wt% are compared to raw data from the Northern Atlantic sites. Any similarities and conclusions drawn between these two datasets shall taken with caution because raw datasets will continue to account for individual biases that are specific to the Bispingen lake record and the North Atlantic marine records. To ensure robust comparisons, only data points exceeding 95 wt% are compared to normalised datasets from other European sites. These data points consist of four rhyolitic shards from Population A of Tephra Peak A. The remaining normalised data points below 95 wt% are nonetheless given in Table 5.3 in Chapter 5.

6.2.1 LINK 16

The first tephra record referenced against the Bispingen record is marine core LINK 16 (Abbott, Austin, and Davies 2014; Figure 2.5). The selected reference layers from LINK 16 extend from 698 cm to 605 cm, covering MIS 5e through MIS 5c. The records are distinctly divided into two geochemical compositions: a tholeiitic affinity with a basaltic composition (yellow, purple, and red shapes; Figure 6.1) and a rhyolitic composition (black open triangles; Figure 6.1). Many of these tephra layers are heterogenous and exhibit multiple geochemical populations. Because Tephra Peak A and Tephra Peak C each contain two tephra populations, neither appear to be homogenous tephra layers. Tephra Peak A contains cluster of rhyolitic leaning shards, but one additional shard with a trachytic-basaltic shard. Tephra Peak C contains two trachy-dacitic shards and one trachytic-basaltic shard. While the LINK 16 tephra layers do not overlap with any Bispingen tephra shards on the TAS plot, there are some overlapping similarities when comparing SiO_2 to individual elemental oxides.

Rhyolitic layers

The rhyolitic layer in LINK 16 (Abbott, Austin, and Davies 2014) from 680-675 cm was composed of several tephra populations, one of which was distinguished as widespread layer d 5e-Midt/RHY (also referred to as 5e-Eem/RHY-I in Brendryen, Hafliðason, and Sejrup 2010). All three rhyolitic populations in the LINK 16 core had at least 71 wt% SiO_2 . Only one Bispingen shard falls above this value at 72.2 wt%. The other remaining shards in Bispingen ranged between 60-70 wt% SiO_2 . There was also very little overlap between the rhyolitic leaning shards from Bispingen and those from LINK 16 when reviewing the SiO_2 vs individual oxide plots. For example, the cluster of shards from Tephra Peak A contains high CaO (>4 wt%) and Na_2O (9.4 wt%), while LINK 16 shards only contained between 0.7 and 1.8 wt% CaO and about 4 wt% Na_2O . In contrast, LINK 16 shards had higher TiO_2 concentrations, exceeding 0.2 wt%, while the Bispingen shards did not even reach 0.1 wt%. However, the both exhibited low FeO concentrations with the Bispingen values below 1 wt% and the LINK 16 values between 2-3 wt%. Because the Bispingen shards contain less than 70 wt% SiO_2 and higher CaO and Na_2O concentrations than the rhyolitic shards found in LINK 16 during MIS 5e, they almost assuredly did not originate from the eruption which produced the widespread Midt/RHY isochron. The normalised data only confirms this assumption as Tephra Peak A shards still contain higher Na_2O concentrations than the LINK 16 layers (Figure 6.2).

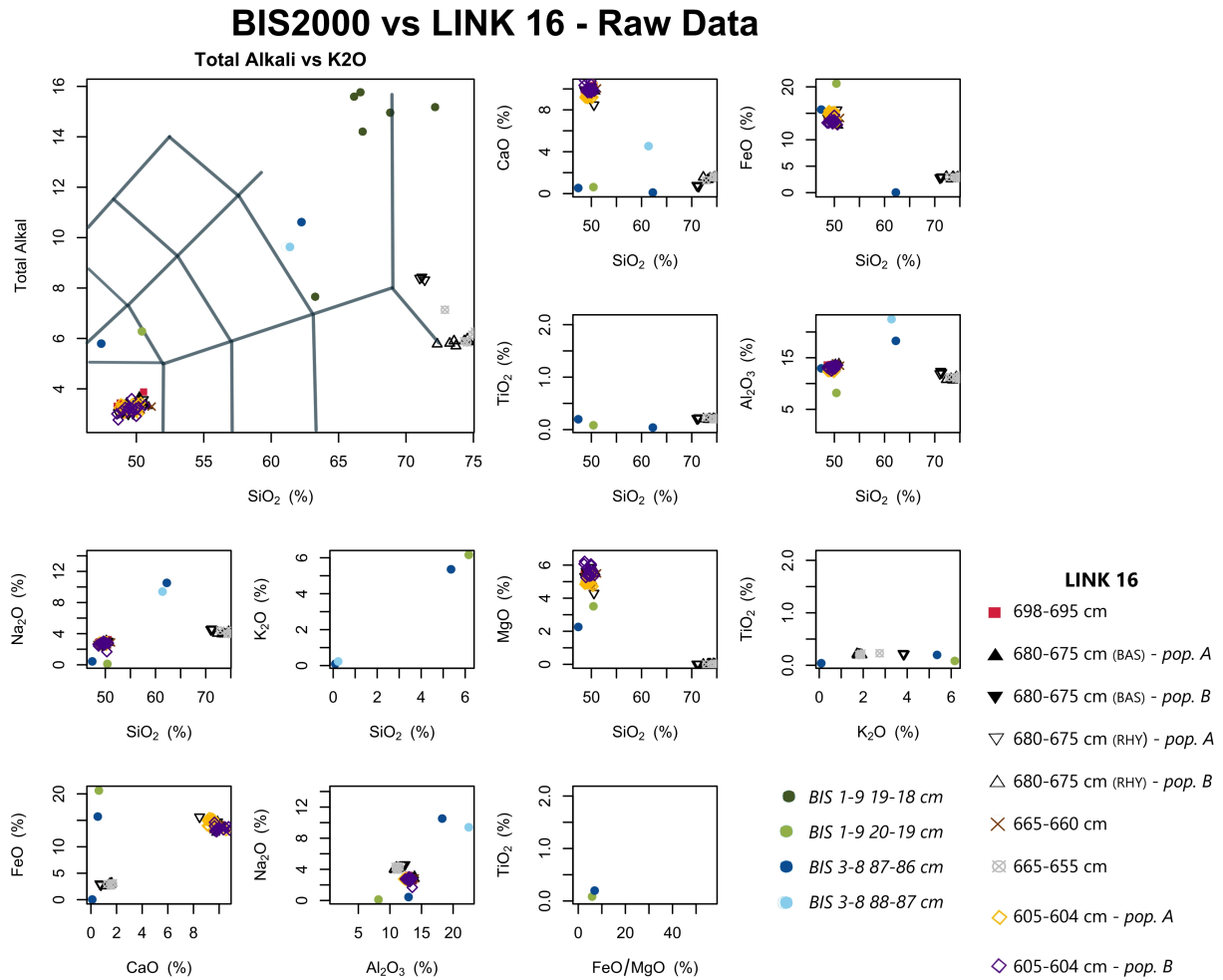


Figure 6.1: Comparing the tephra from BIS-2000 (this study) to tephra populations found in the North Atlantic sequence LINK 16 (Abbott, Austin, and Davies 2014). The data from both studies are presented raw.

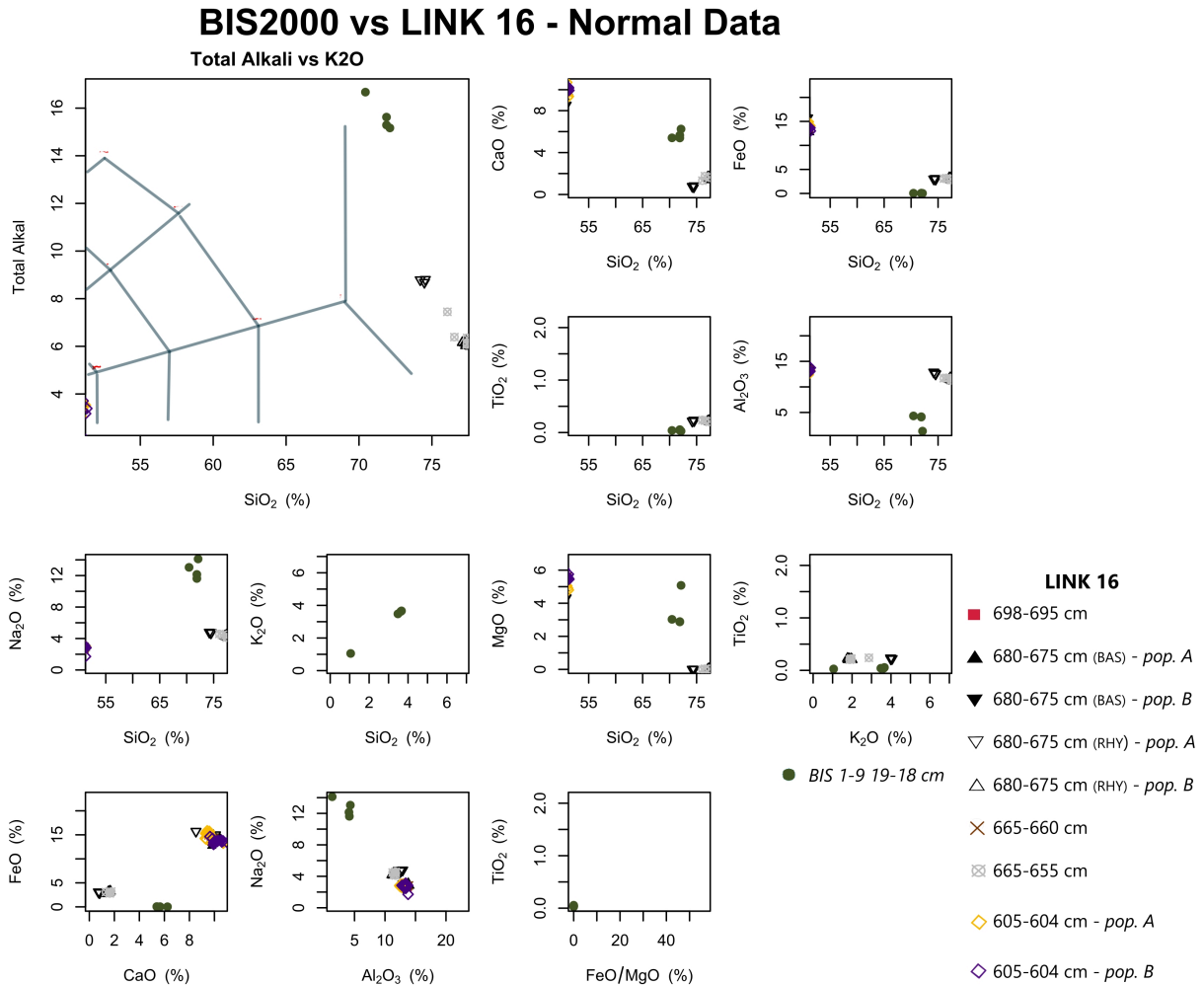


Figure 6.2: Comparing the tephra from BIS-2000 (this study) to tephra populations found in the North Atlantic sequence LINK 16 (Abbott, Austin, and Davies 2014). The data from both studies are presented normalised and only shards with 95 wt% raw are included.

Basaltic Layers

The basaltic layer in LINK 16 (Abbott, Austin, and Davies 2014) from 698-695 cm was determined to be deposited by primary ashfall and subsequently correlated to the known 5e-Low/BAS-IV isochron in ENAM33 and MD95-2009 (Wastegård and Rasmussen 2001; Davies et al. 2014). Its SiO_2 concentration ranged between 49.3 and 50.6 wt% (Abbott, Austin, and Davies 2014). The basaltic layer in LINK 16 from 680 to 675 cm contained two tephra populations and was determined to be a non-isochronous layer deposited by ice-rafting (Abbott, Austin, and Davies 2014). Nevertheless, both populations' SiO_2 concentrations ranged between 48.7 and 50.9 wt% . The next layer in LINK 16 from 665-660 cm exhibited slightly higher SiO_2 concentration upwards of 51 wt%. The two basaltic populations in LINK 16 from 605-604 cm displayed a tholeiitic affinity, ranging between 48.6 and 50.6 wt% SiO_2 , but differed between their TiO_2 concentrations. Because this layer was composed of multiple populations that were traced to multiple volcanic zones in Iceland, it was also determined to be a non-isochronous layer deposited by ice-rafting (Abbott, Austin, and Davies 2014).

The single shard from Population B of Tephra Peak A fell within the overall LINK 16 tholeiitic range of SiO_2 wt% between 48.6 and 51 wt%, and the single shard from Population B of Tephra Peak C fell just outside of this range at 47 wt% SiO_2 (Figure 6.1). The two B populations from Tephra Peaks E and C also expressed fairly similar Na_2O concentrations to the LINK 16 tholeiitic cluster, but the Bispingen tephra has much higher K_2O concentrations (5-6 wt%) compared to the tholeiitic tephra layers that ranged <1 wt% K_2O . The shard from Population B of Tephra Peak C has very similar FeO and Al O , while Population B from Tephra A does not. The shard had 15.7 wt% FeO and was geochemically closest to Population A 605-604 cm, which averaged to 14.8 wt%. The shard also had 12.94 wt% Al_2O_3 and was geochemically closest to LINK 16 Population B 680-675 cm, which averaged to 12.90 wt%.

Icelandic tephra 5e-Low/BAS-IV from 698 to 605 was deposited towards the start of MIS 5e, while Tephra Peak A was identified towards the end of MIS 5e based upon its position within Pollen Zone VIb (Figure 5.6). The Icelandic tephra layer from 605-604 cm was deposited during MIS 5c, well outside the stratigraphic range of this study. While the timing and geochemical profile of this exact eruption does not match Bispingen during the Last Interglacial, the overlap of particular oxides ratios offer insight into possible source volcanic systems. Abbott, Austin, and Davies (2014) attests that the range of tephra between 49 and 50 wt% SiO_2 , 14 wt% FeO, and 10 wt% CaO is strongly characteristic of the Grímsvötn system. The SiO_2 and FeO from Population A of Tephra Peak A show similar characteristics, but contain much less CaO. Therefore,

it appears the Bispingen tephra deviates from the LINK 16 tholeiitic profile because it has high K_2O , low TiO_2 , and low CaO wt% concentrations. Lastly, the normalised data, again, shows no correlation to rhyolitic shards from Tephra Peak A (Figure 6.2).

6.2.2 MD99-2289

Core MD99-2289 is the second Last Interglacial Icelandic tephra record referenced against the Bispingen record (Figure 2.5; Brendryen, Hafliðason, and Sejrup 2010). The selected reference record includes widespread tephra layers from MIS 5e and MIS 5d (Figure 6.3). 5e-EemTAB-I refers to a widespread basaltic layer dated to 124.4 ka, and 5e-Eem/RHY-I refers to a rhyolitic layer with two populations, one of which is correlated to 5e-Midt/RHY (Figure 6.1; Brendryen, Hafliðason, and Sejrup 2010; Abbott, Austin, and Davies 2014). At the transition between MIS 5e to MIS 5d, there was a tephra layer with seven mixed populations, referred to as 1855.5 a-f because of its position between 1856-1855 cm in the core (6.3). This layer was separated into a second figure because it contained seven different populations, and it was easier to distinguish between data points this way (Figure 6.5). Lastly, 5d-DO26sTRACHY-I refers to a widespread layer from MIS 5d, that although is outside the temporal range of this study, provides an example of what an isochronous layer of a trachytic origin may look like.

Rhyolitic Layers

The first rhyolitic layer in the MD99-2289 sequence in Figure 6.5 was composed of one rhyolitic isochronous and a secondary basaltic tephra population. In the primary rhyolitic isochron, there is a large spread of SiO_2 values, ranging from 61.4 to 77.3 wt% . The other individual oxide compositions are less variable. Total alkali is about 5-6 wt%, with Na_2O ranging from 3.9 to 4.8 wt% and K_2O ranging from 1.6 to 1.9 wt%. From the MD99-2289 sample between 1856 to 1855 cm depth in Figure 6.5, 1888.5 - c was the only distinct rhyolitic population, with an SiO_2 concentration around 73.5 wt% and a total alkali concentration around 5 wt%. The total alkali concentrations of the MD99-2289 rhyolitic tephra populations in Figure 6.5 are too low to overlap with population A of Tephra Peak A. Population A from 5e-Eem/RHY-I, however, did show some similarities with the one shard from Population A of Tephra Peak A that was outside of the five-shard cluster. The Bispingen shard has an NaO concentration of 63.3 wt%, a CaO concentration of 0.5 wt%, a FeO concentration of 0.5 wt% , and an Al_2O_3 concentration of 10.5 wt%. In 5e-Eem/RHY Population A, there is one shard that has an NaO concentration of 61.4 wt%, a CaO concentration of 1.4 wt%, a FeO concentration of 2.5 wt% , and an Al_2O_3 concentration of 9.1

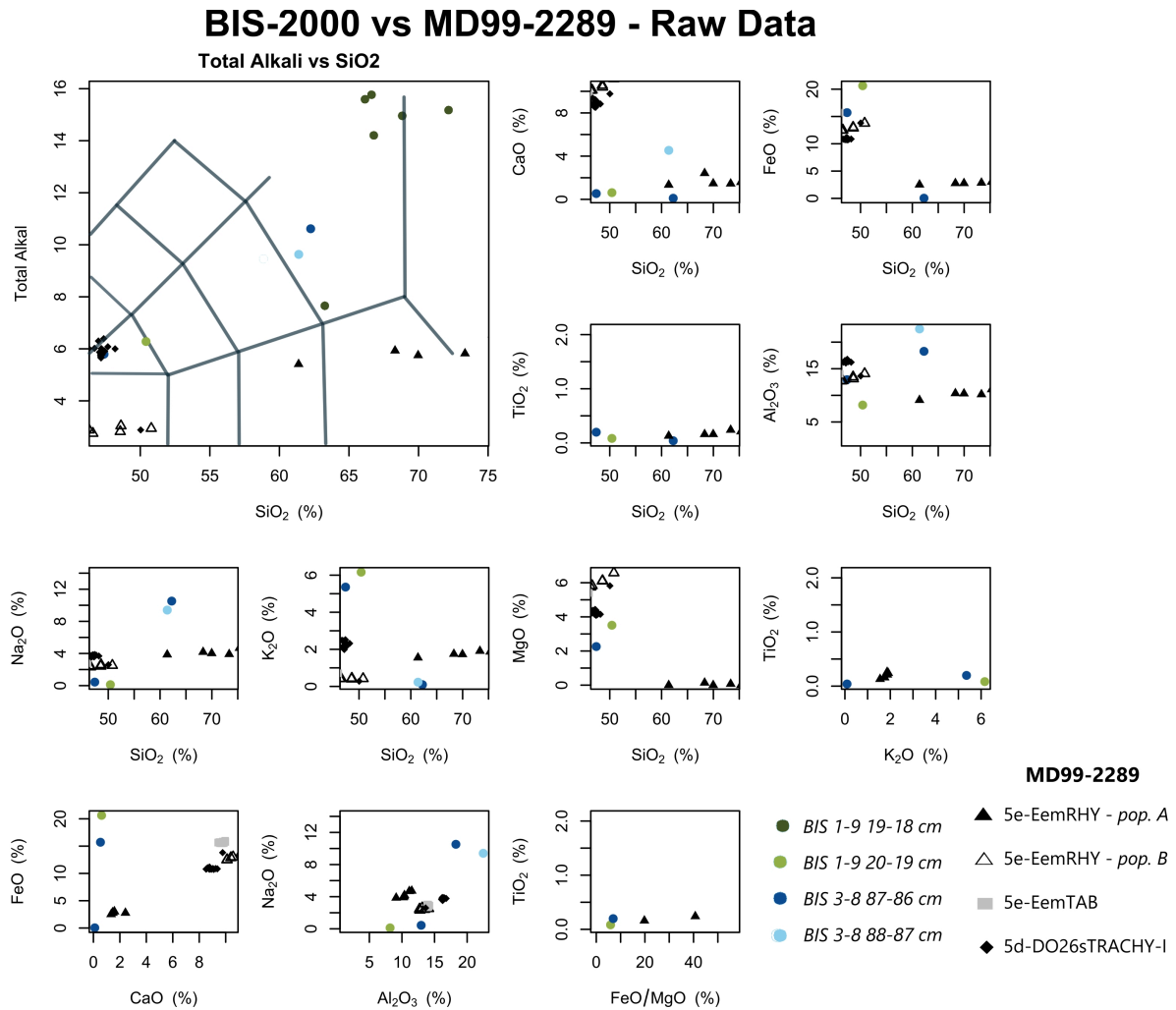


Figure 6.3: Comparing the tephra from BIS-2000 (this study) to tephra populations found in the North Atlantic sequence MD99-2289 (Brendryen, Hafliðason, and Sejrup 2010). The data from both studies are presented raw.

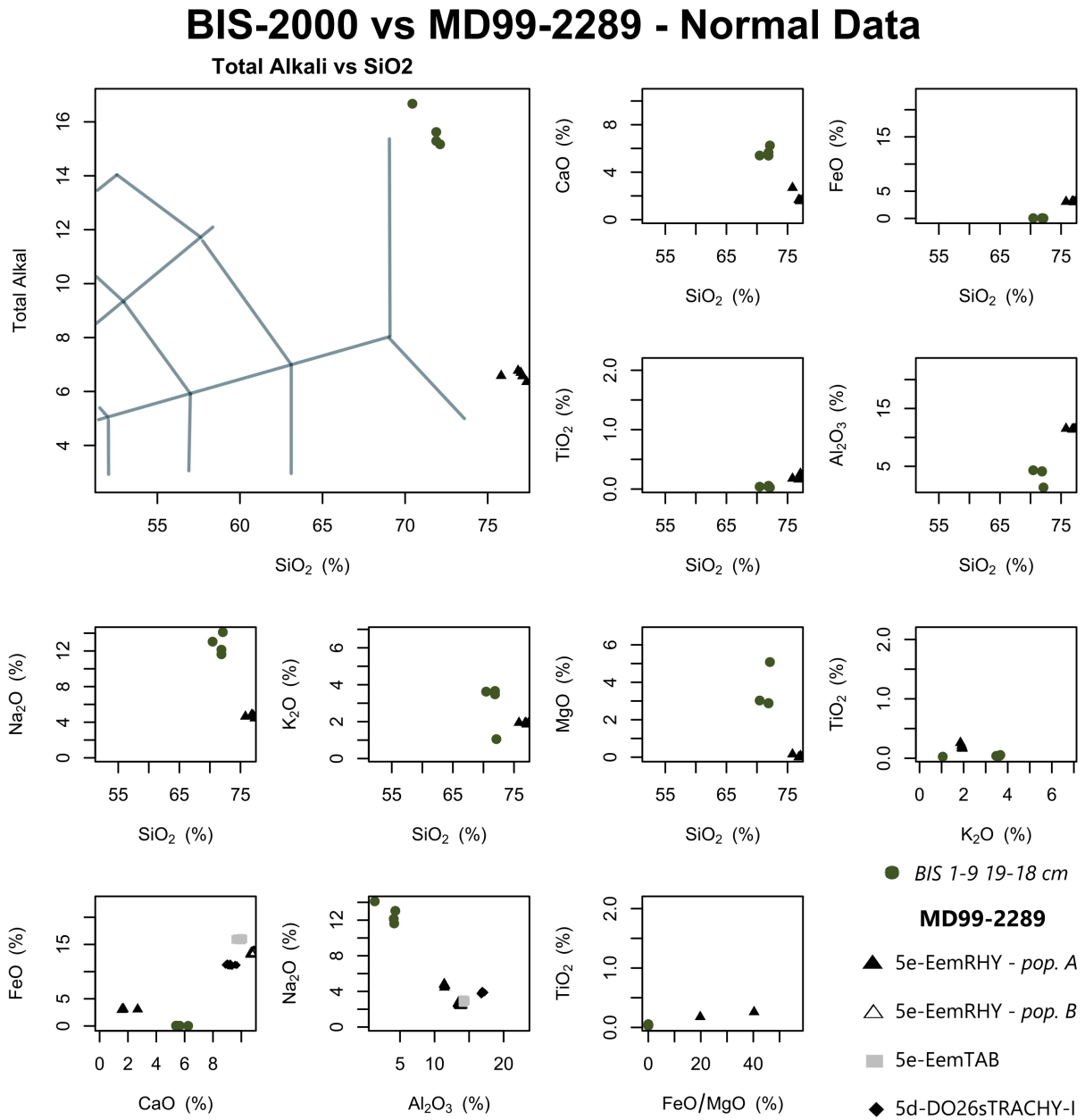


Figure 6.4: Comparing the tephra from BIS-2000 (this study) to tephra populations found in the North Atlantic sequence MD99-2289 (Brendryen, Hafidason, and Sejrup 2010). The data from both studies are presented normalised and only shards with 95 wt% raw are included.

wt%. The normalised Tephra Peak A shards contain higher Na₂O and lower SiO₂ concentrations than the MD99-2289 shards suggesting that they are not geochemically compatible (Figures 6.4 and 6.6).

Trachytic layers

There are three different tephra populations in the MD2299-89 record that offer intermediate SiO₂, intermediate total alkali values, and therefore fall more under a trachytic composition instead of rhyolitic or basaltic. The first two are populations A and B in Figure 6.5. Population A was a cluster of nine shards, slightly more andesitic than both Bispingen Populations B of Tephra Peaks A and Population B of Tephra Peak C. Population A in MD2299-89 (Figure 6.5) is characterized by high CaO (6%), high TiO₂ (>2%), and high Al₂O₃ (>17%). Population B in MD2299-89 is a single shard with a composition close to Bispingen Population A of Tephra Peak C in regards to SiO₂ and aluminium. The shard has a SiO₂ concentration of 58.2 wt% and Al₂O₃ concentration of 18.8 wt%, compared to one of the shards from Population A of Tephra Peak C with a SiO₂ concentration of 62.3 wt% and Al₂O₃ concentration of 18.3 wt%. The final trachytic layer is dated to 116.7 ka in MIS 5d (Brendryen, Hafliðason, and Sejrup 2010). The primary population from this layer is clustered towards one end of the trachy basaltic classification (Figure 6.5). It is defined by 46.3 to 48.2 wt% SiO₂ and an average total alkali of 5.96 wt%. Population B of Tephra Peak C has an SiO₂ concentration of 47 wt% and total alkali of 5.8 wt%. The two populations from the final trachytic layer in MD2299-89 all share fairly high FeO and Al₂O₃. 5d-DO6s/TRACHY-I has an FeO concentration of about 10.9 wt% and an average Al₂O₃ concentration of 16.3 wt%, and Population B of Tephra Peak C has an FeO concentration of 15.7 wt% and an Al₂O₃ concentration of 13.0 wt%. However, Population B from Tephra Peak C exhibits much lower CaO and TiO₂ concentrations.

Basaltic layers

Lastly, there were also a number of basaltic populations in the Iceland MD2299-89 dataset such as smaller secondary deposits in 5e-Eem/RHY-I and a single shard from 5d-DO6s/TRACHY-1. MD99-2289 Populations D, E, F in the sample from 1856-1855 cm depth also fell towards a more basaltic classification with low SiO₂ concentrations and low total alkali concentrations. Shards from population B of 5e-Eem/RHY-I have an Al₂O₃ concentration between 12.7 and 14.1 wt% and an FeO concentration between 12.5 and 13.8 wt%. Shards from Population D in the sample from 1856-1855 cm depth has an Al₂O₃ concentration between 12.9 and 13 wt% and an FeO concentration between 13.8 and 15.4 wt%. The shard from Population B of Tephra Peak

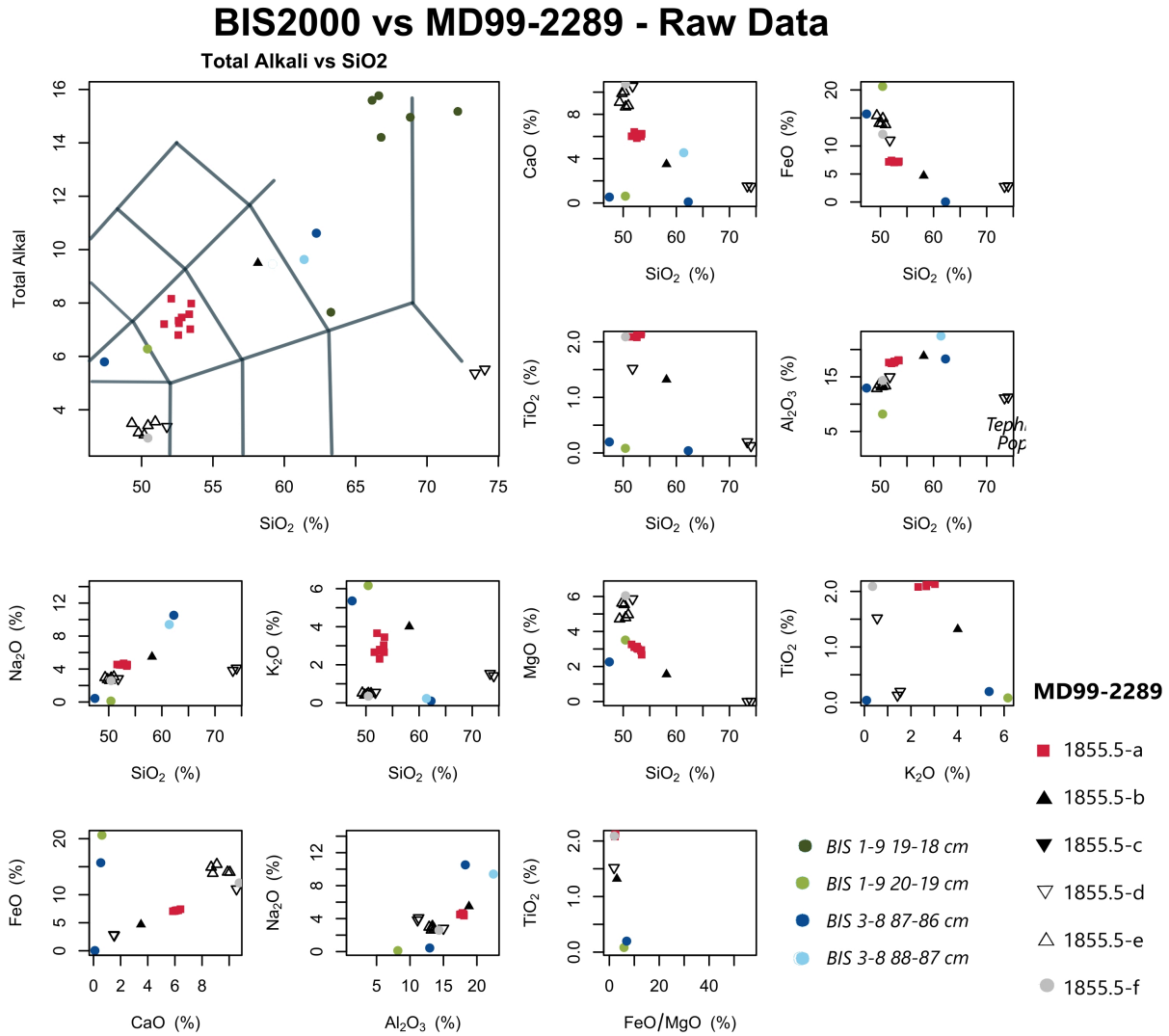


Figure 6.5: Comparison of the tephra from BIS-2000 (this study) to tephra populations found in the North Atlantic sequence MD99-2289 (Brendryen, Hafliðason, and Sejrup 2010). Because one layer between 1856 to 1855 cm contained seven different populations, it is presented on a separate figure. Brendryen, Hafliðason, and Sejrup 2010 originally refers to this layer as 1855.5 a-f, with each letter denoting a distinct population. The same naming is used in the key found in the top right corner of the figure. The data from both studies are presented raw.

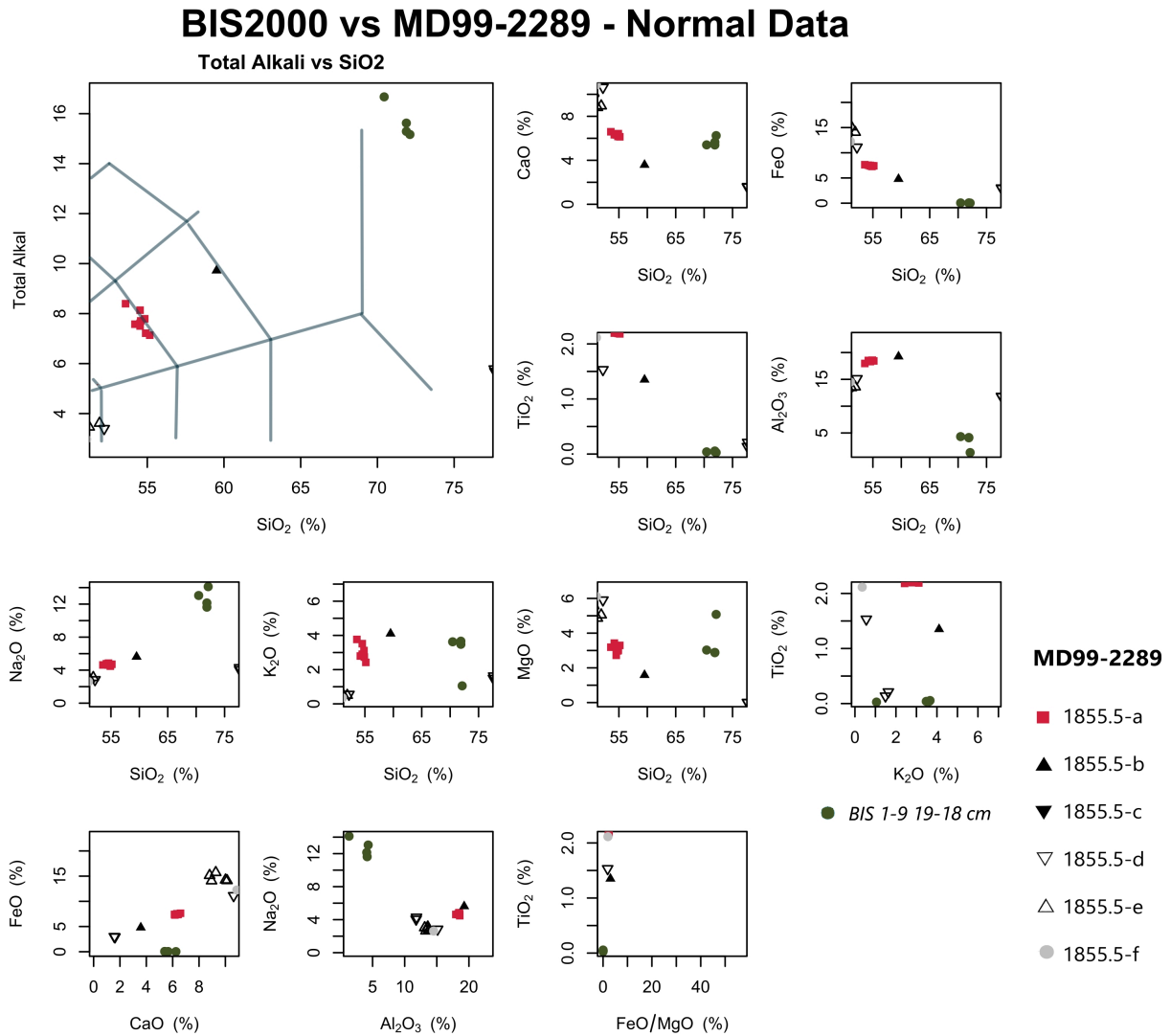


Figure 6.6: Comparison of the tephra from BIS-2000 (this study) to tephra populations found in the North Atlantic sequence MD99-2289 (Brendryen, Hafidason, and Sejrup 2010). Because one layer between 1856 to 1855 cm contained seven different populations, it is presented on a separate figure. Brendryen, Hafidason, and Sejrup 2010 originally refers to this layer as 1855.5 a-f, with each letter denoting a distinct population. The same naming is used in the key found in the top right corner of the figure. The data from both studies are presented normalised and only shards with 95 wt% raw are included.

C had an Al_2O_3 concentration of 13 wt% and a FeO concentration of 15.7 wt%. In general this shard aligns well with basaltic signatures in regards to SiO_2 , Al₂, and FeO, but remains variable for other oxides, like CaO and K_2O .

6.2.3 Volcanic zones and the possible origins of Bispingen tephra

Comparing Icelandic tephra provenances

As highlighted by Brendryen, Hafliðason, and Sejrup (2010), tephra geochemistries are often compared to known data of modern Icelandic volcanoes, but Icelandic Volcanic systems are rarely stationary over time and certain signatures may shift over time to resemble geochemically similar volcanic zones in other parts of Iceland. Jakobsson (1979) classifies Icelandic volcanic zones into three distinct groups: tholeiitic basalts, transitional alkali (high Fe–Ti) basalts, and alkali olivine basalts. Tephra populations associated with Grímsvötn and Veidivötn eruptions tend to be classified as tholeiitic, while those from Hekla and Katla lean towards transitional alkali basaltic affinities (Jakobsson 1979; Brendryen, Hafliðason, and Sejrup 2010). Tephra Peak A contains cluster of rhyolite leaning shards, but one additional shards with a trachytic-basaltic shard. Tephra Peak C contains two trachy-dacitic shards and one trachytic-basaltic shard.

5e-Eem/RHY-I and 5e-Midt/RHY are consider comparative isochronous layers that were deposited around the climate optimum, with shards being present further upcore in Population C at depth 1855.5 cm (Brendryen, Hafliðason, and Sejrup 2010). Because all of these Icelandic tephra compositions exhibit much lower Na_2O wt% than Population A of Tephra Peak C, Bispingen Tephra Peak C and 5e-Eem/RHY-I are assumed to be geochemically distinctly different from each other. 5e-Eem/TAB-1 is distinguishable by its very high SiO_2 and FeO content and low SiO_2 . While Population B of Tephra Peak C exhibits low SiO_2 (<50 wt%) and high FeO (>15%), it does not have the high TiO_2 characteristic of Katla volcanism, for which Brendryen, Hafliðason, and Sejrup (2010) suggests could be transported to regions south of Iceland much easier than other volcanic zones and therefore offer a greater opportunity for locating isochronous distal tephra deposits.

Because Bispingen tephra does not match any of the known Icelandic eruptions from Katla or Grímsvöth during MIS 5e, it is justified to compare the data from this study to more recent Icelandic tephra deposits associated with other volcanic zones. A study by Navrátil et al. (2013) geochemically characterized the 2010 Eyjafjallajökull eruption using proximal ash samples collected near the volcano in Iceland and ultra-distal dust deposits collected in Prague. Bispingen tephra can be compared to the Eyjafjallajökull volcano, which is not documented during MIS 5e,

BIS2000 vs Eyjafjallajökull 2010 Eruption - Raw Data

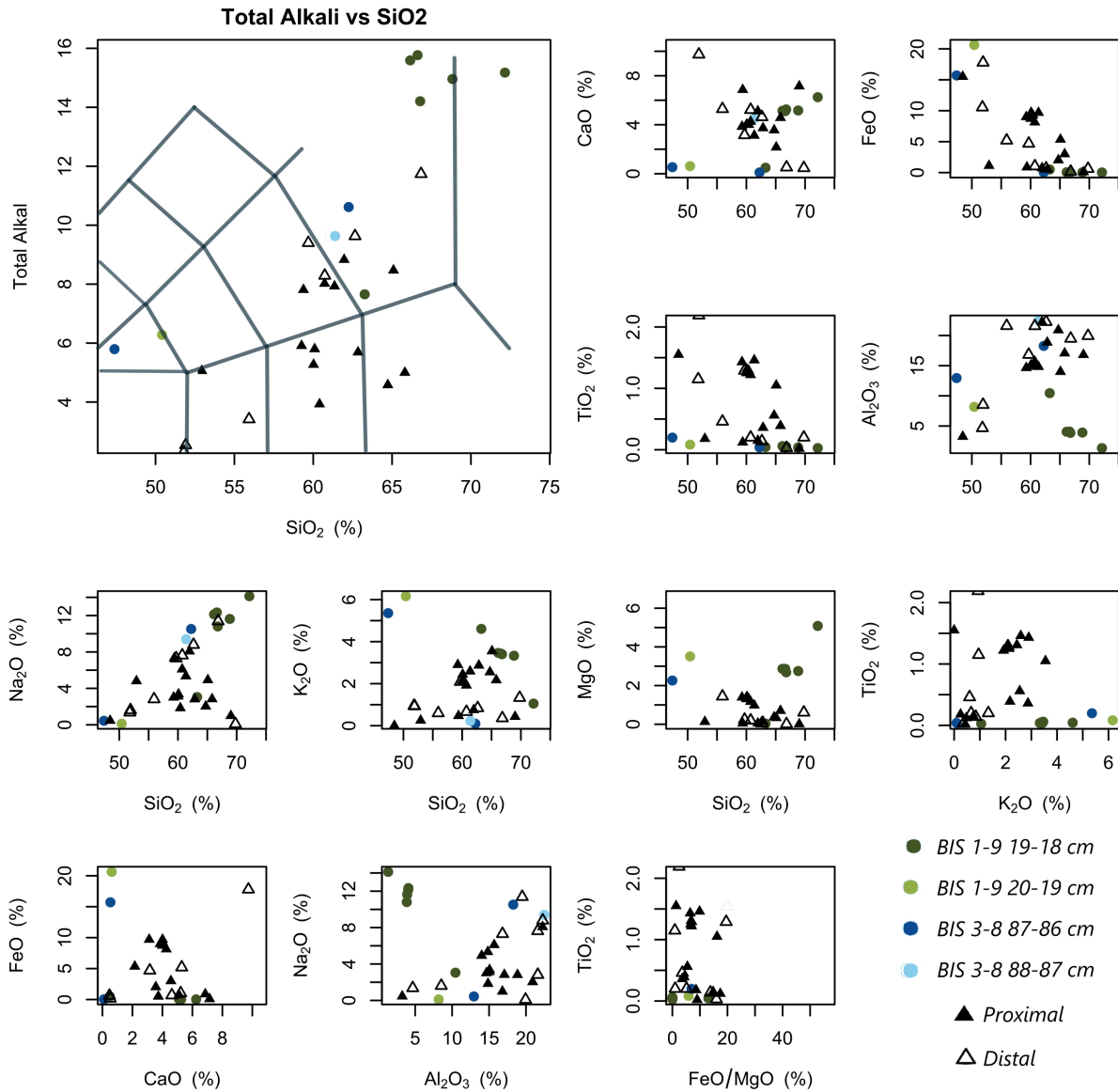


Figure 6.7: Comparing the tephra from BIS-2000 (this study) to tephra proximal to the 2010 Eyjafjallajökull eruption in Iceland and to ultra-distal ash from the same eruption collected in Prague (Navratil et al. 2013). The data from both studies are presented raw.

BIS2000 vs Eyjafjallajökull 2010 Eruption - Normal Data

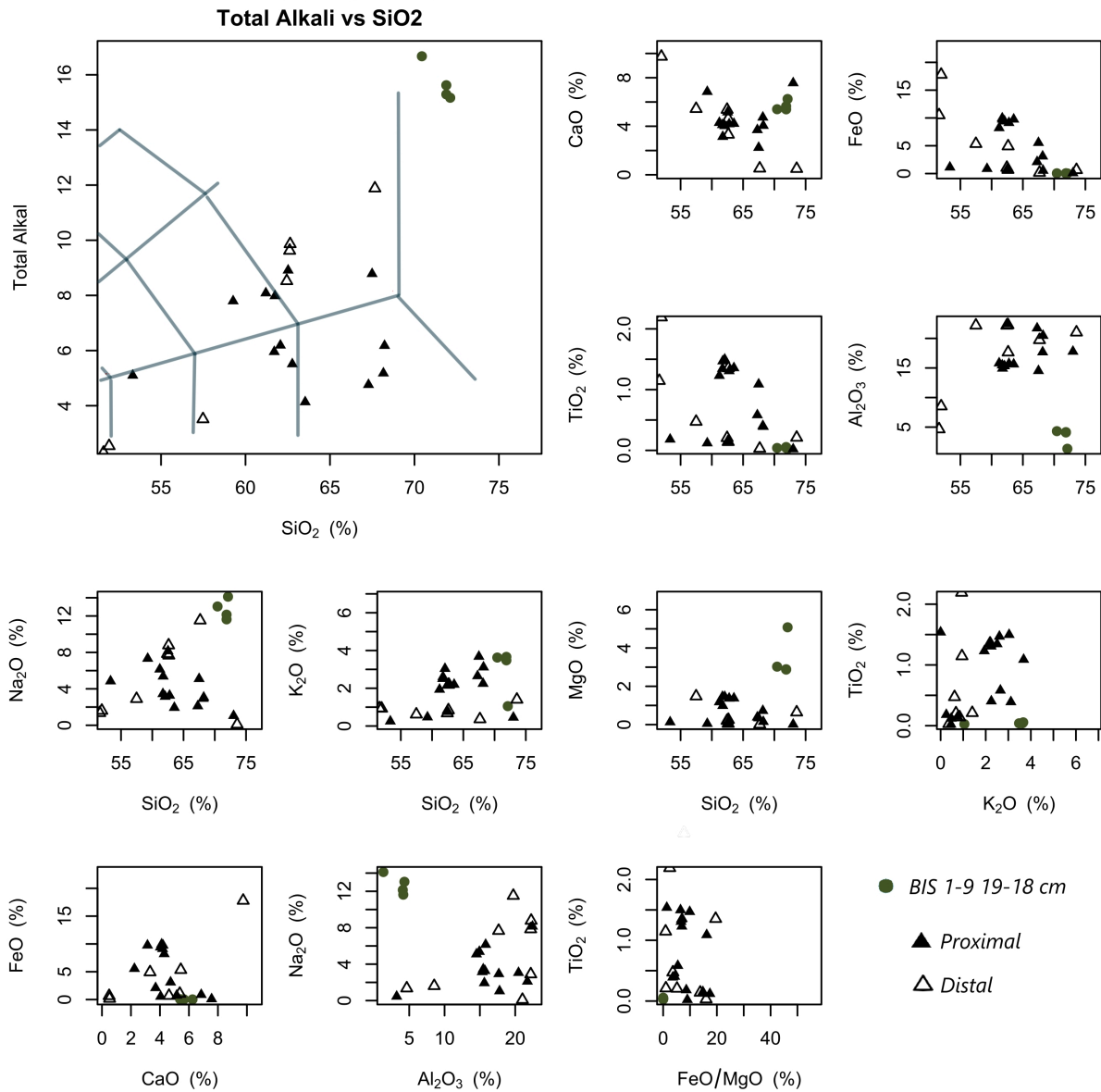


Figure 6.8: Comparing the tephra from BIS-2000 (this study) to tephra proximal to the 2010 Eyjafjallajökull eruption in Iceland and to ultra-distal ash from the same eruption collected in Prague (Navratil et al. 2013). The data from both studies are presented normalised and only shards with 95 wt% raw are included.

Concentration-Extent maps (mg m^{-3})

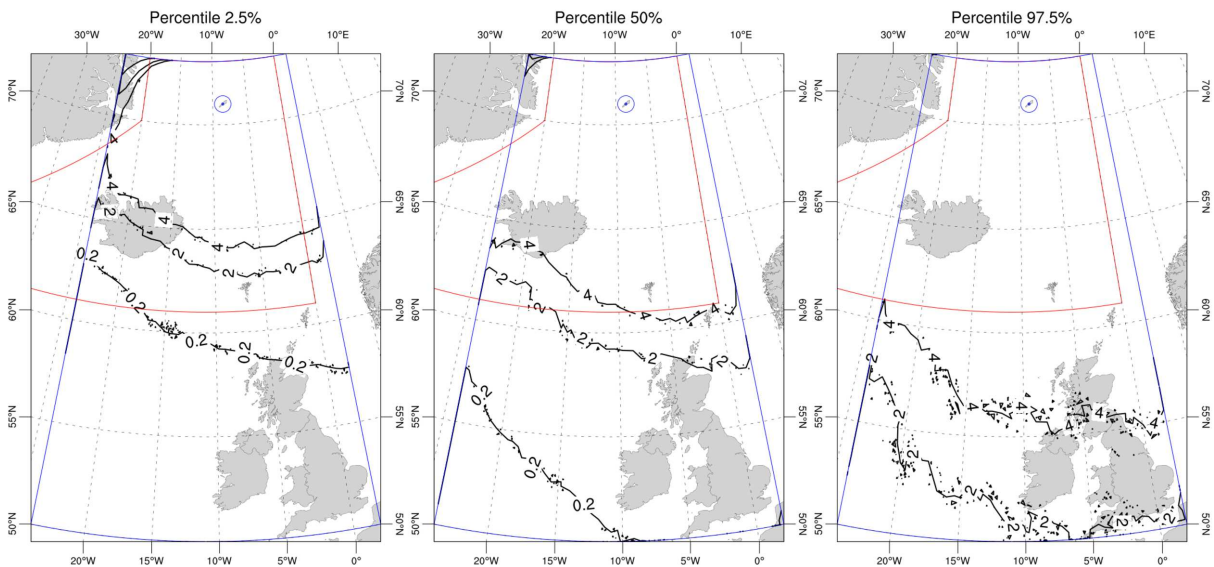


Figure 6.9: From Titos et al. 2021 Figure 12: Concentration hazard map (Medium): relative epistemic uncertainties related with airborne ash cloud concentrations above 0.2 mg/m³, 2 mg/m³ and 4 mg/m³ and extent at 5000 feet (or 1.5 km). Each map corresponds to a different level of confidence, produced by cutting the hazard curves at different percentiles.

by examining its ultra-distal deposits located roughly 500 km southeast of Bispingen in Prague (Navratil et al. 2013). The ash from the 2010 Eyjafjallajökull eruption shows a greater degree of geochemical variability compared to tephra horizons from LINK 16 (Figure 6.1; Abbott, Austin, and Davies 2014) and MD99-29 (Figures 6.3 and 6.5; Brendryen, Haffidason, and Sejrup 2010). Nonetheless, on the TAS plot in Figure 6.7, the distal tephra in Prague had slightly higher total alkali values than the proximal tephra, and aligned with the trachy-dacitic composition of Tephra Peak C Population A. In all of the bivariate oxide plots except for TiO_2 vs SiO_2 , at least one of the two shards, if not both, were found within the bounds of the Eyjafjallajökull tephra (Figure 6.7). The normalised data offers a few similarities with Population A of Tephra Peak A in oxides such as FeO and CaO, but the Bispingen Population still has unusually higher total alkali concentrations (Figure 6.8). While the modern eruption is not directly linked to the Last Interglacial, it offers obvious geochemical similarities none of which could be made with the known MIS 5e eruptions. Furthermore, as instantaneous airfall deposits from Eyjafjallajökull can travel to areas near Central Europe (Figure 6.10), there is great possibility for a similar eruption to transport tephra to Bispingen.

Comparing other tephra provenances

While Population A of Tephra Peak C may align with Eyjafjallajökull, this section considers that some Bispingen tephra may be associated with either an unknown eruption or one from other volcanic provenances. In fact, recent studies suggest that nearly a quarter of all tephra in Northwestern Europe comes from a volcanic provenance other than Iceland (Plunkett and Pilcher 2018).

Because Population B of Tephra Peak A and Population B of tephra Peak C each only contain one shard, determining their exact volcanic sources is difficult with just this limited data alone. While Population B of both Tephra Peak A and Tephra Peak C had similar SiO₂, FeO, and Al₂O₃ wt% concentrations to the basaltic layers found in Icelandic LINK 16 and MD99-2289, the TAS ratio of the Tephra Peak C shard aligned closer to the trachytic-basaltic composition of 5d-DO6s/TRACHY-I, linked to Jan Mayen Volcanic Province. To date, there are no eruptions with the trachy-basaltic signature of Jan Mayen recorded during MIS 5e, but Brendryen, Hafliðason, and Sejrup (2010) notes that while Grímsvötn is the predominant volcanic system in the MD99-2289 record, Jan Mayen activity peaks during MIS 5d and MIS 5e between 109 to 130 ka. MD99-2289 is the only North Atlantic record so far to identify the major tephra layer from 5d-DO6s/TRACHY-I likely because Jan Mayen lies 600 km north of Iceland (Titos et al. 2021) and many of the well-studied cores in the North Atlantic (i.e ENAM33 [Wastegård and Rasmussen 2001], HM57-7 [Sejrup et al. 1989], MD04-2822 [Abbott et al. 2013]; see Figure 2.5).

Ash dispersal from Jan Mayen shows a greater degree of seasonality for large eruption columns between 15 to 20 km (Lacasse 2001; Gjerløw, Hafliðason, and Pedersen 2016). Eruptions during summer months carry ash southwest, in the direction of Iceland and proximal marine cores, but the median wind speed also decreases during these months to <10 m/s (Gjerløw, Hafliðason, and Pedersen 2016). From a study assessing the impact of Jan Mayen eruptions on flight travel, model simulations suggest that medium-sized eruptions could reach the United Kingdom at 5000 feet, with concentrations up to 2 mg/m³ and that large-sized eruptions could reach the United Kingdom and Northern Europe at 25000 feet, with concentrations up to 0.2 mg/m³ (Figure 6.9; Titos et al. 2021;). Ash from large Jan Mayen eruptions can reach the Faroe Islands within 48 hours, so a primary airfall deposit would likely only take days to reach continental Europe (Figure 6.10; Navratil et al. 2013; Titos et al. 2021). In general, the trachy-basaltic composition of Tephra Peak C Population B, as shown only in the TAS plot of 6.3 is roughly consistent with Jan Mayen Volcanic Province, which although has not been recorded in any other Last Interglacial records in the North Atlantic, still has the power to carry ash towards Northern

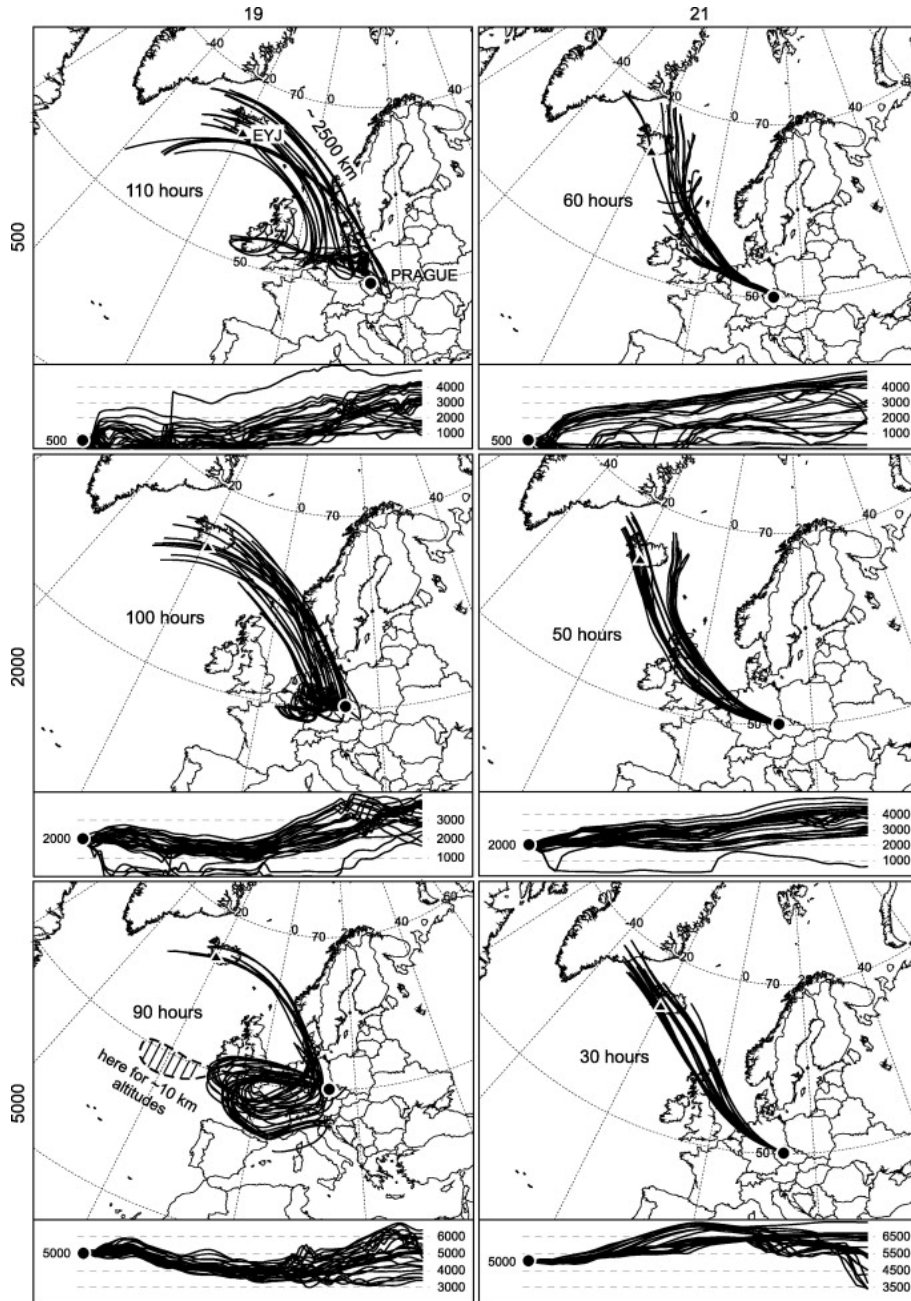


Figure 6.10: Model-simulated trajectories of air masses created to reflect the transport of volcanic ash and dust from Eyjafjallajökull, Iceland to Prague after the 2010 eruption (Source: Navratil et al. 2013; Figure 1).

BIS2000 vs Italian Tephra (Lake Monticchio) - Raw Data

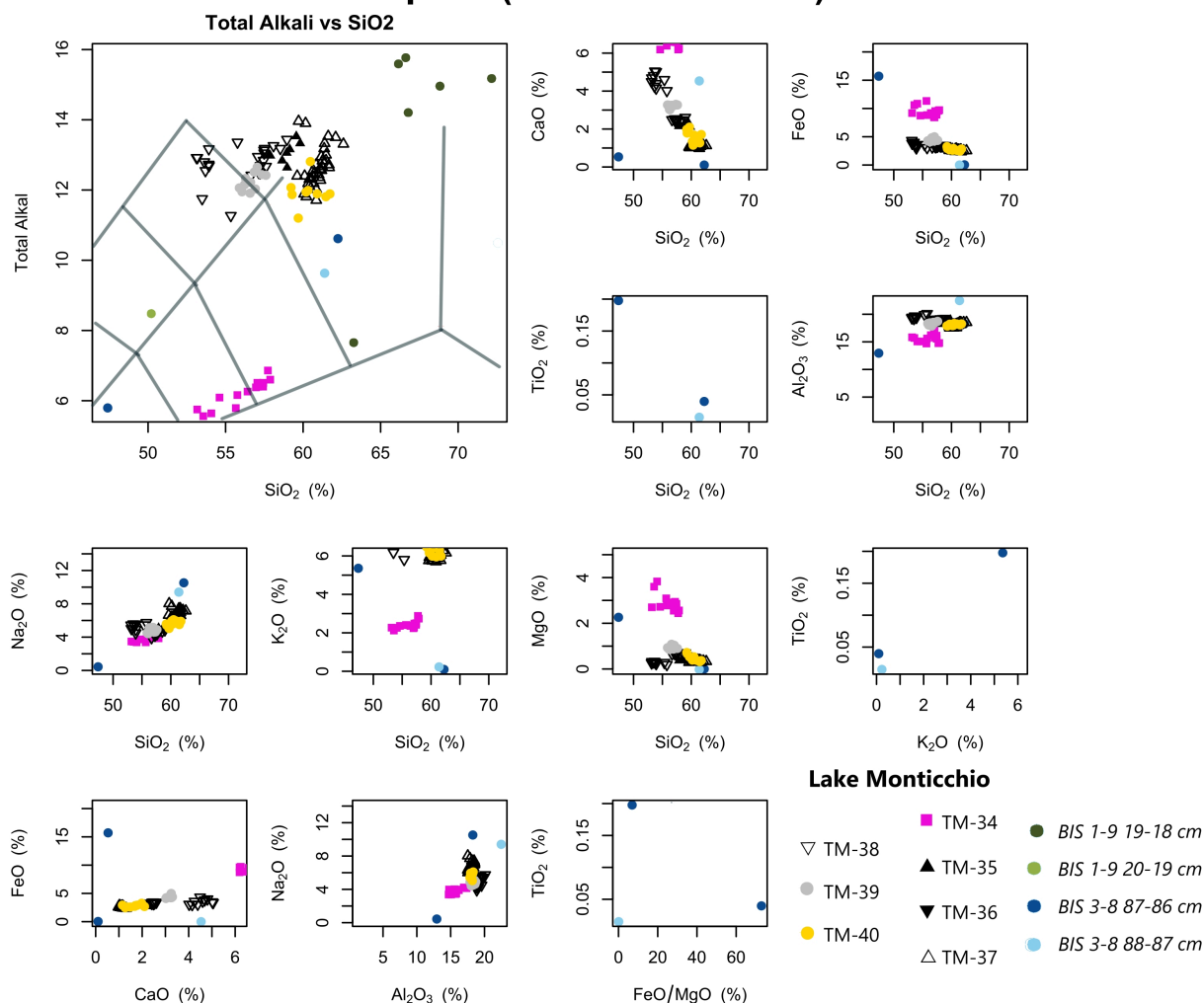


Figure 6.11: Comparing the tephra from BIS-2000 (this study) to tephra layers found in Lake Monticchio, Italy, that are all linked to Italian eruptions during MIS 5e between 130 ka and 118 ka (Wulf et al. 2012). The data from both studies are presented raw.

Europe within days (Gjerløw, Hafliðason, and Pedersen 2016). In rare cases, Jan Mayen eruptions may produce more trachy-andesitic tephra with higher SiO₂ wt% concentrations that could align with Tephra Peak C Population A, but such uncommon occurrences without comparable records are hard to precisely correlate (Gjerløw, Hafliðason, and Pedersen 2016).

It is possible for tephra from Southern European volcanoes to be found in the Bisingen sedimentary sequence. Numerous tephra layers have already been found in the annually varved lake sediments of Lake Monticchio in Southern Italy, all linked to Italian eruptions between 130 ka to 115 ka, roughly synonymous with the length of MIS 5e and the Last Interglacial (Table 2.8; Shackleton et al. 2003; Wulf et al. 2012). The intermediate SiO₂, high (>20 wt%) Al₂O₃, high Na₂O (>8 wt%) and lower FeO and MgO concentrations of Tephra Peak C Population A are somewhat consistent with the trachytic populations of these Italian tephras. While there are

BIS2000 vs Italian Tephra (Lake Monticchio) - Normal Data

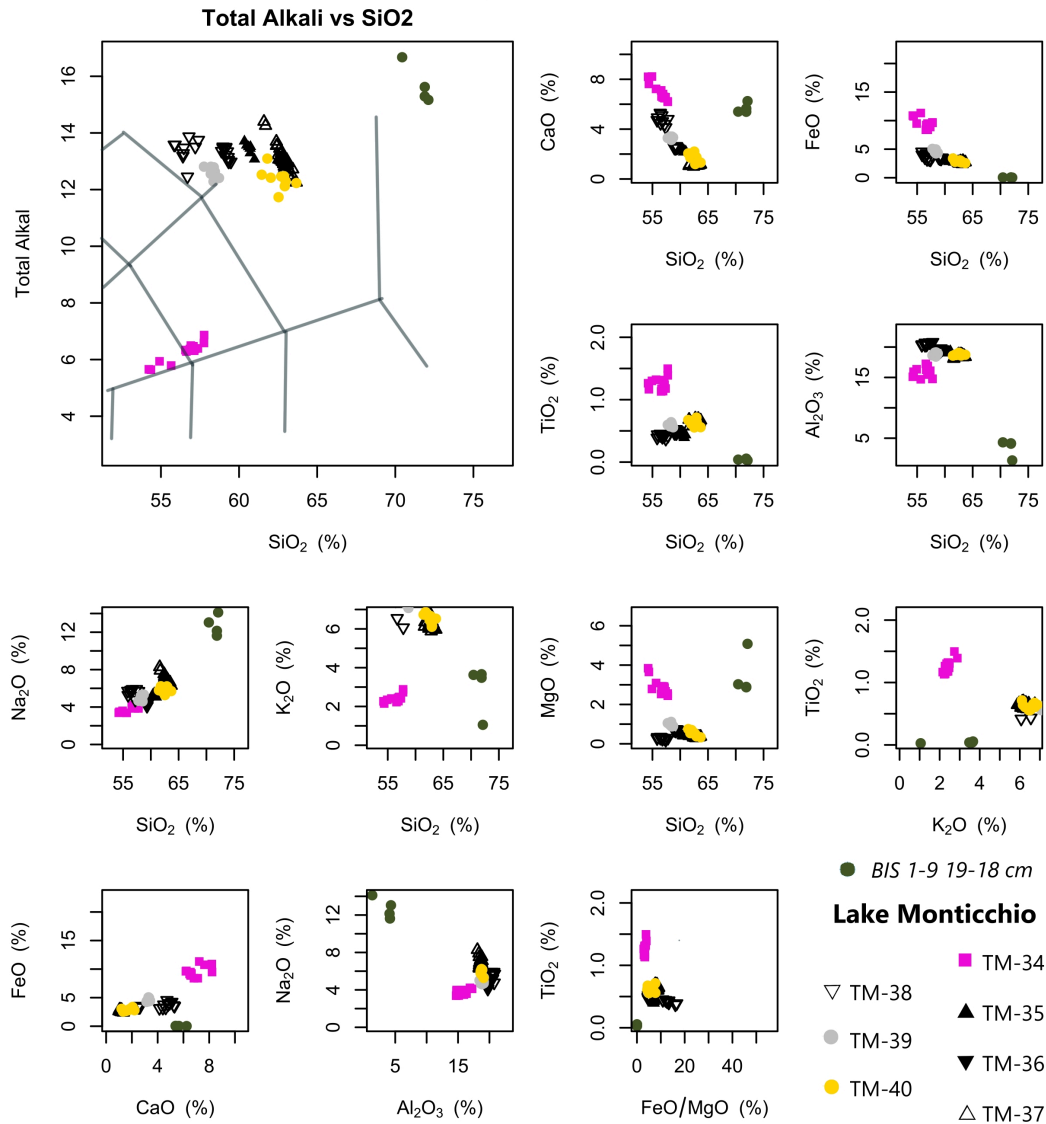


Figure 6.12: Comparing the tephra from BIS-2000 (this study) to tephra layers found in Lake Monticchio, Italy, that are all linked to Italian eruptions during MIS 5e between 130 ka and 118 ka (Wulf et al. 2012). The data from both studies are presented normalised and only shards with 95 wt% raw are included.

no clear and obvious overlaps between the two sites, Tephra Peak C Population generally aligns best with records TM-40 (130.9 ± 6.5 ka) and TM-34 (124.5 ± 6.2 ka) (Figure 6.11; Wulf et al. 2012). Out of all tephra populations from Figure 6.11, TM-40 and TM-34 are the only two traced to Ischia Island. Focusing on all the individual tephra populations traced to Ischia during MIS 5e, including TM-40, TM-37, and TM-33 (c. 118-115 ka), there is still no direct link between Bispingen tephra and Lake Monticchio Ischia tephra, only close similarities (Figure 6.11; Wulf et al. 2012). Should any of the Ischia eruptions be linked to Bispingen Tephra Peak C Population A, it is unlikely to be TM-40 or TM-33-1c because Tephra Peak C occurs during PAZ VIa, and these two layers are found at the very beginning and very end of the Interglacial (Figure 5.6). While high (>20 wt%) Al_2O_3 and high Na_2O (>8 wt%) do provide a strong case for Ischia a possible volcanic source, Al_2O_3 and Na_2O oxides measured in Tephra Peak C Population A also align with Eyjafjallajökull geochemical signatures (Figure 6.7). However, Ischia tephra originates from known eruptions during MIS 5e, while there are still no known recorded Eyjafjallajökull eruptions during this time (Table 2.5).

Although tephra from Azores has been found in Ireland, its general trachytic composition is hard to distinguish between eruptive sources and there is presently not enough Last Interglacial cryptotephra data available with which to draw reliable comparisons (Wastegård, Johansson, and Pacheco 2020). Records of Massif Central volcanism primary come from proximal igneous rock data, which do not offer as reliable comparison to the distal cryptotephra shards in this study (Table 2.7). Likewise, there are few recorded eruption through the entire MIS 5 that are traced to Eiffel Volcanic Zones (Table 2.6), so robust comparisons to the other Volcanic Zones in Chapter 2 are limited during this stage of research.

6.3 Evaluating the potential use of tephra horizons to further Last Interglacial chronology in Northern Europe

Because this study is the first of its kind and to date the only known record of tephra in Northwest Europe during the Last Interglacial, the ability of Bispingen tephra to be compared to other sites is the founding principle guiding this research. This section assesses the vertical variability and shard concentration of the eight major tephra peaks addressed in Chapter 5 to determine their strength as potential chronostratigraphic markers in the Bispingen record. It also suggests regional and local palaeoenvironmental factors that may have influenced how tephra was transported and preserved in the record.

6.3.1 Tephra horizons with weak chronostratigraphic potential

Weak tephra horizons are defined here as those whose sedimentary and characteristics suggest they hold little potential to become a robust a chronostratigraphic marker. Although greater vegetation density is a plausible factor for the downcore spread of tephra shards below Tephra Peak F, the extensive range over 40 cm is still unexplained. In fact, it is likely that this stretch of tephra may be attributed to multiple tephra deposits from changing wind conditions across the phases of one eruption (Watson et al. 2016), or even multiple closely timed eruptions (Davies 2015). Regardless of whether Tephra Peaks G and F are a homogenous mix of multiple eruptive events or one anomalously reworked event, it is still unclear whether the maximum shard concentration is a delayed signal or from primary ashfall. As the power of tephrostratigraphy relies on a precise timing that can be transferred between sequences containing the same ash layer, misinterpreting the stratigraphic position will compromise its integrity as an isochron and therefore I do not recommend Tephra Peaks H, G, and F be pursued as an ideal isochron.

Although it does not display as much stratigraphic spread of tephra shards Tephra Peak D would require more in-depth analysis to be considered a suitable isochron in the future. Both Tephra Peaks D and H displayed the lowest shard concentrations out of all the statistically identified tephra peaks and were therefore not considered for further high-resolution analysis on the basis of time and instrumental constraints. Although the samples surrounding Tephra Peak D contained no tephra, suggesting it has some potential to become a strong by assuming it is the result of little-to-no post-depositional reworking, but the lack of detailed 1-cm stratigraphy or geochemical data prevents further characterising less significant peaks any further.

6.3.2 Tephra horizons with possible chronostratigraphic potential

Possible tephra horizons are defined here as those whose sedimentary and geochemical characteristics suggest they hold potential to serve as a robust chronostratigraphic marker, but are presently limited in some regard. Because Tephra Peak A and Tephra Peak C each contain two tephra populations, neither appear to be homogenous tephra layers.

Tephra Peak C

The shard concentration profile in high-resolution analysis of Tephra Peak C is confined to a narrow peak, since tephra is only found in the first two samples: between 2163 and 2162 cm and between 2162 and 2163 cm. The sample between 2163 and 2162 cm contains one shard that aligned inbetween trachy-dacite and rhyolite because it is composed of intermediate-to-high

silica (62.3 wt%) and intermediate-to-high total alkali (11.4 wt%) and a second shard that aligned with trachy-andesite because it was composed of intermediate silica (47.4 wt%) and intermediate total alkali (5.8 wt%) (Figure 5.3). The sample between 2163 and 2162 cm contained just one shard with a trachytic affinity. It was composed of 61.4 wt% silica and 9.6 wt% total alkali (Figure 5.3). From the three shards taken across the two samples, there are two populations: two higher silica trachytic shards and one lower silica trachy-basaltic shard. The one trachy-basaltic shard showed some affinity to Jan Mayen Volcanic Province primarily on the basis of its TAS ratio (Figure 6.3). However, the other geochemical oxides were not a match, and there are additionally no known records of a Jan Mayen eruption from the Last Interglacial with which to link or compare these results to. The remaining two shards from Population A were also not comparable to any of the major Last Interglacial tephra records from the North Atlantic, and they did not match Jan Mayen basaltic-trachytic composition either. However, the two shards from Population A seemed to show favourable affinity to a modern Icelandic eruption from Eyjafjallajökull and the wider volcanic zone, not the specific eruption itself, may be considered as a possible source for this population.

The major element data from Bispingen alone is not enough information to distinctly characterize this tephra layer, but the shard concentration profile places its stratigraphic position between 2163 and 2161 cm. The high resolution samples, taken between 2162 and 2163 cm actually occur just before Tephra Peak C, which is placed between 2161 cm and 2156 in the low resolution sequence. The low resolution sample from 2166 cm to 2161 cm, which includes the range selected for high-resolution analysis, still had about 3 shards/g tephra. There is a chance that because this occurs in the record before Tephra Peak C, it is the primary tephra air-fall deposit despite having a lower shard concentration. Nevertheless, the high-resolution tephra analysis displays two populations with somewhat unclear origins (Figures 4.3 and 5.3). It is not necessarily impossible for Tephra Peak C to serve as an isochronous ash layer because both the high and low resolution shard concentration profiles are display a narrow enough range to suggest there was not much post-depositional reworking and that it could have been a widespread ashfall event, but this would require finding a dated tephra layer with a geochemical profile that matches either of the populations.

Tephra Peak A

The shard concentration profile in high resolution analysis of Tephra Peak A was confined to a narrow peak, and tephra was only found in the last two 1-cm thick samples: between 2054 and 2053 cm (5 shards/g) and between 2053 and 2052 cm (3.5 shard/g). The sample between

2055 and 2054 cm contained one tephra shard that was classified in between basaltic trachyandesite and trachy-andesite because it contained low-to-intermediate silica (50 wt%) and low-to-intermediate (6.3 wt%) total alkali. The sample between 2054 and 2053 cm contained six tephra shards. Five of them were classified into Population A with high silica ranging between 65 wt% and 73 wt%, and very high total alkali between 14.2 wt% and 15.8 wt%. The final shard was classified as trachy-dacitic because of its high-to-intermediate silica (63.3 wt%) and intermediate total alkali (7.7 wt%) (Figure 5.3). The two tephra populations exhibit a wide range of geochemical signatures from trachy-basaltic to rhyolitic. The five-shard cluster of Population A exhibits the strongest case for becoming a stratigraphic tephra horizon in Bispingen because all of the other populations only contained a shard or two. The SiO₂ and FeO concentrations of Population A aligns well with other rhyolitic tephra layers, such as 5e-Eem/RHY-I but especially differs in Na₂O concentrations, which are about 4 wt% for 5e-Eem/RHY-I but over 10 wt% for Population A. The high sodium concentrations are unusually high for tephra. As hypothesized for Population B of Tephra Peak C, there are some trachytic Italian volcanoes that exhibit similarly high total Na₂O concentrations even exceeding 10 wt%, but these signatures are accompanied by lower SiO₂ concentrations below 60 wt% and much higher Al₂O₃ concentrations (e.g. Santacroce et al. 2008; Wulf et al. 2012; Table 2.8). Tephra Peak A Population B somewhat aligns with Population A of the 1855.5 cm record from MD99-229, but has much lower CaO (<1 wt%) and much higher FeO (>20 wt%) than the North Atlantic population. Since Population A exhibits high CaO (5 wt%) and low FeO (<1 wt%), the differences perhaps due to intrinsic chemical properties of the individual material rather than any post-depositional alteration which would affect all shards to a comparable degree.

There are no known Icelandic eruptions during MIS 5e that align with Population A of Tephra Peak A, but Population A offers a distinct cluster of geochemically similar tephra shards that could be identified easier than the other populations from the Bispingen sequence. The unique geochemical signature held by multiple shards in the same layer increases the likelihood that this population may be part of a wider heterogenous layer that has yet to be discovered during Pollen Zone VIb in other Northern European sites (Figure 6.14). Until then, it can be stated that there is a tephra layer of unknown origin in the BIS-2000 sequence between 2054 and 2053 cm that, with the exception of one shard, ranges in SiO₂ concentration from 65 wt% to 73 wt% and Na₂O concentration from 10.8 wt% to 14.2 wt%, raw. The one shard exception has a very low total percentage of 82 wt%, while the remaining five in the cluster range between 93 and 100 wt% total. Adjusting to 100 wt%, the normalised composition of this tephra layer ranges from 70.5 wt% to 72.1 wt% and Na₂O concentration from 11.7 wt% to 14.1 wt%. The tephra requires

further analysis to address the outlying shard and the origin of both tephra populations in Tephra Peak A. In summary, Tephra Peaks C and A may be considered candidates for further analysis before rejecting them as tephra isochrons.

6.3.3 Tephra horizons with strong chronostratigraphic potential

Strong tephra horizons are defined here as those whose sedimentary characteristics suggest they hold very strong potential to be found in other Northwest European sites and therefore serve as a robust chronostratigraphic marker. With goal to establish a regional Last Interglacial tephra network across Northwest Europe, Tephra Peaks B and especially E are the best example of tephra horizons that are most likely to be found in other sites besides Bispingen and may act ideal geochronological markers. Tephra Peak B is found at the start of Pollen Zone VIb, after the climate optimum during Pollen Zone V and offers a discrete stratigraphic position that can be narrowed down to between 2108 and 2110 cm.

Tephra Peak E is found in Pollen Zone V during the peak warmth of the interglacial (Lauterbach et al. 2024) and layer not only has the greatest shard concentration (>60 shards/g), but it also displays very little reworking in terms of tephra found in neighbouring samples. The sample directly above Tephra Peak B has no tephra and the sample directly below has a concentration of only 4.1 shards/g. The lower sedimentation rate in pollen Zone V (0.535 mm/year) may have provided favourable conditions for the large tephra peak B to accumulate without post-depositional mixing. This is supported by the high-resolution shard profile in which all shards were concentrated in just one 1-cm sample. The prepared stub for this sample did not contain any tephra and was consequently not analysed under the electron microprobe instrument, but based upon its very concise shard profile and distinct peak it may be assumed that this tephra layer was deposited by primary airfall. Tephra Peak E would be an ideal candidate to revisit to try and develop a geochemical profile from and then seek to link to other records.

6.3.4 Limitations and uncertainties

This study highlights distinct tephra peaks (A, B, C, E) based on shard concentration profiles and their distribution depths that offer some potential for establishing a Last Interglacial tephrochronology, along with four additional peaks that lack clear, distinct layers (D, F, G, H). However, there are limitations and uncertainties which are considered in this section.

Sampling methods

Overall, density separation techniques from Blockley et al. (2005) were successful not only in isolating individual tephra shards, but also in identifying tephra horizons during the counting stage. As many tephra shards in this study ranged between 20 and 80 μm , the analysed size fraction between 15 and 125 μm was suitable. It is recommended that future studies aiming to isolate and extract cryptotephra in Last Interglacial sediments should follow the same laboratory procedure. Following the same procedure used to identify the Bispingen tephra ensures robust comparisons between this study and new research.

Sampling intervals limit some of the results in this study with proper context. For example, there is a potential need for upcore sampling of Tephra Peak A because it was identified in the very first sample of this study. Generally, a 5 cm sampling interval was adequate for identifying tephra horizons as major peaks in shard concentrations. A 1 cm sampling interval was also adequate for identifying more precise stratigraphic positions. Except for Tephra Peak F, high-resolution analyses yielded continuous tephra profiles without gaps, suggesting that within a 5 cm sample, specific centimetre of tephra deposition could be identified. Nonetheless, due to the low total shard concentrations and the minimal difference between the highest and second-highest shard densities in a 1 cm high-resolution profile, it is challenging to confirm that the maximum concentration accurately represents the stratigraphic position. For a few tephra peaks, therefore, I am only able to assign ranges for stratigraphic positions that usually cover about 2-3 cm.

Timms et al. (2018) suggests that employing contiguous 1 cm-resolution sampling intervals over the entire sequence would help identify smaller tephra peaks that may otherwise be disregarded as reworked sediments in lower resolution sampling intervals. However, because this study is the first of its kind, it was more important to delegate time in the laboratory to identifying major tephra peaks in the Bispingen record before fine-tuning for smaller signals. In deciding which tephra layer to focus on, Tephra Peak E offers both the greatest shard concentration (>60 shards/g) with the lowest variability in surrounding samples, suggesting it was a primary airfall deposit. It was also the only tephra peak to concentrate all of its high-resolution shards into a singular 1-cm sample. The very low vertical variability of shards, and the ability to narrow down this peak to a single centimetre, already provides a precise and powerful stratigraphic position that can only be strengthened by its likely presence in other sequences.

Geochemical analysis

The EMPA instrument was calibrated using a variety of standards, including ML3B for basaltic glass and Lipari for rhyolitic glass. The shards with a higher silica concentration that leaned more towards a rhyolitic composition were calibrated an additional time. However, many previous studies chose to measure sodium first at a peak time of only 10 seconds and measure all other elements after at peak times between 20 to 30 seconds to reduce sodium migration (Hunt and Hill 1993). The instrument used in this study measured peak time at 20 seconds for all elements in this study, including sodium. Because sodium values in Population A of Tephra Peak C were very high, sodium migration did not appear to be a limit the results.

High resolution analysis required that identified tephra shards be removed and isolated from the slide to be mounted on epoxy resin stubs. In hindsight, it would have been more appropriate to mount one of the two high-resolution batches in glycerol instead of the permanent Canada Basalm mounting medium used on the primary low resolution slides. For the slides that were mounted with glycerol, the method of dissolving it by soaking the entire slide in a wide centrifuge tube with warm water was effective. The two stubs that did not contain any tephra were likely lost in the picking stage. There are alternative methods for picking, such as Lane et al. (2014) using a gas chromatography syringe. Either method, however, requires a high level of precision to pick single shards with as little extra material as possible. Ideally, it would not be necessary to pick ever single shard in high resolution sample as long as a minimum number was accounted for, but because the high resolution samples in the Bispingen sequence contained such few shards, it was especially important to try an pick every single one.

Transport

It is very important that the stratigraphic position of a tephra layer accurately reflects the timing of primary airfall, and therefore the timing of the eruption. The further away a tephra deposit lies from its eruptive source, the more difficult it becomes to correctly assign a stratigraphic position to the layer because volcanic horizons across hundreds, and especially thousands, of kilometres, are often non-visible (Lowe 2011). Understanding how, why, and where cryptotephra ends up in the sediment record of a particular site affects the magnitude to which it can later be used as an isochron. External factors of the wider environment and internal factors of tephra itself can also slow ash fall directly into a lake. Cryptotephra catchment follows the same taphonomic principles that guide other particles, like pollen, to settle in lakes (Pyne-O'Donnell 2010). Tephra largely depends on atmospheric winds, vegetation density, meteorological conditionals,

and snow cover at the time of eruption(Boygle 1999).

The tephra record from Bispingen highlights an overwhelming dominance of silicic volcanic ash based upon its clear or slightly pink colour morphology (Figure 5.4). Considering basaltic magma in Iceland often comes in contact with water to produce highly explosive phreatomagmatic eruptions, and several basaltic layers have already been identified in the North Atlantic and Norwegian Seas during the Last Interglacial (Table 2.5 i.e., Abbott, Austin, and Davies 2014), the lack of basaltic brown shards in Bispingen offers insight into tephra transport and reworking in the German lake.

The presence of basaltic tephra in the Bispingen record, or in this case lack thereof, depends on the possible sources of mafic tephra in Germany. When basaltic magma does not come in contact with water upon erupting, the explosions are relatively mild and produce lower tephra yields than their rhyolitic counterparts. In continental European eruptions, such as those from Massif Central in France or Eifel Volcanic Field in Germany, maar lakes are the only proximal bodies of water able to initiate the phreatomagmatic eruptions and not to the magnitude or frequency observed in Iceland, which sits as a small island in the North Atlantic. The density range of basaltic tephra, from 2.5 to 2.8 g/cm³, is greater than the density of silicic tephra, which is closer to 2.3 g/cm³ (Wolff-Boenisch, Gislason, and Oelkers 2004). As a consequence, basaltic tephra falls out of the atmosphere sooner and is less likely to reach ultra-distal sites, like Bispingen (Wastegard and Davies 2009). Even if basaltic shards reach Bispingen, they are more susceptible to hydration, as opposed to silicic shards which are more likely to retain their geochemical integrity over time (Cooper, Savov, and Swindles 2019). In certain conditions, the life span of a tephra shard, in regards to how long it can retain its chemical integrity in sediment, is nearly an order of magnitude greater for silicic shards than basaltic ones (Wolff-Boenisch, Gislason, and Oelkers 2004). Clear silicic shards are overwhelmingly favoured in the record, perhaps from chemical deterioration of brown basaltic shards, or even more likely from their lighter density and ability to be carried further from distal sources to Bispingen.

The same idea holds for larger shards over 100 µm for which Watson et al. (2016) suggest that cryptotephra above this size threshold are likely to fall out of the atmosphere before reaching ultra distal sites. This study also found that tephra preserved in lakes tended to have a larger median shard size than nearby peat deposits that contained the same tephra layer. The variety of shard sizes, often leaning towards the larger sizes than in peats (Watson et al. 2016), may be due to in-wash and catchment geomorphology that allow lakes to receive tephra by transport mechanisms other than direct airfall. Shard size data from small lakes captures a fuller picture of maximum shard size compared to equivalent peat data, and the size of a tephra shard does not

seem to have an impact on vertical migration within a record, like density does (Watson et al. 2016). Shard sizes tends to decrease with distance from the source, but this not always the case, as with the some Hekla-4 deposits recording greater median shard sizes in ultra-distal sites than proximal ones (Watson et al. 2016). While there are unique cases that deviate from expected transport trends in regards to size and density, it must be noted that distal sites are often limited by smaller sample sizes for comparing between sites.

While the low-resolution analysis only resulted in the identification of a few brown coloured shards in total, there was a more even distribution between clear and brown tephra shards in the high-resolution analysis. Although total counts in 1-cm samples were generally low (<5 shards), the majority of the 1 cm samples still contained about one or two brown shards that were otherwise entirely absent in their low-resolution counterparts. High-resolution analysis of well-preserved lake sediments, such as Bispingen, often captures focused tephra deposits that may only consist of a few shards (Watson et al. 2016). The slightly higher presence of brown shards in 1 cm high-resolution analysis may be related to how sediment settles in lakes. Lake sediments have a greater ability to capture single tephra shards that may be washed in from a wide catchment area, compared to peatland sites that tend to only record layers of primary airfall (Watson et al. 2016). In high latitude peatland sites especially, fallout onto prolonged snow cover is exposed to more wind and rain that distributes tephra layers unevenly during melting season (Figure 6.13; Watson et al. 2016; Bergman et al. 2004). For this reason, lake sediments may be more favourable for capturing the very low concentrations of tephra shards in high latitude sites.

From a comprehensive viewpoint, basaltic shards are not present in the Bispingen record, with the exception of two 5 cm-thick samples a few shards found throughout 1 cm-thick samples. There are several possible factors that may explain the lack of basaltic shards in the stratigraphy, including the lower ash yield of non phreatomagmatic eruptions and heavier density that decreases the maximum distance of transport. Regardless of shard colour morphology, whether clear or brown, the Bispingen sequence was able to capture tephra layers, albeit whose peaks are of relatively low concentration. For example, the series of minor tephra deposits centred around 2250 cm depth was not focused upon for its low shard concentrations (<5 shards/g), but its presence in the record nonetheless highlights that even low ash signals can be detected in the Bispingen palaeolake record.

Lastly, climate events, like the North Atlantic Oscillation that coincide with an eruption can influence the direction of tephra dispersal (Lacasse 2001; Martin-Garcia 2019) . During the NAO positive phase, a strong pressure gradient from the Azores to Iceland drives warm, moist air from the Azores northeastward. Conversely, in its negative phase, a weaker pressure gradient

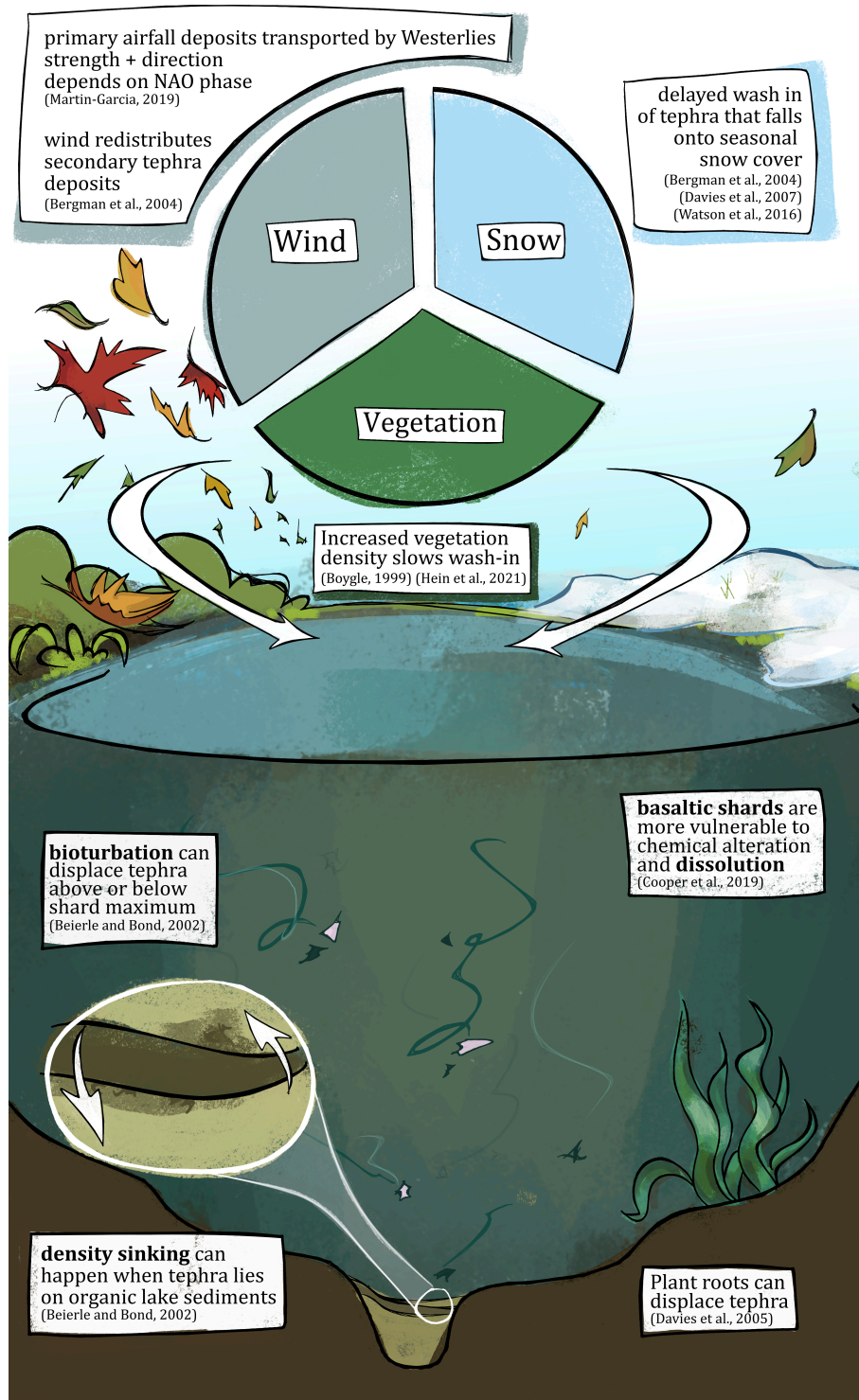


Figure 6.13: Illustration depicting the ways external factors can affect the stratigraphic position of a tephra layer. The top half shows how climate and vegetation conditions affect tephra transport into a lacustrine environment, and the bottom half shows how conditions within a lake can affect tephra shards even after they settle in the sediment.

allows air from Iceland to move southward towards Northern Europe (Martin-Garcia 2019). Western European eruptions originating from Azores, Massif Central, or Eiffel are more likely to travel northeast towards the Lower Saxony region during positive NAO phases than negative ones. On the other hand, Icelandic eruptions are more likely to be carried towards Lower Saxony in negative NAO phases than positive ones. Because the North Atlantic Oscillation occurs at an inter-annual to decadal scale, the exact timing of its cycles during the Last Interglacial cannot be determined, but it is nonetheless a confounding factor in how certain volcanic sources may be over or under-represented in the Bispingen record depending on the regional climatic phase at the time of eruption (Lacasse 2001; Martin-Garcia 2019). Geochemical analysis of a wider range of Last Interglacial tephra from around Europe will help unravel some of these questions around transport direction.

6.4 Future Work

The expansive network of Last Interglacial pollen assemblages are connected to each other over a regional scale by aligning alike pollen zones (PAZs). While some of these zones, of course, differ from one another, there are generally accepted zonations that allow comparisons between sites across the Netherlands, Germany, and even Poland (McGuire, Waajen, and Barlow 2024). When incorporating tephra layers into the Bispingen sequence, there is considerable scope to translate the position of the tephra layer to other Eemian sequences using their common pollen zones. The power of tephrostratigraphy is especially enhanced when the same tephra layer can be found in multiple sedimentary sequences. The tephra layers, therefore, can link pollen sequences independent of the pollen assemblage zones, thus refining the latter, current pollen zoning method. Bispingen Palaeolake, used in the very the first study of Last Interglacial pollen zone duration in Northwest Europe (Müller 1974), was an obvious choice for the very first likewise study using tephra. However, there is now potential to find the tephra layers in the other notable Last Interglacial sites in Northwest Europe and develop a tephra network similar to the established pollen one. This section discusses sites that may offer potential for finding tephra layers because of their robust and well-preserved Last Interglacial sediment sequences similar to that of Bispingen Palaeolake sequence.

The next concrete goal in establishing a Last Interglacial tephra network is to find one of the Bispingen tephra layers in another European Last Interglacial site. Moving forward, we must consider which layers are likely to be regionally widespread and which sites are likely to preserve a particular widespread tephra layer. More than just the presence of tephra itself, we must also

consider how connecting a new tephra layer to Bispingen will enhance our understanding of regional climate and its responses.

While lacustrine sequences, like Bispingen, are favourable for finding low concentration tephra layers where single shards may be washed in from the wider area, ombiotrophic peat sequences often show more discrete and obvious tephra layers because the lack of frequent stream influx concentrates primary fallout and reduces post depositions reworking (Watson et al. 2016). Revisiting lacustrine archives will ideally highlight small tephra signatures, but shifting towards ombiotrophic peat archives, in contrast, will ideally highlight the presence of primary tephra layers, such as Tephra Peak E. Less defined peaks, such as Tephra Peak F, may be present more discretely in peat sequences that have been yet to be analysed from a tephrostratigraphic perspective. As Tephra Peak F lies in Pollen Zone IV, originally thought to be 4000 years long (Müller 1974) but revised to be over 7000 years long (Lauterbach et al. 2024), finding this marker in another sequence will help link pollen zones between sites over a period of long duration and with otherwise poor chronostratigraphic constrains. Of course, the extended length of Pollen Zone IV by over 3000 years will have profound impacts on our understanding of the possible diachroneity in the onset of Last Interglacial warming between north and south Europe (McGuire, Waajen, and Barlow 2024). To truly confirm that the Last Interglacial lasted about 15,000 years in both halves of Europe, we would need to link a Bispingen tephra layer to one of many known Icelandic layers found in the well-studied North Atlantic sequences (e.g Sejrur et al. 1989; Sjøholm, Sejrur, and Furnes 1991; Fronval et al. 1998; Wastegård and Rasmussen 2001; Brendryen, Hafliðason, and Sejrur 2010; Abbott et al. 2011; Abbott et al. 2013; Abbott, Austin, and Davies 2014; Davies et al. 2014). Because both Tephra Peaks A and B were found towards the end of the Last Interglacial in Bispingen, it is important to revisit sites that offer complete and continuous sequences across all of the pollen zones.

6.4.1 The Netherlands

There are many well-studied Dutch pollen sequences that could be further re-investigated for potential tephra layers. Many Eemian pollen sequences in the Netherlands are preserved in ice-pushed ridge valleys, nearly 50 m below present sea level. Amersfoort and Amsterdam, two sites in this region, are notable places to further Last Interglacial climatological research in Northern Europe (Figure 6.14; Cleveringa et al. 2000; Zagwijn 1983). The Amersfoort sequence is located in a sheltered embayment just inland of the North Sea which is otherwise unaffected by the sea except in periods of extreme sea level highstands, such as the Last Interglacial (Long et

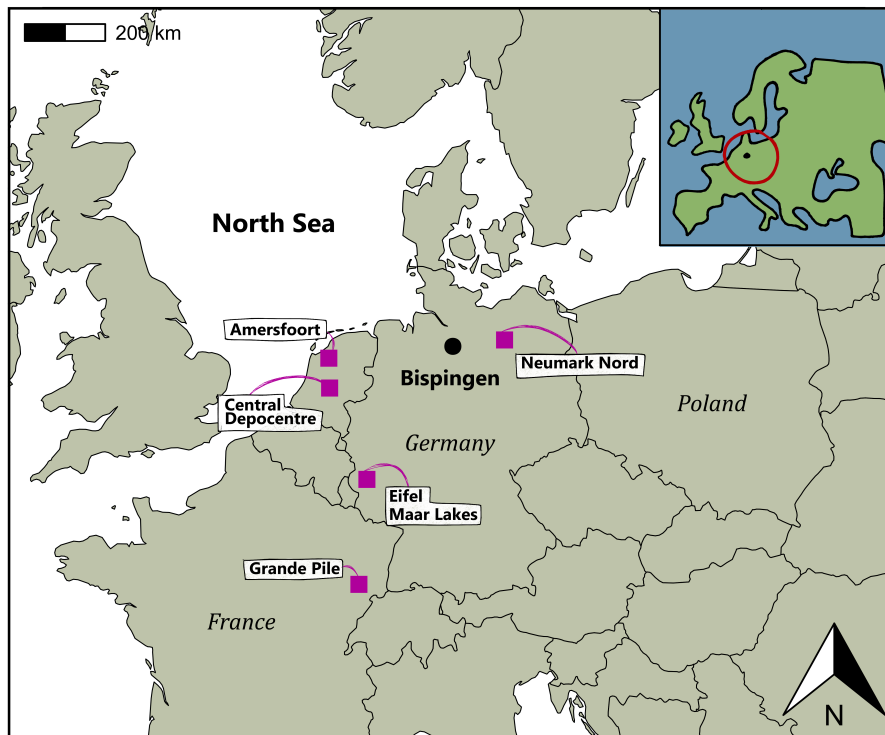


Figure 6.14: Map of Northwest European sites with continuous Eemian Pollen records discussed in this section.

al. 2015; Zagwijn 1961; Zagwijn 1983). The Amersfoort sequence contains a 15 m thick section of sediment that is associated with the Last Interglacial through drawing comparisons between established pollen successions. The continuous Amersfoort sequence contains all Eemian pollen zones from E2 through E6 with the exception of the very basal layer E1 (Zagwijn 1961; Cleveringa et al. 2000). There are a few breaks in the sequence either from erosion or from little to no sediment being deposited. One erosion break in E4a happened when the environment rapidly shifted from lacustrine to brackish marking the onset of marine transgression. In E5 the breaks in sediment were far more continuous, likely caused by eroding of glacial sands at the bounds of ice pushed ridges during marine transgression. Part way through E5 the record records an abrupt shift from transgressing marine sands to clay when the environment rapidly shifted back to freshwater conditions by E6, also recorded by Zagwijn 1983. E5, the specific PAZ named given by Zagwijn 1961, correlates to PAZ V at Bispingen (Table 2.2). If Tephra Peak B, in PAZ V, is also found here, this would be a vital location from which to correlate changes in sea level with regional environmental change.

Another site found in the ice carved valleys of the Netherlands offers a high potential for finding tephra and enhancing a wide range of geochemical and biostratigraphical proxies. The ice pushed ridges from the Saalian Glacial Period separate the Netherlands into several valleys or depocentres (Figure 6.14). Because the Southern Depocentre experienced more erosion, pre-

serving only the early basal layers of the Last Interglacial, the less-eroded Central Depocentre provides a greater hope for finding tephra layers (Peeters et al. 2016). Several cores taken in transects across the Central Depocentre by Peeters et al. 2016 reveal the Last Interglacial sediments average about 5-10 km in thickness. The Last Interglacial sediments have been analysed from both a biostratigraphical approach using pollen assemblages linked to the common Dutch Pollen Assemblage Zones (Zagwijn 1961; Zagwijn 1983), and from a geochemical approach using OSL dating of minerals. While OSL dating of feldspar minerals in sediments older than 100 ka can provide an absolute duration for the Last Interglacial, it often underestimates ages in ways tephra usually does not because tephra does not rely on exposure. For example, Peeters et al. 2016 underestimated the Last Interglacial age to be between 122 to 104 ka, much later than that suggested by other records (ref), and attributed the few thousand year difference to regional uplift that slowed North Sea transgression compared to eustatic sea-level rise and the sea-level highstand.

The Central Depocentre cores analysed for pollen, including B15F1501, B15G0212 13/14, B20E0063, would be strong choices for tephra analysis because their already established connection to the major pollen zones in the Netherlands can be easily translated to the major pollen zones in Germany from the Bispingen Sequence (Peeters et al. 2016; Müller 1974; Lauterbach et al. 2024). These records are both continuous and near complete through the Last Interglacial, offering a high likelihood that the large tephra peak found in this study during German Pollen Zone Vb may be found in the centre of these sequences where the equivalent E5a was also found (Table 2.2). As the study of deposits found in Saalian carved basins of the Central depocentre already have some age estimate of the Last Interglacial from luminescence dating, although underestimated, there is definitely potential to refine it using tephrostratigraphy.

6.4.2 Germany

German Site Neumark Nord 2 (51.19'28"N; 11.53'56"E; Figure 6.14) preserves a 6-8m thick Last Interglacial sediment record, lying in between later Weischelian gravels and earlier Saalian diamicton (Sier et al. 2011). This record also underwent a similar multiproxy analysis to the Dutch glacial basin deposits (Peeters et al. 2016). Here, the Last Interglacial sediments were analysed from both a biostratigraphical approach, using pollen assemblages linked to the common assemblage zones by Menke and Tynni (1984) and from a geochemical approach using palaeomagnetic age estimates. While palaeomagnetic age estimates refine the duration of the Last Interglacial in a way the floating pollen assemblages cannot, the age currently relies on the age of Sapropel 5,

which although is generally accepted at 124 ka, may still be revised in the future, thus re-affecting the palaeomagnetic age of this record (Corselli et al. 2002; Sier et al. 2011). The uncertainty in this palaeomagnetic estimate makes it quite difficult to compare the age of this record to the age of a marine record like Shackleton et al. (2002) did with Last Interglacial sediments near the Iberian Peninsula. In fact, while core MS952042 used in the study by Shackleton et al. (2002) aligned well with the global deep sea benthic $\delta^{18}\text{O}$ record, the ages at Neumark Nord lag 5000 years behind (Sier et al. 2011). Whether this supports an ongoing theory that European climate during the Last Interglacial in the north lagged a few thousand years behind the south, or whether the lag is due to age uncertainty in palaeomagnetic methods and Sapropel 5, cannot be precisely determined. Therefore, tephrostratigraphy as an absolute chronostratigraphic marker tool may be able to link Neumark Nord to the varved Bispingen record and constrain its palaeomagnetic age estimate independent of Sapropel 5.

The west Eifel Maar lakes (Figure 6.14) also offer opportunity to compare tephra preserved in other annually laminated lacustrine records in Germany. As the name of this record suggests, this sequence was taken from 30 dry Maar Lakes in the west Eifel volcanic field (Sirocko et al. 2005). The larger Eifel Laminated Sediment Archive (ELSA) project spans from the Pleistocene through the Holocene, but provides additional focus on the Late Eemian Aridity Pulse (LEAP) during the Last Interglacial (Sirocko et al. 2005). Anoxic bottom water in the maar lake prevented biologic reworking, so the varve facies present in the ELSA record during the Last Interglacial between 104 and 132 ka BP were studied in 30 μm thin sections (Sirocko et al. 2005). The pollen record from two cores, although aligning closer with the record from Ribains, France, rather than the German Bispingen record, are stratigraphically consistent and show identical pollen succession (Sirocko et al. 2005). There is also further potential to find tephra shards in the Last Interglacial thin sections that have already been produced from the ELSA project. Tephra may be easily visible in the thin sections if there was an eruption in West Eifel, given its close proximity to the volcanic source.

6.4.3 France

La Grande Pile (47°44'N, 6°30'14"E; Figure 6.14) is a strong candidate for further tephra research during the Last Interglacial because it is one of only a few sites in Northwest Europe that extends through the last major climate cycle. The well-documented chronological record offers an impressive timelines 140 ka from the Last Interglacial to the present Interglacial period (Woillard 1973). The site is located in the Southern Vosges Mountains of northeastern France.

It lies specifically in the Saint Germain basin, on an inter-fluvial plateau about 325 m above sea level (Ponel 1995).

The existing studies (e.g. Woillard 1973; Woillard 1975; Woillard 1976; Woillard 1978; Woillard 1979; Beaulieu and Reille 1992, Seret et al. 1992; Guiot et al. 1992; Guiot et al. 1993; Ponel 1995) have already established detailed isotope and pollen records, which greatly enhance the site's chronological framework. The multi-proxy records are well established within the wider Eemian pollen framework, providing a seamless stratotype between potential tephra found here and tephra already found at Bispingen. Furthermore, the extensive multi proxy research within the continuous record only strengthens the likelihood that Last Interglacial tephra will be also be well-preserved. In fact, tephra has already been identified in upper sections of La Grande Pile sequence (Juvigné and Mörner 1984). The sediment in which this tephra was found was radiocarbon dated between 53 to 62 ka, about half the age of Last Interglacial sediments (Woillard and Mook 1982). La Grande Pile's strategic location makes it an ideal site for capturing tephra from Massif Central, but because it lies towards the south of the Northwest Europe it may not capture very small and distal signals from Iceland. Because La Grande is primarily a peat environment, its strength lies in preserving primary tephra fallout rather than small tephra signals commonly found in palaeolakes with wide catchment areas, such as Bispingen.

Despite the fact that the Grand Pile record continuously extends to present day, the lack of annually laminated layers offered by Bispingen and select other glacial lakes in Europe (e.g. Lake Monticchio in Southern Italy, Wulf et al. (2012)) prevents it from being absolutely dated, as it stands. Therefore, establishing a common tephra stratotype between Bispingen and Grande Pile would be especially important for providing a chronological link across Northwestern Europe. Kukla et al. (1997) previously attempted to link the Grand Pile pollen sequence (core) from MIs 5e and 5d to the offshore Portugal record (MD95-2042) from Shackleton et al. (2002). Tephra may help draw chronostratigraphic constraints between these two records, furthering comparisons between terrestrial responses and marine responses during the Last Interglacial. Fully securing an absolute tie between Northern European terrestrial pollen records and a dated marine one may require a more developed tephra framework in the future. Regardless, Grande Pile lies further inland than many other Northern European sites (e.g. Amersfoort), so it offers a unique perspective on climate responses. A chronostratigraphic marker in the Grande Pile record would improve understanding of regional vegetation changes, thus facilitating temperature and precipitation reconstructions (Woillard 1978).

La Grande Pile's well-documented and continuous sedimentary record, combined with its strategic location and existing multi-proxy data, makes it an exceptional site for further tephra

research during the Last Interglacial. Grande Pile, in its extensive sedimentary history, lacks the distinct layering characteristics found in Bispingen. Establishing a chronostratigraphic marker between these two sites would, therefore, combine the detailed temporal resolution of Bispingen with the wide proxy analysis of Grande Pile.

6.5 Summary

Tephra Peak F is an inconclusive layer that suggests very high levels of reworking. Tephra Peaks C and A offer geochemical populations that can be linked to future tephra studies, even though they cannot be definitively linked to any known tephra layers at this point in time. Tephra Peak E and B offer discrete tephra maxima and suggest the likelihood of widespread ashfall events that could be found in other well-studied Northern European pollen sequences. These tephra maxima may be present even more discretely in peat archives, like Grande Pile, which often do not collect secondary tephra in-wash from the wider catchment area. Chronologically linking Bispingen tephra to Grand Pile would constrain continental system responses, while linking Bispingen tephra to Amersfoort would constrain more coastal and sea-level related responses.

CHAPTER 7

CONCLUSIONS

Since this is the first study of its kind, the initial milestone or aim of this study was to see whether it was possible for tephra to be observed in Last Interglacial pollen sequences in Northern Europe. Last Interglacial tephra layers have previously been identified in Southern European lake and cave records (Tzedakis et al. 2018) and in North Atlantic marine sequences (see Chapter 2). Tephra from Bispingen Palaeolake in Northern Germany is added to the list of known cryptotephra archives during the Last Interglacial. Not only was cryptotephra identified in the Bispingen sequence, The discovery of several distinct peaks in shard concentration are enough to prove that it is possible to build a tephra framework from the Eemian pollen sediment sequences.

Once tephra was discovered in the Bispingen sequence, the shards picked from high resolution samples underwent electron microprobe analysis to measure the concentrations of their major elements. Appropriate procedures were taken to ensure the reliability of this data. Geochemical data produced at least one distinct tephra population that could serve as tie point in future tephra studies in Northwest Europe. Tephra Peaks A and C each contained a main population with rhyolitic-to-dacitic compositions and one shard with a trachy-basaltic composition. The primary Population A of Tephra Peak A displayed unusually high sodium concentrations, and could not be linked to a known MIS 5e eruption. From the major element compositions, there were no direct matches to MIS 5e tephra from the North Atlantic to the tephra from this study, but Eyjafjallajökull may be the sourced of Tephra Peak C Population A of the basis of its similar geochemistry to a modern eruption. The TAS compositions Tephra Peak C Population B are closely related to that from a MIS 5d Jan Mayen eruption, which would suggest it may originate from a presently unknown eruption from this volcanic province, although its other major-element compositions do not exactly align. While the possible sources of tephra in the Bispingen record are not perfect matches, the record nonetheless shows promise in the development of a tephrochronological framework. Future studies should gather a greater number of individual shards for geochemical analysis to identify more robust tephra populations.

Even without geochemical classification, Tephra Peak B displays a distinct maximum in the shard concentration profile, making it likely to be identifiable in other sequences. Revisiting Northwest European sites to try and link these tephra peaks will help establish a regional

chronostratigraphic marker. The power of a chronostratigraphic marker in constraining the rates of interglacial warming responses depends on the location of the next investigated site. Linking a tephra layer from Bispingen to a coastal site, like Amersfoort in the Netherlands, will provide understanding of sea level changes. Linking a tephra layer from Bispingen to an inland site, like Grande Pile in France, will provide understanding of continental vegetation and climate changes. There is also nuance in the type of environment a sequence is retrieved from and that peat records, like Grande Pile (Woillard 1973, may preserve a particular tephra layer more concise, but less detailed, than Bispingen. As Bispingen is the first tephra record of this kind so far, it is not currently possible to link it to any existing archives, but this only strengthens the need for more studies in this region of continental Europe. Revisiting previously studied Last Interglacial sites in Northern Europe using a tephrostratigraphic approach can help distinguish geochemical nuances to determine the volcanic origins of the five Bispingen tephra peaks, contributing to a more precise geochronological framework. Correlating the Bispingen tephra horizons with other regional sedimentary archives in the future will ultimately build a network of isochronous layers. These time-linked tephra layers have the potential to anchor Eemian pollen zones and constrain the timing of Last Interglacial warming in Northern Europe.

7.1 Key Findings

1. Using density separation techniques, cryptotephra shards were identified in the poorly varved sections of the composite BIS-2000 sequence between 2050 cm to 2399 cm, covering upper PAZ IVb to lower PAZ VIb
2. Low resolution analysis of 5 cm-thick samples revealed five primary tephra peaks, which were identified on the presence of distinct maxima in shard concentration profile. The five key horizons demonstrate potential to establish a regional isochron in Bispingen sedimentary sequence.
3. Continuous high-resolution analysis of 1 cm-thick samples were sufficient for assessing the stratigraphic position of the five tephra horizons, discerning whether they were likely deposited as primary airfall deposits or the result of multiple reworking events.
4. Major element oxide data suggests the presence of a primary rhyolitic population with high sodium oxide concentrations that current prevent it from being linked to any known eruptions. Two other populations display some geochemical affinity to Icelandic and Jan Mayen eruptions, but cannot be definitively linked.
5. There are several well-studied sites in Northwestern Europe that offer great potential to

preserve one or more of the tephra horizons identified in this study. It is recommended that these sediment archives be reinvestigated for cryptotephra to unlock the full potential of the Bispingen tephra as regional chronostratigraphic markers.

CHAPTER 8

APPENDIX

Table 8.1: Low-resolution tephra counts. The leftmost column are the laboratory names assigned to each sample. Top and Bottom refer to the 5 cm depth each sample covers. The depth is relative to the BIS-2000 composite sedimentary sequence. Dry (g) refers to the weight of each sample after drying. Clear and brown represent the individual raw shard counts, while the final three columns are shard concentrations per gram calculated by dividing raw shard counts by the dry weight. Coloured rows are those samples used in high-resolution analysis.

Sample	Top (cm)	Bottom (cm)	Dry (g)	clear	brown	clear/g	brown/g	total/g
LT103	2050	2055.0	0.514	7	4	13.61868	7.782101	21.40078
LT104	2055	2060.0	0.363	1	0	2.754821	0	2.754821
LT105	2060	2065.0	0.48	0	0	0	0	0
LT106	2065	2070.0	0.421	0	0	0	0	0
LT107	2070	2075.0	0.65	0	0	0	0	0
LT108	2075	2080.0	0.748	5	0	6.684492	0	6.684492
LT109	2080	2085.0	0.547	0	0	0	0	0
LT110	2085	2090.0	0.839	0	0	0	0	0
LT111	2090	2095.0	0.369	1	0	2.710027	0	2.710027
LT112	2095	2100.0	0.752	0	0	0	0	0
LT113	2100	2105.0	0.868	0	0	0	0	0
LT114	2105	2108.0	0.475	0	0	0	0	0
LT119	2108	2113.0	1.014	34	0	33.53057	0	33.53057
LT120	2113	2118.0	0.811	0	0	0	0	0
LT127	2116	2121.0	1.104	0	0	0	0	0
LT128	2121	2126.0	1.169	1	0	0.855432	0	0.855432
LT129	2126	2131.0	0.844	1	0	1.184834	0	1.184834
LT130	2131	2136.0	1.157	0	0	0	0	0
LT131	2136	2141.0	1.018	0	0	0	0	0
LT132	2141	2146.0	0.952	1	0	1.05042	0	1.05042
LT133	2146	2151.0	0.94	5	0	5.319149	0	5.319149

Continued on next page

Table 8.1 – continued from previous page

Sample	Top (cm)	Bottom (cm)	Dry (g)	clear	brown	clear/g	brown/g	total/g
LT134	2151	2156.0	0.704	0	0	0	0	0
LT135	2156	2161.0	0.366	4	0	10.92896	0	10.92896
LT136	2161	2166.0	0.389	1	0	2.570694	0	2.570694
LT137	2166	2169.0	0.423	0	0	0	0	0
LT138	2169	2174.0	0.463	0	0	0	0	0
LT139	2173	2178.0	0.409	2	0	4.889976	0	4.889976
LT140	2178	2183.0	0.518	0	0	0	0	0
LT141	2183	2188.0	0.381	3	0	7.874016	0	7.874016
LT142	2188	2193.0	0.433	0	0	0	0	0
LT143	2193	2198.0	0.394	0	0	0	0	0
LT144	2198	2203.0	0.559	0	0	0	0	0
LT115	2203	2208.0	0.928	1	0	1.077586	0	1.077586
LT116	2208	2213.0	0.524	0	0	0	0	0
LT117	2213	2217.0	0.438	27	0	61.64384	0	61.64384
LT118	2217	2221.0	0.989	4	0	4.044489	0	4.044489
LT121	2239	2244.0	0.612	1	0	1.633987	0	1.633987
LT122	2244	2249.0	0.556	0	0	0	0	0
LT123	2249	2254.0	0.878	3	0	3.416856	0	3.416856
LT124	2254	2259.0	0.748	0	1	0	1.336898	1.336898
LT125	2259	2264.0	0.783	0	0	0	0	0
LT126	2264	2269.0	0.55	1	0	1.818182	0	1.818182
LT145	2267	2272.0	0.48	0	0	0	0	0
LT146	2272	2277.0	0.476	0	0	0	0	0
LT147	2277	2282.0	0.431	0	0	0	0	0
LT148	2282	2287.0	0.417	0	0	0	0	0
LT149	2287	2292.0	0.465	0	0	0	0	0
LT150	2292	2297.0	0.355	0	0	0	0	0
LT151	2297	2302.0	0.483	12	0	24.84472	0	24.84472
LT152	2302	2307.0	0.346	4	0	11.56069	0	11.56069
LT153	2307	2312.0	0.507	2	0	3.944773	0	3.944773
LT154	2312	2317.0	0.468	2	0	4.273504	0	4.273504

Continued on next page

Table 8.1 – continued from previous page

Sample	Top (cm)	Bottom (cm)	Dry (g)	clear	brown	clear/g	brown/g	total/g
LT155	2317	2322.0	0.497	2	0	4.024145	0	4.024145
LT156	2322	2327.0	0.562	1	0	1.779359	0	1.779359
LT157	2327	2332.0	0.613	1	0	1.631321	0	1.631321
LT158	2332	2337.0	0.377	3	0	7.95756	0	7.95756
LT159	2337	2341.0	0.551	0	0	0	0	0
LT160	2341	2345.0	0.593	0	0	0	0	0
LT161	2346	2349.0	0.329	0	0	0	0	0
LT162	2349	2354.0	0.585	0	0	0	0	0
LT163	2354	2359.0	0.459	0	0	0	0	0
LT164	2359	2364.0	0.518	0	0	0	0	0
LT165	2364	2369.0	0.334	0	0	0	0	0
LT166	2369	2374.0	0.274	0	0	0	0	0
LT167	2374	2379.0	0.527	0	0	0	0	0
LT168	2379	2384.0	0.291	1	0	3.436426	0	3.436426
LT169	2384	2389.0	0.373	0	0	0	0	0
LT170	2389	2394.0	0.415	0	0	0	0	0
LT171	2394	2399.0	0.345	0	0	0	0	0
LT172	2399	2404.0	0.348	0	0	0	0	0

Table 8.2: Table of tephra counts from high resolution samples. The samples are grouped in chronological order with the topmost Tephra Peak A samples at the top of the table and the deepest Tephra Peak E samples at the bottom of the table. The leftmost column are the laboratory names assigned to each sample. Top and Bottom refer to the 1 cm depth that each sample covers. The depth is relative to the BIS-2000 composite sedimentary sequence. Dry (g) refers to the weight of each sample after drying. Clear and brown represent the individual raw shard counts, while the final three columns are shard concentrations per gram calculated by dividing raw shard counts by the dry weight.

Sample	Top (cm)	Bottom (cm)	Dry (g)	clear	brown	clear/g	brown/g	total/g
LT192	2050	2051	0.547	0	0	0	0	0
LT193	2051	2052	0.632	0	0	0	0	0
LT194	2052	2053	0.729	0	0	0	0	0
LT195	2053	2054	0.568	1	1	1.760563	1.760563	3.521127
LT196	2054	2055	0.391	0	2	0	5.11509	5.11509
LT197	2108	2109	0.374	2	1	5.347594	2.673797	8.02139
LT198	2109	2110	0.28	2	1	7.142857	3.571429	10.71429
LT199	2110	2111	0.482	1	0	2.074689	0	2.074689
LT200	2111	2112	0.698	0	0	0	0	0
LT201	2112	2113	0.418	0	0	0	0	0
LT183	2161	2162	0.304	3	1	9.868421	3.289474	13.15789
LT184	2162	2163	0.254	1	4	3.937008	15.74803	19.68504
LT185	2163	2164	0.417	0	0	0	0	0
LT186	2164	2165	0.344	0	0	0	0	0
LT187	2165	2166	0.423	0	0	0	0	0
LT188	2213	2214	0.375	0	0	0	0	0
LT189	2214	2215	0.364	2	2	5.494505	5.494505	10.98901
LT190	2215	2216	0.435	0	0	0	0	0
LT191	2216	2217	1.141	0	0	0	0	0
LT173	2297	2298	0.55					7.27
LT174	2298	2299	0.655	0	0	0	0	0
LT175	2299	2300	0.438	1	0	2.283105	0	2.283105
LT176	2300	2301	0.428	0	0	0	0	0
LT177	2301	2302	0.529					7.56
LT178	2302	2303	0.464	7	0	15.08621	0	15.08621
LT179	2303	2304	0.564	0	0	0	0	0
LT180	2304	2305	0.387					7.75
LT181	2305	2306	0.415	2	1	4.819277	2.409639	7.228916
LT182	2306	2307	0.482	0	0	0	0	0

REFERENCES

- 1983 (n.d.). “The Elsterian glaciation in the Netherlands.” In: *1983* () (cit. on p. 7).
- Abbott, P.M. Austin W.E.N. Davies S.M. (2014). “Re-evaluation and extension of the Marine Isotope Stage 5 tephrostratigraphy of the Faroe Island region: the cryptotephra record.” In: *Palaeogeography, Palaeoclimatology, Palaeoecology* 409, pp. 153–168 (cit. on pp. 15–17, 19, 21, 22, 49, 74–79, 88, 100, 104).
- Abbott, P.M. Davies S.M. (2012). “Volcanism and the Greenland ice-cores: the tephra record”. In: *Earth-Science Reviews* 115, pp. 173–191 (cit. on p. 17).
- Abbott, P.M. et al. (2011). “Identification of cryptotephra horizons in a North East Atlantic marine record spanning marine isotope stages 4 and 5a (60,000-82,000 a b2k).” In: *Quaternary International* 246, pp. 177–189 (cit. on pp. 2, 19, 21, 49, 74, 104).
- (2013). “Cryptotephrochronology of a North East Atlantic marine sequence over termination II, the Eemian and the last interglacial-glacial transition.” In: *Journal of Quaternary Science* 28, pp. 501–514 (cit. on pp. 19, 21, 49, 74, 89, 104).
- Albert, P.G. et al. (2024). “Cryptotephra preserved in Lake Suigetsu (SG14 core) reveals the eruption timing and distribution of ash fall from Japanese volcanoes during the Late-glacial to early Holocene”. In: *Quaternary Science Reviews* 324, p. 108376 (cit. on p. 18).
- Aubry, T.J. Cerminara M. Jellinek A.M. (2019). “Impacts of climate change on volcanic stratospheric injections: comparison of 1-D and 3-D plume model projections”. In: *Geophysical Research Letters* 46, pp. 10609–10618 (cit. on p. 15).
- Aubry, T.J. et al. (2016). “Impact of global warming on the rise of volcanic plumes and implications for future volcanic aerosol forcing”. In: *Journal of Geophysical Research: Atmospheres* 121, pp. 13, 326–13, 351 (cit. on p. 15).
- Aubry, T.J. et al. (2022). “Impact of climate change on volcanic processes: current understanding and future challenges”. In: *Bulletin of Volcanology* 84, p. 58 (cit. on pp. 15, 19).
- Baeteman, C. Gans W. de (1993). “The western Coastal Plain of Belgium”. In: *Quaternary Shorelines in Belgium and The Netherlands. Excursion Guide of the 1993 Field meeting of the INQUA Subcommission of Shorelines of Northwestern Europe*. The Hague: Geological Survey of The Netherlands, pp. 1–24, 43–55 (cit. on p. 30).
- Bas, M. J. Le et al. (1992). “A chemical classification of volcanic rocks based on the total alkali-silica diagram”. In: *Journal of Petrology* 33.4, pp. 745–750 (cit. on pp. 17, 48, 49, 59, 62).

- Beaulieu, J.-L. de Reille M. (1992). “The last climatic cycle at La Grande Pile (Vosges, France) a new pollen profile”. In: *Quaternary Science Reviews* 11.4, pp. 431–438 (cit. on p. 108).
- Beets, D.J. Beets C.J. Cleveringa P. (2006). “Age and climate of the late Saalian and early Eemian in the type-area, Amsterdam basin, The Netherlands.” In: *Quaternary Science Reviews* 25, pp. 876–885 (cit. on p. 7).
- Behre, K.-E. (2004). “Coastal development, sea-level change and settlement history during the later Holocene in the Clay District of Lower Saxony (Niedersachsen), northern Germany”. In: *Netherlands Journal of Geosciences* 83, pp. 283–296 (cit. on p. 30).
- Behre, K.-E. Dörjes J. Irion G. (1985). “A dated Holocene sediment core from the bottom of the southern North Sea”. In: *Eiszeitalter Gegenwart* 35, pp. 9–13 (cit. on p. 30).
- Behre, K.-E. Hölzer A. Lemdahl G. (2005). “Botanical macro-remains and insects from the Eemian and Weichselian site of Oerel (northwest Germany) and their evidence for the history of climate”. In: *Vegetation History and Archaeobotany* 14.1, pp. 31–53 (cit. on p. 28).
- Behre, K.-E. Menke B. (1969). “Pollenanalytische Untersuchungen an einem Bohrkern der südlichen Doggerbank”. In: *Beiträge zur Meereskunde* 24.25, pp. 122–129 (cit. on p. 30).
- Behre, K.-E. Plicht J. van der (1992). “Towards an absolute chronology for the last glacial period in Europe: radiocarbon dates from Oerel, northern Germany”. In: *Vegetation History and Archaeobotany* 1.2, pp. 111–117 (cit. on p. 28).
- Beierle, B. Bond J. (2002). “Density-induced settling of tephra through organic lake sediments”. In: *Journal of Paleolimnology* 28, pp. 433–440 (cit. on pp. 16, 70).
- Benda, L. Brandes H. (1974). “Die Kieselgur-Lagerstätten Niedersachsens: I. Verbreitung, Alter und Genese”. In: *Geologisches Jahrbuch* A21, pp. 3–85 (cit. on p. 31).
- Berger, A. Loutre M.F. Mélice J.L. (2006). “Equatorial Insolation: From Precession Harmonics to Eccentricity Frequencies”. In: *Climate of the Past* 2, pp. 131–136 (cit. on p. 6).
- Bergman, J. et al. (2004). “Holocene tephra horizons at Klocka Bog, west-central Sweden: aspects of reproducibility in subarctic peat deposits”. In: *J. Quaternary Sci.* 19, pp. 241–249 (cit. on p. 101).
- Bilt, W.G.M. van der Lane C.S. Bakke J. (2017). “Ultra-distal Kamchatkan ash on Arctic Svalbard: Towards hemispheric cryptotephra correlation”. In: *Quaternary Science Reviews* 164, pp. 230–235 (cit. on pp. 2, 15).
- Blockley, S. P. E. et al. (2005). “A new and less destructive laboratory procedure for the physical separation of distal glass tephra shards from sediments”. In: *Quaternary Science Reviews* 24.16-17, pp. 1952–1960 (cit. on pp. iv, 39, 69, 98).

- Bluszcz, P. et al. (2008). “Global radiation and onset of stratification as forcing factors of seasonal carbonate and organic matter flux dynamics in a hypertrophic hardwater lake (Sacrower See, northeastern Germany)”. In: *Aquatic Geochemistry* 14, pp. 73–98 (cit. on p. 33).
- Bogaard, P. van den Schmincke H.-U. (1990). “Die Entwicklungsgeschichte des Mittelrheingebietes und die Eruptionsgeschichte des Oostfälisch-Vulkanfeldes”. In: *DEUQUA Führer* 1. Ed. by Schirmer, W., pp. 166–190 (cit. on pp. 23, 24).
- Boygale, J. (1999). “Variability of tephra in lake and catchment sediments, Svínavatn, Iceland”. In: *Global and Planetary Change* 21, pp. 129–149 (cit. on pp. 71, 100).
- Brauer, A. et al. (1999). “High resolution sediment and vegetation responses to Younger Dryas climate change in varved lake sediments from Meerfelder Maar, Germany.” In: *Quaternary Science Reviews* 18, pp. 321–329 (cit. on p. 19).
- Brauer, A. et al. (2000). “AMS radiocarbon and varve chronology from the annually laminated sediment record of Lake Meerfelder Maar, Germany.” In: *Radiocarbon* 42, pp. 355–368 (cit. on pp. 18, 19).
- Brendryen, J. Haflidason H. Sejrup H.P. (2010). “Norwegian Sea tephrostratigraphy of marine isotope stages 4 and 5: prospects and problems for tephrochronology in the North Atlantic region.” In: *Quaternary Science Reviews* 29, pp. 847–864 (cit. on pp. 19, 21, 22, 49, 74, 75, 79–85, 88, 89, 104).
- Brousse, R. et al. (1990). *La Tour d’Auvergne (740)*. 1:50 000 map and memoir. Orleans, France: Bureau de Recherches Géologiques et Minières (BRGM) (cit. on p. 24).
- Brunskill, G. J. (1969). “Fayetteville Green Lake, New York. II. Precipitation and sedimentation of calcite in a meromictic lake with laminated sediments”. In: *Limnology and Oceanography* 14, pp. 830–847 (cit. on pp. 33, 73).
- Cameron, D. et al. (1993). “Geology of the North Sea Basin”. In: *Coastlines of the Southern North Sea* Volume Number, Page Numbers (cit. on pp. 29, 30).
- Cartelle, V. et al. (2021). “Sedimentary architecture and landforms of the late Saalian (MIS 6) ice sheet margin offshore of the Netherlands”. In: *Earth Surface Dynamics* 9.6, pp. 1399–1421 (cit. on p. 27).
- Cleveringa, P. et al. (2000). “The Eemian stratotype locality at Amersfoort in the central Netherlands: a re-evaluation of old and new data”. In: *Netherlands Journal of Geosciences* 79, pp. 197–216 (cit. on pp. 104, 105).
- Cohen, K.M. Gibbard P.L. (2019). “Global chronostratigraphical correlation table for the last 2.7 million years, version 2019 QI-500”. In: *Quaternary International* 500, pp. 20–31 (cit. on p. 5).

- Cohen, K.M. et al. (2022). “Last Interglacial Sea Level Data Points from Northwest Europe.” In: *Earth System Science Data* 14, pp. 2895–2937 (cit. on pp. 11, 29).
- Cooper, C.L. Savov I.P. Swindles G.T. (2019). “Standard chemical-based tephra extraction methods significantly alter the geochemistry of volcanic glass shards”. In: *J. Quaternary Sci* 34, pp. 697–707 (cit. on pp. 39, 100).
- Corselli, C. et al. (2002). “Changes in Planktonic Assemblages during Sapropel S5 Deposition: Evidence from Urania Basin Area, Eastern Mediterranean”. In: *Paleoceanography* 17.3, 10-1 to 10–12 (cit. on p. 107).
- Davies, S.M. (2015). “Cryptotephra: the revolution in correlation and precision dating.” In: *Journal of Quaternary Science* 30, pp. 114–130 (cit. on pp. 2, 14, 42, 43, 45, 69, 72, 94).
- Davies, S.M. et al. (2005). “Detection of Lateglacial distal tephra layers in the Netherlands”. In: *Boreas* 34, pp. 123–135 (cit. on p. 71).
- Davies, S.M. et al. (2014). “A North Atlantic tephra framework for 130–60 ka b2k: new tephra discoveries, marine based-correlations and future challenges.” In: *Quaternary Science Reviews* (cit. on pp. 19, 21, 49, 53, 74, 78, 104).
- DeConto, R.M. et al. (2021). “The Paris Climate Agreement and future sea-level rise from Antarctica.” In: *Nature* 593, pp. 83–89 (cit. on p. 1).
- Dugmore, A.J. (1989). “Icelandic volcanic ash in Scotland.” In: *Scottish Geographical Magazine* 105, pp. 168–172 (cit. on p. 18).
- Dutton, A. Lambeck K. (2012). “Ice Volume and Sea Level During the Last Interglacial”. In: *Science* 337, p. 216 (cit. on p. 28).
- Dutton, A. et al. (2015). “Sea-level rise due to polar ice-sheet mass loss during past warm periods.” In: *Science* 349, p. 6244 (cit. on pp. 1, 6).
- Field, M.H. Huntley B. Muller H. (1994). “Eemian climate fluctuations observed in a European pollen record.” In: *Nature* 371, pp. 779–783 (cit. on pp. 9, 12).
- Folch, A. (2012). “A review of tephra transport and dispersal models: Evolution, current status, and future perspectives”. In: *Journal of Volcanology and Geothermal Research* 235-236, pp. 96–115 (cit. on p. 14).
- Förster, M.W. et al. (2010). “Late Pleistocene Eifel eruptions: insights from clinopyroxene and glass geochemistry of tephra layers from Eifel Laminated Sediment Archive sediment cores”. In: *Journal of Quaternary Science* 35, pp. 186–198 (cit. on p. 23).
- Fox-Kemper, B. et al. (2021). “The Physical Science Basis. Contribution of Working Group I to the Sixth Assessment Report of the Intergovernmental Panel on Climate Change.” In: *Cambridge University Press*, pp. 1211–1362 (cit. on p. 1).

- Frechen, J. Lippolt H.J. (1965). “Kalium-Argon-Daten zum Alter des Laacher Vulkanismus, der Rheinterrassen und der Eiszeiten”. In: *Quaternary Science Journal* 16, pp. 5–30 (cit. on p. 23).
- Fronval, T. et al. (1998). “Variability in surface and deep water conditions in the Nordic Seas during the Last Interglacial Period.” In: *Quaternary Science Reviews* 17, pp. 963–985 (cit. on pp. 2, 19, 21, 22, 49, 74, 104).
- Gewelt, M. Juvigné E. (1986). “Les « téphra de Remouchamps », un nouveau marqueur stratigraphique dans le Pléistocène supérieur daté par 230Th/234U.” In: *Annales de la Société géologique de Belgique* 109, pp. 489–497 (cit. on p. 23).
- Giaccio, B. Nomade S. Wulf S. Et al. (2012). “The late MIS 5 Mediterranean tephra markers: a reappraisal from peninsular Italy terrestrial records”. In: *Quaternary Science Reviews* 56, pp. 31–45 (cit. on pp. 24, 25).
- Gill, R. Fitton J.G. (2010). *Igneous Rocks and Processes: A Practical Guide*. 2nd. Wiley (cit. on pp. 15, 16, 22).
- Gjerløw, E. Hafliðason H. Pedersen R.B. (2016). “Holocene explosive volcanism of the Jan Mayen (island) volcanic province, North-Atlantic”. In: *Journal of Volcanology and Geothermal Research* 321, pp. 31–43 (cit. on pp. 89, 91).
- Goe'r de Herve, A. de et al. (1993). “Le puy de Gravenoire et ses coulées, dans l'agglomération de Clermont-Ferrand (Massif central français): un mode 'le inhabituel d'avalanche de débris, déclenché par une éruption strombolienne en climat périglacière”. In: *Bulletin de la Société géologique de France* 164, pp. 783–793 (cit. on p. 24).
- Govin, A. al. et (2015). “Sequence of events from the onset to the demise of the Last Interglacial: Evaluating strengths and limitations of chronologies used in climatic archives.” In: *Quaternary Science Reviews* 129, pp. 1–36 (cit. on pp. 6, 9, 10).
- Guarino, M.-V. et al. (2020). “Sea-ice-free Arctic during the Last Interglacial supports fast future loss”. In: *Nature Climate Change* 10, pp. 928–932 (cit. on p. 1).
- Gue'rin, G. (1983). “La thermoluminescence des plagioclases, method de datation du volcanisme. Applications au domaine volcanique français: Chaîne des Puys, Mont Dore et Cezaillier, Bas Vivarais”. The'se de Doctorat d'Etat e's Sciences, Physique. Université Pierre et Marie Curie (cit. on p. 24).
- Guiot, J. et al. (1992). “Calibration of the climatic signal in a new pollen sequence from La Grande Pile”. In: *Journal of Quaternary Science* 6.3-4, pp. 259–264 (cit. on p. 108).

- Guiot, J. et al. (1993). “The climate in Western Europe during the last Glacial/Interglacial cycle derived from pollen and insect remains”. In: *Palaeogeography, Palaeoclimatology, Palaeoecology* 103.1-2, pp. 73–93 (cit. on p. 108).
- Haarnagel, W. (1979). *Die Grabung Feddersen Wierde. Methode, Hausbau, Siedlungs- und Wirtschaftsformen sowie Sozialstruktur*. Date of Issue From: 1979. Monograph, p. 190 (cit. on p. 30).
- Hageman, B. P. (1969). “Development of the western part of the Netherlands during the Holocene”. In: *Geologie en Mijnbouw* 48, pp. 373–388 (cit. on p. 30).
- Hall, M. Hayward C. (2014). “Preparation of micro-and crypto-tephras for quantitative microbeam analysis”. In: *Geological Society, London, Special Publications* 398, SP398–5 (cit. on p. 39).
- Hall, V. A. Pilcher J. R. (2002). “Late-Quaternary Icelandic tephras in Ireland and Great Britain: detection, characterization and usefulness”. In: *The Holocene* 12.2, pp. 223–230 (cit. on p. 39).
- Harting, P. (1874). “De bodem van het Eemdal.” In: *Verslagen en Verhandelingen Koninklijke Academie van Wetenschappen 2C* Reeks 8, pp. 282–290 (cit. on p. 7).
- Hays, J.D. Imbrie John Shackleton N.J. (1976). “Variations in the Earth’s Orbit: Pacemaker of the Ice Ages”. In: *Science* 194, pp. 1121–1132 (cit. on p. 6).
- Hayward, C. (2012). “High spatial resolution electron probe microanalysis of tephras and melt inclusions without beam-induced chemical modification”. In: *Holocene* 22, pp. 119–125 (cit. on p. 46).
- Heaton, T.J. (Nov. 2022). “Non-parametric calibration of multiple related radiocarbon determinations and their calendar age summarisation”. In: *Journal of the Royal Statistical Society Series C: Applied Statistics* 71.5, pp. 1918–1956 (cit. on p. 9).
- Hein, M. et al. (2021). “Eemian landscape response to climatic shifts and evidence for northerly Neanderthal occupation at a palaeolake margin in northern Germany”. In: *Earth Surface Processes and Landforms* 46, pp. 1–18 (cit. on pp. 27, 71).
- Helmens, K.F. (2014). “The Last Interglacial–Glacial cycle (MIS 5–2) re-examined based on long proxy records from central and northern Europe”. In: *Quaternary Science Reviews* 86, pp. 115–143 (cit. on p. 28).
- Hunt, J. B. (1997). “Quaternary tephrology and tephrochronology of the North Atlantic region”. Unpublished PhD. PhD thesis. University of Edinburgh (cit. on p. 46).
- Hunt, J. B. Hill P. G. (1993). “Tephra geochemistry: a discussion of some persistent analytical problems”. In: *Holocene* 3, pp. 271–278 (cit. on pp. 46–48, 99).

- (2001). “Tephrological implications of beam size—sample-size effects in electron microprobe analysis of glass shards”. In: *Journal of Quaternary Science: Published for the Quaternary Research Association* 16.2, pp. 105–117 (cit. on pp. 46, 47).
- Hunt, J. B. et al. (1998). “Interlaboratory comparison of electron probe microanalysis of glass geochemistry”. In: *Proceedings of the Ocean Drilling Program, Scientific Results* 152, pp. 85–91 (cit. on p. 47).
- Imbrie, J. et al. (1984). “The orbital theory of Pleistocene climate: support from a revised chronology of the marine $\delta^{18}\text{O}$ record”. In: *Milankovitch and Climate*. Ed. by Berger, A. et al. Norwell, MA: Riedel, pp. 269–305 (cit. on p. 6).
- IPCC (2019). “Sea level rise and implications for low-lying islands, coasts and communities”. In: *IPCC Special Report on the Ocean and Cryosphere in a Changing Climate*. Ed. by Pörtner, H.-O. et al. Cambridge: Cambridge University Press, pp. 321–445 (cit. on p. 7).
- (2021). *Climate Change 2021: The Physical Science Basis*. Geneva, Switzerland: Intergovernmental Panel on Climate Change (cit. on pp. 5, 6).
- Jakobsson, S.P. (1979). “Petrology of Recent basalts of the Eastern Volcanic Zone, Iceland”. In: *Acta Naturalia Islandica* 26, p. 103 (cit. on pp. 74, 85).
- Jessen, A. Milthers V. (1928). *Stratigraphical and paleontological studies of interglacial freshwater deposits in Jutland and Northwest Germany*. Vol. 48. Danmarks Geologiske Undersøgelse (cit. on pp. 1, 12).
- Jones, G. et al. (2018). “The Lateglacial to early Holocene tephrochronological record from Lake Hämelsee, Germany: a key site within the European tephra framework”. In: *Boreas* 47, pp. 28–40 (cit. on pp. 18, 19).
- Juggins, Steve (2024). *rioja: Analysis of Quaternary Science Data*. R package version 1.0-7. URL: <https://cran.r-project.org/package=rioja> (cit. on p. 42).
- Juvigné, E. (1985). “Données nouvelles sur l’âge de la capture de la Warche à Bévercé.” In: *Bulletin de la Société géographique de Liège* 21, pp. 3–11 (cit. on p. 23).
- Juvigné, E. Mörner N.A. (1984). “A volcanic ash-fall at the Early-Mid Weichselian Würmian transition in the peat-bog of Grande Pile (Vosges, France)”. In: *Eiszeitalter und Gegenwart* 34, pp. 1–5 (cit. on p. 108).
- Kaspar, F. et al. (2005). “A model-data comparison of European temperatures in the Eemian interglacial.” In: *Geophysical Research Letters* 32, p. L11703 (cit. on p. 1).
- Kearney, R.J. et al. (2024). “At an important tephrostratigraphic crossroads: cryptotephra in Late Glacial to Early Holocene lake sediments from the Carpathian Mountains, Romania”. In: *Quaternary Science Reviews* 330, p. 108558 (cit. on p. 22).

- Keller, J. et al. (1978). “Explosive volcanic activity in the Mediterranean over the past 200,000 yr as recorded in deep-sea sediments”. In: *Geological Society of America Bulletin* 89, pp. 591–604 (cit. on p. 25).
- Kelts, K. Hsü K. J. (1978). “Freshwater carbonate sedimentation”. In: *Lakes: Chemistry, Geology, Physics*. Ed. by Lerman, A. New York: Springer, pp. 295–324 (cit. on pp. 33, 73).
- Kershaw, A.P. Nix H.A. (1988). “Quantitative Palaeoclimatic Estimates from Pollen Data Using Bioclimatic Profiles of Extant Taxa”. In: *Journal of Biogeography* 15, pp. 589–602 (cit. on p. 8).
- Kinder, M. et al. (2020). “Late-Holocene ultra-distal cryptotephra discoveries in varved sediments of Lake Żabińskie, NE Poland.” In: *Journal of Volcanology and Geothermal Research* 402, p. 106988 (cit. on pp. 14, 22).
- Knudsen, K.L. (1993). “Late Elsterian–Holsteinian foraminiferal stratigraphy in boreholes in the Lower Elbe area, NW Germany”. In: *Geologisches Jahrbuch A* 138, pp. 97–119 (cit. on p. 29).
- Kopp, R.E. et al. (2009). “Probabilistic assessment of sea level during the last interglacial stage.” In: *Nature* 462, pp. 863–867 (cit. on pp. 1, 11).
- Kristjánisdóttir, G.B. et al. (2007). “Geochemistry of Holocene cryptotephra from the North Iceland Shelf (MD99-2269): intercalibration with radiocarbon and paleomagnetic chronostratigraphies”. In: *The Holocene* 17, pp. 155–176 (cit. on p. 42).
- Kühl, N. et al. (Nov. 2002). “Probability Density Functions as Botanical-Climatological Transfer Functions for Climate Reconstruction”. In: *Quaternary Research* 58.3, pp. 381–392 (cit. on p. 10).
- Kühl, N. et al. (2007). “Eemian and Early Weichselian temperature and precipitation variability in northern Germany.” In: *Quaternary Science Reviews* 26, pp. 3311–3317 (cit. on p. 12).
- Kukla, G.J. et al. (1997). “How long and how stable was the Last Interglacial?” In: *Quaternary Science Reviews* 16, pp. 605–612 (cit. on pp. 10, 108).
- Kvamme, T. et al. (1989). “Geochemistry of Pleistocene ash zones in cores from the North Atlantic”. In: *Norsk Geologisk Tidsskrift* 69, pp. 251–272 (cit. on pp. 42, 69).
- Laban, C. (2000). “The Pleistocene glaciations in the Dutch sector of the North Sea: A synthesis of sedimentary and seismic data”. Supervisors: P. D. Jungerius and J. J. M. van der Meer. PhD thesis. Faculty of Social and Behavioural Sciences (FMG), p. 194 (cit. on p. 29).
- Lacasse, C. (2001). “Influence of climate variability on the atmospheric transport of Icelandic tephra in the subpolar North Atlantic”. In: *Global Planetary Change* 29, pp. 31–55 (cit. on pp. 15, 89, 101, 103).

- Lambeck, K. et al. (2006). “Constraints on the Late Saalian to early Middle Weichselian ice sheet of Eurasia from field data and rebound modelling.” In: *Boreas* 35, pp. 539–575 (cit. on p. 11).
- Lane, C. Woodward J. (2022). “Tephrochronology”. In: *Encyclopedia of Geoarchaeology*. Ed. by Gilbert, A. S. et al. Encyclopedia of Earth Sciences Series. Springer, Cham (cit. on pp. 17, 18).
- Lane, C.S. et al. (2014). “Cryptotephra as a dating and correlation tool in archaeology”. In: *Journal of Archaeological Science* 42, pp. 42–50 (cit. on pp. 18, 99).
- Lane, C.S. et al. (2015). “The Late Quaternary tephrostratigraphy of annually laminated sediments from Meerfelder Maar, Germany.” In: *Quaternary Science Reviews* 122, pp. 192–206 (cit. on pp. 2, 18, 19).
- Lane, C.S. et al. (2011b). “Tephrochronology and absolute centennial scale synchronisation of European and Greenland records for the last glacial to interglacial transition: a case study of Soppensee and NGRIP.” In: *Quaternary International*, pp. 145–156 (cit. on pp. 18, 19).
- Lane, C.S. et al. (2011a). “The occurrence of distal Icelandic and Italian tephra in the Lateglacial of Lake Bled, Slovenia.” In: *Quaternary Science Reviews* 30, pp. 1013–1018 (cit. on p. 24).
- Laskar, J. et al. (2004). “A long term numerical solution for the insolation quantities of the Earth”. In: *Preprint submitted on 23 May 2004*. HAL Id: hal-00001603 (cit. on p. 1).
- Lauterbach, S. et al. (2024). “Re-investigation of the Bispingen palaeolake sediment succession (northern Germany) reveals that the Last Interglacial (Eemian) in northern-central Europe lasted at least 15,000 years.” In: *Boreas* (cit. on pp. iv, 2, 9–12, 28, 32–34, 36–39, 55, 65–68, 71–73, 97, 104, 106).
- Leeuwen, R.J. Van et al. (2000). “Stratigraphy and integrated facies analysis of the Saalian and Eemian sediments in the Amsterdam-Terminal borehole, the Netherlands.” In: *Netherlands Journal of Geosciences* 79, pp. 161–196 (cit. on p. 7).
- Leyk, H.J. Lippolt H.J. (1999). “ $^{40}\text{Ar}/^{39}\text{Ar}$ -Untersuchungen an spat quartaren Vulkaniten der Eifel- Neue Arbeitsansätze zur Datierung junger Lavastrome”. In: *Berichte der Deutschen Mineralogischen Gesellschaft Beih. z. European Journal of Mineralogy* 11.1, p. 145 (cit. on p. 23).
- Lisiecki, L.E. Raymo M.E. (2005). “A Pliocene-Pleistocene stack of 57 globally distributed benthic $\delta^{18}\text{O}$ records”. In: *Paleoceanography* 20, PA1003 (cit. on p. 6).
- Litt, T. (1990). *Pollenanalytische Untersuchungen zur Vegetations- und Klimaentwicklung während des Jungpleistozäns in den Becken von Gröbern und Grabschütz*. Vol. 5. Altenburger naturwissenschaftliche Forschungen, pp. 92–105 (cit. on p. 8).

- Litt, T. Junge F.W. Böttger T. (1996). “Climate during the Eemian in north-central Europe - a critical review of the palaeobotanical and stable isotope data from central Germany”. In: *Vegetation History and Archaeobotany* 5, pp. 247–256 (cit. on pp. 8, 9, 12, 33).
- Liu, X. Galloway W. E. (1997). “Quantitative Determination of Tertiary Sediment Supply to the North Sea Basin”. In: *AAPG Bulletin* 81.9, pp. 1482–1509 (cit. on p. 29).
- Long, A.J. et al. (2015). “Near-field sea-level variability in northwest Europe and ice sheet stability during the Last Interglacial.” In: *Quaternary Science Reviews* 126, pp. 26–40 (cit. on pp. 11, 104).
- Long, D. et al. (1988). “The sedimentary record of climatic variation in the southern North Sea”. In: *Philosophical Transactions of the Royal Society B: Biological Sciences* 318.1191, 29 April 1988 (cit. on p. 29).
- Lowe, D.J. (2011). “Tephrochronology and its application: a review.” In: *Quaternary Geochronology* 6, pp. 107–153 (cit. on pp. 2, 14–18, 42, 45, 47, 48, 53, 74, 99).
- Lowe, D.J. et al. (2017). “Correlating tephtras and cryptotephtras using glass compositional analyses and numerical and statistical methods: Review and evaluation”. In: *Quaternary Science Reviews* 175, pp. 1–44 (cit. on pp. 48, 49, 57, 58, 61).
- Lowe, J.J. Turney C.S.M. (1997). “Vedde Ash layer discovered in a small lake basin on the Scottish mainland.” In: *Journal of the Geological Society* 154, pp. 605–612 (cit. on p. 18).
- Lüthi, D. et al. (2008). “High-resolution carbon dioxide concentration record 650,000–800,000 years before present.” In: *Nature* 453, pp. 379–382 (cit. on p. 1).
- Maier, D. B. et al. (2018). “Using a decadal diatom sediment trap record to unravel seasonal processes important for the formation of the sedimentary diatom signal”. In: *Journal of Paleolimnology* 60, pp. 133–152 (cit. on p. 33).
- Mamamkowa, K. (1989). “Late middle polish glaciation, Eemian and early Vistulian vegetation at Imbramowice near Wrocław and the pollen stratigraphy of this part of the Pleistocene in Poland.” In: *Acta Palaeobotanica* 29, pp. 11–176 (cit. on pp. 8, 33).
- Mangerud, J. (1989). “Correlation of the Eemian and the Weichselian with deep sea oxygen isotope stratigraphy”. In: *Quaternary International* 3/4, pp. 1–4 (cit. on p. 1).
- Martin-Garcia, G.M. (2019). “Oceanic Impact on European Climate Changes during the Quaternary”. In: *Geosciences* 9.3, p. 119 (cit. on pp. 15, 101, 103).
- McGuire, A.M. Waajen I.M. Barlow N.L.M. (2024). “Advancing chronologies for Last Interglacial sequences”. In: *Journal of Quaternary Science*, pp. 1–24 (cit. on pp. 36, 103, 104).
- McManus, J.F. et al. (1994). “High-resolution climate records from the North Atlantic during the last interglacial.” In: *Nature* 371, pp. 326–329 (cit. on p. 10).

- Members, CAPE Last Interglacial Project (2006). “Last Interglacial Arctic warmth confirms polar amplification of climate change.” In: *Quaternary Science Reviews* 25, pp. 1383–1400 (cit. on p. 1).
- members, NEEM community (2013). “Eemian interglacial reconstructed from a Greenland folded ice core.” In: *Nature* 493, pp. 489–494 (cit. on p. 7).
- Menke, B. Tynni R. (1984). *Das Eeminterglazial und das Weichselfrühglazial von Rederstal-/Dittmarschen und ihre Bedeutung für die mitteleuropäische Jungpleistozängliederung*. Vol. A 76. Geologisches Jahrbuch, pp. 3–120 (cit. on pp. 8, 9, 33, 106).
- Meschede, M. Warr L. N. (2019). *The Geology of Germany: A Process-Oriented Approach*. Springer (cit. on p. 27).
- Meyer, W. (1994). *Geologie der Eifel*. 3rd. Stuttgart: E. Schweizerbart’sche Verlagsbuchhandlung (Na’gele u. Obermiller) (cit. on p. 23).
- Milankovitch, M. (1941). *Kanon der Erdbestahlung und seine Anwendung auf das Eiszeitenproblem*. Belgrade: Royal Serbian Academy of Sciences (cit. on pp. 1, 5, 6).
- Mohn, H. (1878). “Askereggen den 29de-30te Marts 1875.” In: *Forhandlinger i Videnskabs-selskabet i Christiania aar 1877* 10, pp. 1–12 (cit. on p. 18).
- Müller, H. (1974). “Pollenanalytische Untersuchungen und Jahresschichtenzählung an der eemzeitlichen Kieselgur von Bispingen/Luhe.” In: *Geologisches Jahrbuch* A21, pp. 149–169 (cit. on pp. 2, 8, 10–13, 26, 31, 33, 34, 36, 37, 65, 66, 73, 103, 104, 106).
- Murray, J. (2006). “Ecology and Applications of Benthic Foraminifera”. In: *Palaeogeography, Palaeoclimatology, Palaeoecology* 95, pp. 1–426 (cit. on p. 45).
- Navratil, Petr et al. (2013). “Geochemical characterization of the 2010 Eyjafjallajökull eruption”. In: *Journal of Volcanology and Geothermal Research* 256, pp. 1–15 (cit. on pp. 85–90).
- Olafsson, H. Rousta I. (2021). “Influence of atmospheric patterns and North Atlantic Oscillation (NAO) on vegetation dynamics in Iceland using Remote Sensing”. In: *European Journal of Remote Sensing* 54, pp. 351–363 (cit. on p. 15).
- Otto-Bliesner, B.L. et al. (2021). “Large-scale features of Last Interglacial climate: results from evaluating the lig127k simulations for the Coupled Model Intercomparison Project (CMIP6)–Paleoclimate Modeling Intercomparison Project (PMIP4)”. In: *Climate of the Past* 17, pp. 63–94 (cit. on pp. 1, 5, 7).
- Pastre, J-F. Debarde E. Chennaoui K. (1994). “Un tephra-repe’re du volcanisme phre’atomagmatique du Vivarais dans la se’quence Ple’istoce’ne supe’rieur de l’abri Moula (Soyons, Arde’che, France)”. In: *Comptes rendus l’Acade’mie des Sciences, Paris, se’rie II* 319, pp. 937–943 (cit. on p. 24).

- Paterne, M. Guichard F. Duplessy J.C. Et al. (2008). “A 90,000–200,000 yrs marine tephra record of Italian volcanic activity in the Central Mediterranean Sea”. In: *Journal of Volcanology and Geothermal Research* 177, pp. 187–196 (cit. on p. 25).
- Peeters, J. et al. (2016). “Sedimentary architecture and chronostratigraphy of a late Quaternary incised-valley fill: A case study of the late Middle and Late Pleistocene Rhine system in the Netherlands”. In: *Quaternary Science Reviews* 131, pp. 211–236 (cit. on p. 106).
- Pilleyre, T. et al. (1992). “Attempts at dating ancient volcanoes using the red TL of quartz”. In: *Quaternary Science Reviews* 11, pp. 13–17 (cit. on p. 24).
- Pirson, S. et al. (2006). “Belgian cave entrance and rock-shelter sequences as palaeoenvironmental data recorders: the example of Walou cave.” In: *Geologica Belgica* 9, pp. 275–286 (cit. on p. 23).
- Plunkett, G. Pilcher J.R. (2018). “Defining the potential source region of volcanic ash in north-west Europe during the Mid- to Late Holocene”. In: *Earth-Science Reviews* 179, pp. 20–37 (cit. on p. 89).
- Ponel, P. (1995). “Rissian, Eemian and Würmian Coleoptera assemblages from La Grande Pile (Vosges, France)”. In: *Palaeogeography, Palaeoclimatology, Palaeoecology* 114, pp. 1–41 (cit. on p. 108).
- Poucllet, A. Juvigné E. Pirson S. (2008). “The Rocourt Tephra, a widespread 90–74 ka stratigraphic marker in Belgium.” In: *Quaternary Research* 70, pp. 105–120 (cit. on p. 23).
- Preusser, F. Rufner D. Schreurs G. (Dec. 2011). “Direct dating of Quaternary phreatic maar eruptions by luminescence methods”. In: *Geology* 39.12, pp. 1135–1138 (cit. on p. 23).
- Pyne-O’Donnell, S. (2010). “The taphonomy of Last Glacial–Interglacial Transition (LGIT) distal volcanic ash in small Scottish lakes.” In: *Boreas* (cit. on pp. 71, 99).
- (2011). “The taphonomy of Last Glacial–Interglacial Transition (LGIT) distal volcanic ash in small Scottish lakes”. In: *Boreas* 40.1, pp. 131–145 (cit. on p. 17).
- Raynal, J-P. et al. (1984). “La maar de Saint-Hippolyte (Puy-de-Do^{me}, France). Datation par thermoluminescence, flores et faunes, fossiles, présence humaine, climatologie et dynamique du système paléolacustre”. In: *Revue des Sciences Naturelles d’Avergne* 50, pp. 97–114 (cit. on p. 24).
- Riede, F. et al. (2011). “A Laacher See-eruption supplement to TephraBase: Investigating distal tephra fallout dynamics.” In: *Quaternary International* 246, pp. 134–144 (cit. on p. 19).
- Rollinson, H. R. (2014). *Using geochemical data: evaluation, presentation, interpretation*. Routledge (cit. on p. 48).

- Salonen, J. S. et al. (2021). “Contrasting northern and southern European winter climate trends during the Last Interglacial”. In: *Geology* 49, pp. 1220–1224 (cit. on p. 28).
- Sánchez-Goñi, M.F. et al. (2002). “Synchronicity between marine and terrestrial responses to millennial scale climatic variability during the last glacial period in the Mediterranean region”. In: *Climate Dynamics* 19, pp. 95–105 (cit. on p. 9).
- Santacroce, R. et al. (2008). “Age and whole rock-glass compositions of proximal pyroclastics from the major explosive eruption of Somma-Vesuvius: a review as a tool for distal tephrstratigraphy”. In: *J. Volcanol. Geoth. Res.* 177, pp. 1–18 (cit. on pp. 24, 96).
- Sanzelle, S. et al. (2000). “Datation par thermoluminescence: étude d’une corrélation chronologique possible entre le maar de La Vestide-du-Pal et un niveau de téphra de La Baume-Moula-Guercy (Arde‘che, France)”. In: *Comptes rendus l’Académie des Sciences, Paris, se´rie II* 321, pp. 541–546 (cit. on p. 24).
- Schrum, C. (1997). “Thermohaline stratification and instabilities at tidal mixing fronts: results of an eddy resolving model for the German Bight”. In: *Continental Shelf Research* 17.6, pp. 689–716 (cit. on p. 27).
- Scussolini, P. et al. (2023). “Modeled storm surge changes in a warmer world: the Last Interglacial”. In: *Climate of the Past* 19, pp. 141–157 (cit. on p. 28).
- Seddon, A. W. R. et al. (2017). “Improved quantification of UV-B absorbing compounds in *Pinus sylvestris* L. pollen grains using an internal standard methodology”. In: *Review of Palaeobotany and Palynology* 247, pp. 97–104 (cit. on p. 45).
- Seiriene, V. et al. (2021). “Correlation of Eemian sections in Lithuania and Belarus based on palaeomagnetic, radioisotope and palaeobotanic data”. In: *Geological Quarterly* 65, p. 46 (cit. on p. 10).
- Sejrup, H.P. et al. (1989). “Quaternary tephrchronology on the Iceland Plateau, north of Iceland.” In: *Journal of Quaternary Science* 4, pp. 109–114 (cit. on pp. 19, 21, 49, 74, 89, 104).
- Selle, W. (1962). “Geologische und vegetationskundliche Untersuchungen an einigen wichtigen Vorkommen des letzten Interglazials in Nordwestdeutschland.” In: *Geologisches Jahrbuch* 79, pp. 295–352 (cit. on pp. 13, 36, 52, 65).
- Seret, G. et al. (1992). “Tentative palaeoclimatic reconstruction linking pollen and sedimentology in La Grande Pile (Vosges, France)”. In: *Quaternary Science Reviews* 11.4, pp. 425–430 (cit. on p. 108).
- Shackleton, N.J. (1987). “Oxygen Isotopes, Ice Volume and Sea-Level”. In: *Quaternary Science Reviews* 6.3-4, pp. 183–190 (cit. on p. 1).

- Shackleton, N.J. et al. (2002). “The Classic Marine Isotope Substage 5e.” In: *Quaternary Research* 58, pp. 14–16 (cit. on pp. 9, 10, 36, 107, 108).
- Shackleton, N.J. et al. (2003). “Marine Isotope Substage 5e and the Eemian Interglacial”. In: *Global and Planetary Change* 36, pp. 151–155 (cit. on pp. 1, 28, 91).
- Sier, M.J. et al. (2011). “Direct terrestrial-marine correlation demonstrates surprisingly late onset of the last interglacial in central Europe”. In: *Quaternary Research* 75.1, pp. 213–218 (cit. on pp. 106, 107).
- Sirocko, F. et al. (2005). “A late Eemian aridity pulse in central Europe during the last glacial inception”. In: *Nature* 436, pp. 833–836 (cit. on pp. 12, 23, 24, 28, 107).
- Sirocko, F. et al. (2016). “The ELSA-Vegetation-Stack: reconstruction of Landscape Evolution Zones (LEZ) from laminated Eifel maar sediments of the last 60,000 years”. In: *Global and Planetary Change* 142, pp. 108–135 (cit. on p. 23).
- Sjøholm, J. Sejrup H.P. Furnes H. (1991). “Quaternary volcanic ash zones on the Iceland Plateau, southern Norwegian Sea.” In: *Journal of Quaternary Science* 6, pp. 159–173 (cit. on pp. 2, 19, 21, 22, 49, 74, 104).
- Ster, H. et al. (2015). “Paleomagnetism and its applications in understanding geological processes”. In: *Earth, Planets and Space* 67, Article number: 70 (cit. on p. 10).
- Streif, H. (2004). “Sedimentary record of Pleistocene and Holocene marine inundations along the North Sea coast of Lower Saxony, Germany”. In: *Quaternary International* 112, pp. 3–28 (cit. on pp. 29–31).
- Thorarinsson, S. (1981b). “Greetings from Iceland. Ash-falls and volcanic aerosols in Scandinavia.” In: *Geografiska Annaler* 63A, pp. 109–118 (cit. on p. 18).
- Timms, R. G. et al. (2018). “Toward a tephrostratigraphic framework for the British Isles: A Last Glacial to Interglacial Transition (LGIT c. 16-8 ka) case study from Crudale Meadow, Orkney”. In: *Quaternary Geochronology* 46, pp. 28–44 (cit. on p. 98).
- Titos, M. et al. (2021). “Assessing potential impact of explosive volcanic eruptions from Jan Mayen Island (Norway) on aviation in the North Atlantic”. In: *Preprint* (cit. on pp. 88, 89).
- Turner, C. (2000). “The Eemian interglacial in the North European plain and adjacent areas.” In: *Geologie en Mijnbouw / Netherlands Journal of Geosciences* 79, pp. 2–3 (cit. on p. 7).
- Turner, C. West R.G. (1968). “The subdivision and zonation of interglacial periods.” In: *Eiszeitler und Gegenwart* 19, pp. 93–101 (cit. on pp. 8, 9).
- Turney, C.S.M. et al. (2006). “North European last glacial-interglacial transition (LGIT; 15-9 ka) tephrochronology: extended limits and new events”. In: *Journal of Quaternary Science* 21, pp. 335–345 (cit. on p. 71).

- Tzedakis, C. (2003). “Timing and duration of last interglacial conditions in Europe: a chronicle of a changing chronology.” In: *Quaternary Science Reviews* 22, pp. 763–768 (cit. on p. 9).
- Tzedakis, P.C. et al. (2018). “Enhanced climate instability in the North Atlantic and southern Europe during the Last Interglacial.” In: *Nature Communications* 9, pp. 1–14 (cit. on pp. 9, 36, 110).
- Väliranta, M. et al. (2009). “Early Weichselian interstadial (MIS 5c) summer temperatures were higher than today in northern Fennoscandia”. In: *Quaternary Science Reviews* 28.9-10, pp. 777–782 (cit. on p. 8).
- Vera, C. et al. (2013). “Understanding and Predicting Climate Variability and Change at Monsoon Regions”. In: *Climate Science for Serving Society*. Dordrecht: Springer, pp. 273–306 (cit. on p. 1).
- Vogel, H. et al. (2010). “A tephrostratigraphic record for the last glacial–interglacial cycle from Lake Ohrid, Albania and Macedonia.” In: *Journal of Quaternary Science* 25, pp. 320–338 (cit. on pp. 24, 25).
- Walsh, A.A. Blockley S.P.E. Milner A.M. (2021). “Complexities in European Holocene cryptotephra dispersal revealed in the annually laminated lake record of Diss Mere, East Anglia.” In: *Quaternary Geochronology* 66, p. 101213 (cit. on p. 24).
- Wastegård, S. Davies S.M. (2009). “An overview of distal tephrochronology in northern Europe during the last 1000 years”. In: *Journal of Quaternary Science* 24, pp. 500–512 (cit. on pp. 69, 100).
- Wastegård, S. Johansson H. Pacheco J.M. (2020). “New major element analyses of proximal tephros from the Azores and suggested correlations with cryptotephros in North-West Europe”. In: *Journal of Quaternary Science* 35, pp. 114–121 (cit. on p. 93).
- Wastegård, S. Rasmussen T.L. (2001). “New tephra horizons from Oxygen Isotope 5 in the North Atlantic: correlation potential for terrestrial, marine and ice-core archives.” In: *Quaternary Science Reviews* 20, pp. 1587–1589 (cit. on pp. 19, 21, 22, 49, 74, 78, 89, 104).
- Watson, E.J. et al. (2016). “The transport of Icelandic volcanic ash: Insights from northern European cryptotephra records”. In: *Journal of Geophysical Research: Solid Earth* 121, pp. 7177–7192 (cit. on pp. 15, 94, 100, 101, 104).
- Wheatcroft, R.A. et al. (1990). “A mechanistic view of the particulate biodiffusion coefficient: step lengths, rest periods and transport directions”. In: *Journal of Marine Research* 48, pp. 177–207 (cit. on p. 71).
- Winter, J. D. (2009). *Principles of Igneous and Metamorphic Petrology*. second. New York: Prentice-Hall, p. 702 (cit. on p. 48).

- Woda, C. Mangini A. Wagner G.A. (Dec. 2001). “ESR dating of xenolithic quartz in volcanic rocks”. In: *Quaternary Science Reviews* 20.5-9, pp. 993–998 (cit. on p. 23).
- Woillard, G. (1973). “Mise en évidence de l’Eemien sur le plateau de Haute-Saône”. In: *Comptes Rendus Académie des Sciences Paris* 276, pp. 939–942 (cit. on pp. 107, 108, 111).
- (1975). “Recherches palynologiques sur le Pleistocene dans l’Est de la Belgique et dans les Vosges Lorraines”. In: *Acta Geographica Lovaniensia* 14, pp. 1–168 (cit. on p. 108).
- (1976). “Comparison between the chronology from the beginning of the classical Eemian to the beginning of the classical Würm in Grande Pile peatbog, and other chronologies in the world”. In: *International Geological Correlation Programme (IGCP), Project 7311124. “Quaternary Glaciations in the Northern Hemisphere,” Report 4, Session in Stuttgart-Hohenheim, 5-13 September 1976, Prague 1977*, pp. 72–82 (cit. on p. 108).
- (1979). “Abrupt end of the last interglacial s.s. in north-east France”. In: *Nature* 281, pp. 558–565 (cit. on p. 108).
- Woillard, G.M. (1978). “Grande Pile peat bog: a continuous pollen record for the last 140,000 years.” In: *Quaternary Research* 9, pp. 1–21 (cit. on pp. 10, 108).
- Woillard, G.M. Mook W.G. (1982). “Carbon-14 dates at Grande Pile: correlation of land and sea chronologies”. In: *Science* 215, pp. 159–161 (cit. on p. 108).
- Wolff-Boenisch, D. Gislason S.R. Oelkers E.H. (2004). “The effect of fluoride on the dissolution rates of natural glasses at pH 4 and 25 degrees C”. In: *Geochimica et Cosmochimica Acta* 68.22, pp. 4571–4582 (cit. on p. 100).
- Wulf, S. et al. (2012). “The 100 - 133 ka tephra record of Lago Grande di Monticchio, southern Italy: implication for a revised chronology.” In: *Quaternary Science Reviews* (cit. on pp. 10, 24, 25, 39, 91–93, 96, 108).
- Zagwijn, W. H. (1979). “Early and Middle Pleistocene coastlines in the southern North Sea basin”. In: 2, pp. 31–42 (cit. on p. 29).
- (1961). “Vegetation, climate and radiocarbon datings in the late Pleistocene of the Netherlands: I. Eemian and early Weichselian.” In: *Mededelingen van de Geologische Stichting Nieuwe Serie* 14, pp. 15–45 (cit. on pp. 8, 13, 33, 36, 105, 106).
- (1983). “Sea-level changes in the Netherlands during the Eemian.” In: *Geologie en Mijnbouw* 62, pp. 437–450 (cit. on pp. 8, 12, 33, 104–106).
- (1985). “An outline of the Quaternary stratigraphy of the Netherlands”. In: *Geologie en Mijnbouw* 64, pp. 17–24 (cit. on p. 29).
- (1996). “An analysis of Eemian climate in Western and Central Europe.” In: *Quaternary Science Reviews* 15, pp. 451–469 (cit. on pp. 2, 8).

- Zillen, L.M. Wastegård S. Snowball I.F. (2002). “Calendar year ages of three mid-Holocene tephra layers identified in varved lake sediments in west central Sweden.” In: *Quaternary Science Reviews* 21, pp. 1583–1591 (cit. on p. 18).
- Zolitschka, B. et al. (2015). “Varves in lake sediments – a review”. In: *Quaternary Science Reviews* 117, pp. 1–41 (cit. on p. 36).
- Zöller, L. Blanchard H. (2009). “The partial heat–longest plateau technique: testing TL dating of Middle and Upper Quaternary volcanic eruptions in the Eifel Area, Germany.” In: *Quaternary Science Journal* 58, pp. 86–106 (cit. on p. 23).